POLITECNICO DI MILANO

Facoltà di Ingegneria Industriale

Corso di Laurea in
Ingegneria Spaziale

Student hybrid thruster testing and research

in collaboration with

German Aerospace Center (DLR), Institute of Space Propulsion
Lampoldshausen, Germany

Relatore: Prof. Luigi T. DE LUCA
Supervisore: Ing. Wolfgang KITSCHE

Tesi di Laurea di:

Giacomo COSTA   Matr.750986

Anno Accademico 2012 - 2013

Table of contents

List of figures

List of tables

Acronyms

DLR	Deutschen Zentrums für Luft- und Raumfahrt
RANS	Reynolds Averaged Navier-Stokes
LES	Large Eddy Simulation
LOX	Liquid oxygen
FLOX	Fluorin mixed with LOX
N_2O	Nitrus oxider or laughing gas
ISS	International space station
RP-1	Rocket Propellant-1 or Refined Petroleum-1
MHT	Micro hybrid thruster
SAO	Spalart-Allmaras Original
PDE	Partial differential equation
PET	Polyethylene Terephthalate
T006	Test number 6
T007	Test number 7
CFD	Computational Fluid Dynamics
IR	Infrared

Sommario

Nell'ambito dell'esplorazione spaziale, la propulsione ibrida è attualmente una tra le più promettenti tecniche per la generazione di spinta. Spesso in secondo piano a favore dei propellenti liquidi e solidi, più economici e di più semplice realizzazione gli ibridi coniugano insieme i pregi di entrambe le già diffuse metodologie di propulsione ponendosi nel mezzo in quanto a performance, problematiche di realizzazione e di utilizzo ed economicità.

Molti sono ad oggi gli studi che vengono condotti sui più svariati propellenti ibridi al fine di caratterizzarli e renderli il futuro dell'esplorazione spaziale. Ed è quanto viene fatto anche dall'*Agenzia Spaziale Tedesca* (Deutsches Zentrum für Luft-und Raumfahrt - DLR) che, nell'istituto di propulsione di Lampoldshausen in Germania, si dedica anche alla ricerca e allo sviluppo della propulsione ibrida.

Nell'ambito di questa ricerca si pone il presente lavoro di tesi che, svoltosi nel laboratorio M11 del DLR – Lampoldshausen ed in collaborazione con il Politecnico di Milano, ha lo scopo di studiare, comprende e caratterizzare il comportamento di un micro propulsore ibrido alimentato da ossido di diazoto N_2O e polietilene tereptalato PET.

In particolare la tesi qui discussa prevede una prima parte in cui l'intero sistema studiato viene valutato e analizzato numericamente secondo le ormai diffuse tecniche di *fluidodinamica computazionale* (CFD) utilizzando, per la risoluzione dei flussi turbolenti e il calcolo dell'equilibrio chimico dei reagenti, il software Tau code, sviluppato internamente al DLR, e NASA Cea. Da sottolineare la realizzazione della mesh e la logica utilizzata nella risoluzione numerica del problema.

All'analisi numerica segue poi quella sperimentale, condotta attraverso una campagna di test che si avvale anche di tecniche di visualizzazione avanzata, quali quella ad infrarossi e schlieren, con lo scopo finale di comparare i risultati ottenuti nei due casi e minimizzare le differenze.

Si pone l'attenzione sui gas esausti in uscita dall'ugello, sulla loro struttura e composizione con accenni anche riguardo alle proprietà termodinamiche del polietilene tereftalato.

Abstract

In the context of space exploration, hybrid propulsion is currently one of the most promising techniques for the thrust generation. Often in the background respect to the liquid and solid propellants, hybrids combine together the advantages of both the successful methods placing itself in the middle in terms of performance, utilization and construction problems and economy.

Several are presently the studies that are conducted on a wide range of hybrid propellants in order to characterized them for the future of the space exploration. And it is also what is done by the *German Aerospace Centre* (Deutsches Zentrum für Luft-und Raumfahrt - DLR) that, in the institute of propulsion in Lampoldshausen, Germany, is also dedicated to the research and development of hybrid propulsion.

As part of this research is the present work, which took place in the M11 laboratory of the DLR – Lampoldshausen in collaboration with Politecnico of Milan, in order to study, understand and characterize the behavior of the micro hybrid thruster powered by nitrous oxide N_2O and polyethylene terephthalate PET.

In particular, the work here discussed includes a first part in which the system is studied and evaluated numerically according to the widely used techniques of *computational fluid dynamics* (CFD) using for the resolution of the turbulent flows and the calculation of the equilibrium of the reactants, the internal DLR software Tau code and NASA Cea. Noteworthy the construction of the mesh and the logic used in the numerical solution of the problem.

At the numerical analysis then follows the experimental one, conducted through a series of tests which also makes use of advanced visualization techniques, such as infrared and schlieren, with the aim of comparing the results obtained in both cases and minimize the differences.

It focuses on the exhaust gases leaving the nozzle, their structure and composition with even hints about thermodynamic properties of polyethylene terephthalate.

1. Introduction to hybrid propulsion

The hybrid propulsion is based on the utilization of a liquid oxidizer and a solid fuel. By selecting one propellant as a liquid and the other as a solid, it is possible to take advantages from both the configuration, making the hybrid engine in an intermediate configuration between the complexity of the liquid propulsion and the extremely simplicity of the solid one. The resulting rocket motor evidences features of both the system, making available a large number of design options and operational characteristic. The main advantages of hybrid propulsion are presented further.

1.1. Historical notes

Interestingly enough from the beginning, the hybrid propulsion see its dawn in the late 30's [16] during which sporadic investigation were performed with the main objective to prove the feasibility of hybrid combustion in rocket motors. This was also the period of the main development of liquid and solid propulsion but the major know-how and asset toward these two propulsion configurations, lead to focus the efforts on them. However, a lots of studies were conducted on the problem of hybrid propulsion and now, it is possible to state that the past years of active research provides illustrations of hybrid rocket applied to a large variety of applications nowadays [16].

The first flight using hybrid propulsion goes back to 1933 in the Soviet Union but a broad series of tests and studies were conducted in Europe and USA [17].

In 1937, Noegerrath and Lutz performed some tests on 10 kN thrust engines for about 120 seconds in Germany using coal disks stacked and multi drilled in which flowed nitrous oxide gas (N_2O) [18]. Also Oberth tried to perform some hybrid characterization tests using LOX and graphite but the results of these first two experiences were unsatisfactory.

In the early of 40's an amateur group California Pacific Rocket Society had some success using LOX and a wide range of different fuel such as wood, wax, gum. The combination LOX- gum had the major success and allowed a rocket to reach 9 km high in 1951.

In the 1946 Bartel and Rannie from Jet Propulsion Laboratory, experimented an engine which had coal as solid fuel and the authors made the very first mathematical model of hybrid combustion.

Also Moore and Berman from General Electric in the 1956 tried to test the couple peroxide and polyethylene in a grain tube with bar. They observed a regular and efficient combustion process with a series of positive consequences:

- Remarkable longitudinal uniformity of combustion;

- No effects of the solid grain fractures on combustion;
- Gradual start of combustion;
- Stable combustion because the combustion surface behaved itself as a stabilizer;
- The process were easily controllable thanks to a valve;
- An high liquid/solid ratio were recommended (0/F=7) for simplify combustion;
- The resulting burning rate was low and not sensible to all the attempts to change it.

Altman, a very passionate researcher, stated which was the basic concept of the hybrid propulsion: "The combustion chamber pressure for an hybrid engine is proportional to the to the flow rate of oxidizer and not to the surface area exposed to the flame. There's no danger of explosion due to breakage fissures in the propellant charge as with solid propellant engines..." [17].

Author	fuel	Oxidizer
Noegerrath(1937) and Lutz (1938-1941)	Coal	N_2O
Smith (1938-1941)	Coal	O_2
Bartel and Rannie (1946)	Coal	Air
Dembrown and Pompa (1952)	J P	NH_4NO_3, NH_4ClO_4, $KClO_4$
Moore and Berman (1956)	P E	H_2O_2 (90%)
Ordhal (1959)	Metal based	Halogen compounds
Moutet and Barrère (1960)	Organic plastics	HNO_3

Table 1: Synthetic overview of the historical development of hybrid propulsion

1.2. Fundamentals of hybrid propulsion

The hybrid propulsion is based on the use of combustion reagents in different states of matter: solid and either in liquid or gaseous phase. That's why this kind of propulsion is called *hybrid*, differentiating from liquid or solid propulsion in which reagents are stored in the same state of aggregation. There are two

different types of configurations: direct or reverse. In the direct and classical configurations the fuel is solid and the oxidizer is liquid or gaseous, while in the reverse configuration a solid oxidizer is used with a liquid or gaseous fuel.
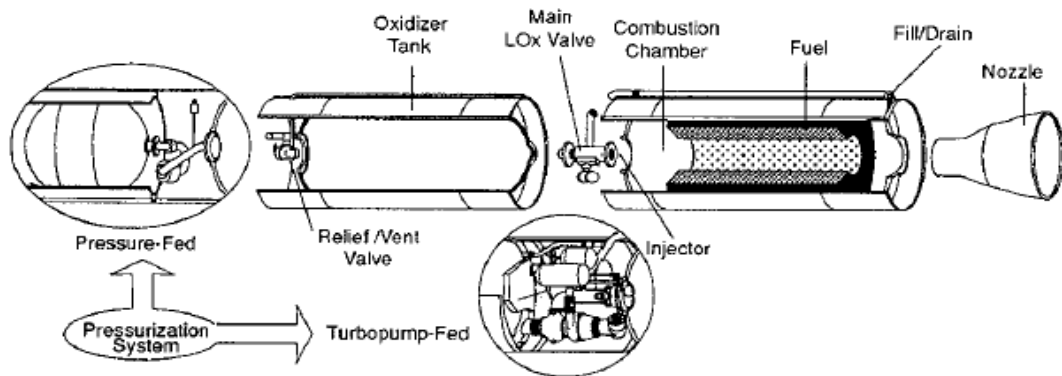
Figure 1: Hybrid propulsion engine for LOX

The Fig.1 represent the classic configuration and the main components of an hybrid engine which are:

- The oxidizer tank which contains the gas or the liquid under pressure.
- The injection valve: it commands and regulates the flow of oxidizer into the combustion chamber.
- The igniter, possible in different types and configurations, responsible of starting the combustion.
- The combustion chamber which is where effectively the grain solid fuel is stored. The presence of one or more hole with different geometry guarantees a place where the combustion actually happens.
- The nozzle able to generate thrust by the acceleration of the exhaust gases.

The operation principles of a classic hybrid engine is based on the combustion of a solid fuel by a liquid or gaseous oxidizer. The oxidizer tank is under pressure and at the extremity of the tank an injection valve open and close the circuit permitting to regulate the flow rate into the combustion chamber and then the thrust. Usually when the valve is open to permit the flowing towards the combustion chamber, an expansion of the oxidizer occurs.
The fuel is stored into the combustion chamber with the shape of an hollowed cylinder. The port for the combustion could have various shape and geometry, shown in Fig.4, giving different combustion properties. Between the valve and the fuel solid grain there is the igniter, which could be electric or pyrotechnical, with the aim to give the needed energy to start the combustion.

The gas mixture flows through the nozzle which transforms the enthalpy energy into kinetic energy and generates thrust. The oxidizer passes throw the perforation of the fuel grain and, when there are the right conditions of temperature and concentration of chemical species, a diffusion flame starts.

The injection of the oxidizer into the combustion chamber can be done by using turbo-pumps, with the aid of an inert gas that gradually goes to fill the tank pushing the oxidizer outside or moreover, just taking advantage of the high pressure of the fluid inside the tank. The choice between these methods is driven by the engine's dimension [18]: on small engines, using turbo-pumps would have no sense because of their low efficiency due to scale effects. Meanwhile on big engines tanks under pressure aren't used because the weight of the inert gas and the increased tank weight would bring to a decrease of the propellant mass fraction.

The combustion area is concentrated into the boundary layer created by the flow of the injected oxidizer in the fuel regression surface where the solid fuel is gasified. The fuel combustion is radial and the flame is created in the hole and moves radially outward uniformly reducing the grain thickness up to consume it all.

The boundary layer structure is shown in some schlieren photos (Fig.2) relative to the combustion of Plexiglas in oxygen atmosphere. Based on those photos and on the considerations about the combustion model, a representative scheme of the hybrid combustion model is given by the Fig.3:
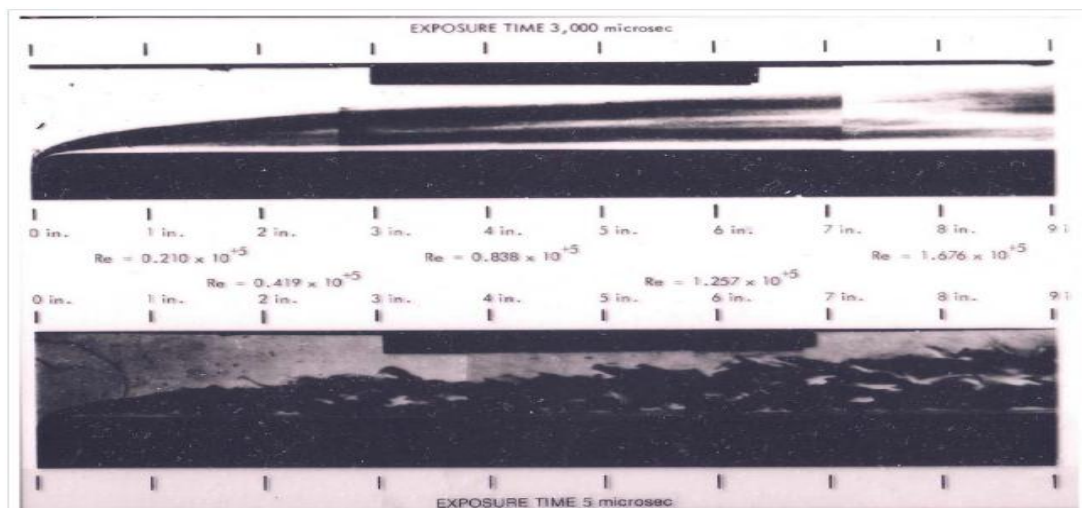
Figure 2: Schlieren image of hybrid combustion [16]
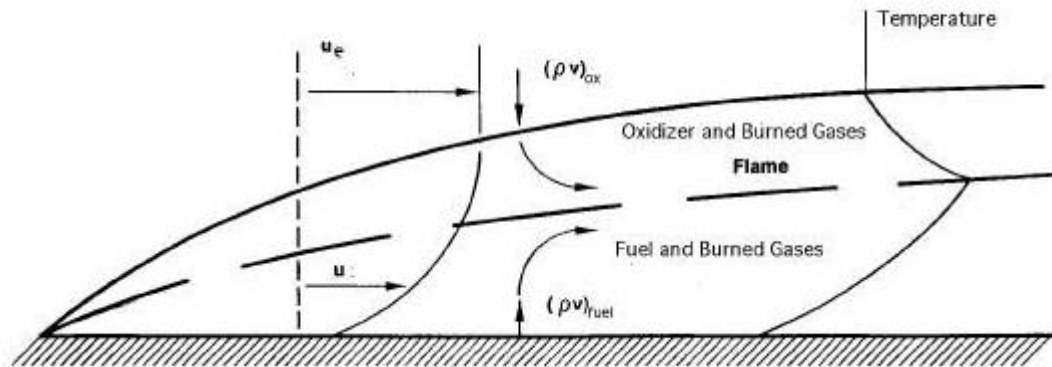
Figure 3: Hybrid combustion model [16]

The flame is macroscopically diffusive and insensitive to operating conditions, because it is not controlled by chemical kinetic laws, but by fluid dynamics ones. The process of hybrid combustion is powered by the return of thermal energy, convective and radiative of the flame to the solid grain. This energy payback allows the gasification of the fuel fresh mass, and therefore, with the continuous and simultaneous injection of liquid oxidizer, the maintenance of the flame. Ideally, the diffusive flame is like a veil or a thin layer, located into the fluid dynamic boundary layer, where is reached the stoichiometric ratio between the gasified fuel and oxidizer injected. Actually, the flame thickness is increased to a discrete measure, due to the good reactivity of the reagents and the discrete reaction speed. The thickness is limited by the reciprocal flammability limits of the reagents. The combustion products are transported downstream by the convective flow, mixed with the fuel under the flame and the upper oxidizer. Referring to Fig.3, while the speed u monotonically increases from the wall value to the free stream value u_e, the temperature passes from the wall value T_w to the free stream value T_e with a maximum in correspondence of the flame veil. The reverse configuration has rarely been used because of poor quality of combustion considered rough (stable, but oscillatory), and because of the performances which are insufficient compared with the difficulties encountered for the compression of the solid oxidizer. However, some military applications have been done.

1.3. Configuration and main applications

The classic configuration for an hybrid rocket engine consists of a liquid oxidizer and a solid fuel but there is the possibility to have also the opposite configuration with solid oxidizer and liquid fuel. This kind of system is called

reverse hybrid. The pioneers of this in 1952 were Dembrow and Pompa [17]. They developed the first hybrid engine with reverse configuration, using JP as liquid fuel and several solid materials as oxidizers, chosen mostly for low costs reasons. The reverse hybrid configuration was considered unattractive because of its poor combustion quality and low performances to justify the difficulties encountered to realize it, but there are some military applications.

The versatility of hybrid propulsion produced a broad variety of application using this technology and then, the interest in this field is now very high due to numerous studies and successful missions (among them the important suborbital accomplished mission of Space Ship One).

At the moment a lot of studies are focused to characterize hybrid propulsion with appropriate metallic additives with the possibility to improve the performance in terms of specific impulse and combustion stability.

Hybrid propulsion finds a lots of application in sounding rockets by the main customers Onera and Volvo Flygmotor. It is possible to consider also military application which involves hybrid propulsion, in particular target drones or tactical motors. Among the various applications for which the hybrid propulsion could be advantageous, stand out the high energy space engines, boosters for space launchers and orbital maneuvers for small satellites [16]

The revival interest in the hybrid propulsion in the last decades could be found in the main reason [16]: the growing business worldwide in commercial satellites which stimulated many industrialized nations to build their own version of a space vehicle capable to place payload in orbit. This caused a competition in the research for a low coast approach to launch space vehicles. The second reason is the need of safety and efficient propulsion system emerged after the catastrophic failures of both space flight Challenger and Titan III.

1.4. Advantages and disadvantages of hybrid propulsion

The choice to place efforts in the research and development of hybrid propulsion is due to the broad advantages of this technology in comparison with the well known liquid and solid propulsion. It combines the benefits of liquid engines (thrust regulation, shut down and restarts) with the benefits of management and costs of solid engines. In detail [17]:

- Intrinsically safe: only inert materials are used in the phase of manufacturing, assembling, transportations and pre-launch operations without specific security recommends. Accidental ignitions, common in solid propellant, are impossible before the injection of the liquid component in the combustion chamber and, in case of emergency, it is

possible to shut down the motor interrupting the flow of the liquid oxidizer.

- Flexibility: typical of liquid propulsion, the hybrid propulsion is characterized by throttling thrust easily regulating a valve which control the oxidizer's flow in the combustion chamber. The ignition is hypergolic and then simple and immediate. The hybrid engines can be restarted several times until the fuel grain is over or the nozzle has reached its project limit in terms of ablation or debris accumulation.
- Reliability of operation: hybrid engines are more complex then solid engines because of the presence of the distribution and injection system, but they remain really less complex then liquid engines which need more complicated injection plates and distribution systems. It can be considered very simple propulsion system. In comparison with solid propellant, the hybrid propellants are less thermal sensitive and then more stable. The manufacturing defects are well tolerated and do not affected the performance of the propulsor.
- Versatility in the choice of propellants: it is possible to burn more or less everything using hybrid propulsion technology. Many were the experiments using waste products generated in the ISS (paper, human waste, uneated food…) and some tests are performed also using Italian salami [16]. At the moment the major grains used are polyethylene, resin and HTPB with high mechanical properties and specific impulse.
- Performance: the specific impulse of hybrid engine is equivalent to that of a liquid fueled engine using RP-1 and LOX, and it's higher than the specific impulse of a solid engine. Moreover, in theory the couple FLOX-Li and the triple hybrid LOX-(Be+H_2) offer the best combination into the thermo-chemical field.
- Cost: the management and construction processes are less expensive than in liquid or solid cases.
- Environmental impact: using appropriate propellants, the impact in the environment during the launch and flight is relatively small.

Despite all the benefits here described, hybrid propulsion presents also some disadvantages that are of less importance and impact in comparison with the advantages.

- Regression rate: it is low and not so much sensitive to the operational conditions which lead to a larger combustion surface, obtainable by increasing the holes in the solid grain, but which determinates an increase of the engine's cross section.
- Scaling: the performances of big systems are worse than small scales motors.

- Low combustion quality: in comparison with solid and liquid propellants combustion (η=98-99%), the hybrid combustion efficiency is quite low (η=95%).
- Longitudinal instability: it's the only type of instability that affects hybrid engines, but it could be dangerous due to its intensity.
- Variation of the mixture ratio during the combustion due to the increasing burning surface. This can be however handled by a proper design of the solid grain or varying the oxidizer mass flow, in order to maintain the same mixture ratio, as shown in the Fig.4.
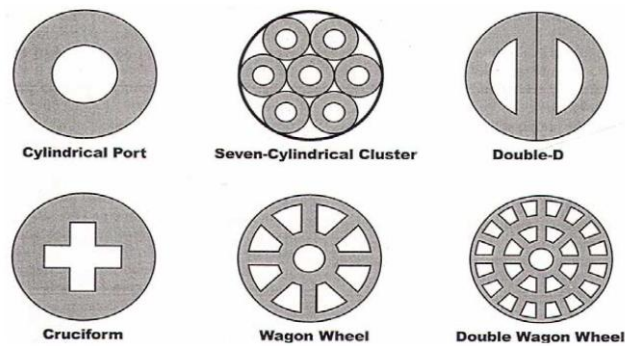
Figure 4: Geometry of the grain for solid fuel

2. Introduction to turbulent model

In the study of turbulent flows the primary and final objective is to obtain a reliable quantitative theory and model that can be used to calculate quantities of interest and practical relevance. With this purpose, it is worthwhile to reflect on the particular properties of the turbulent flows that make difficult to develop an accurate turbulent theory and model.

Considering this kind of phenomena, the largest turbulent motions are almost as large as the characteristic width of the flow and consequently are directly affected by the boundary geometry. There is also a large range of timescales and lengthscales to identify the phenomena inside the turbulent flow. The most important difficulties in the definition of turbulent problems arise from non-linear convective term in the Navier-Stokes equation, and much more so from the pressure-gradient term.

In general, in a turbulent flow simulations, equations are solved for a time-dependent velocity field that represent the velocity field of the turbulent flow.

According to the numerous different situations which involve turbulent analysis, a wide range of model and algorithm have been proposed and many are currently in use. It is important to appreciate that there is a broad range of turbulent flows and also a broad range of questions to be addressed. Consequently it is useful and appropriate to have a wide range of models that vary in complexity, accuracy and other attributes. The main features which define and diversify all the models are [13]:

- Level of description: an high level of description of the flow can provide a complete characterization of the turbulence, leading a model of wider accuracy and applicability;
- Completeness: a model is considered complete if its constituent equations are free from flow-dependent specifications. One flow is distinguished from another solely by the specification of the material properties and of initial and boundary conditions.
- Cost and ease of use: the difficulty of performing turbulent model calculations depends both on the flow and on the model. The computational difficulty increases with the dimensionality of the problem. Of course the cost and the difficulties to perform the computation depend strongly on the scale of the computer required, on the amount of human time and skill needed to perform the computation. In terms of machine time consumption, 25 hours of CPU time on a workstation is reasonable [13];
- Range of applicability: not all the models are applicable to all the flows. A model is applicable to a flow if the model equations are well posed and can be solved irrespective of whether the solutions are accurate;

- Accuracy: it is a desirable attribute of any model. In application to a particular flows , the accuracy of a model can be determined by comparing model calculation with experimental measurements. This process of model testing is of fundamental importance and deserves careful consideration. As shown in the Fig.5, the process consists of a number of steps, several of which introduce errors.
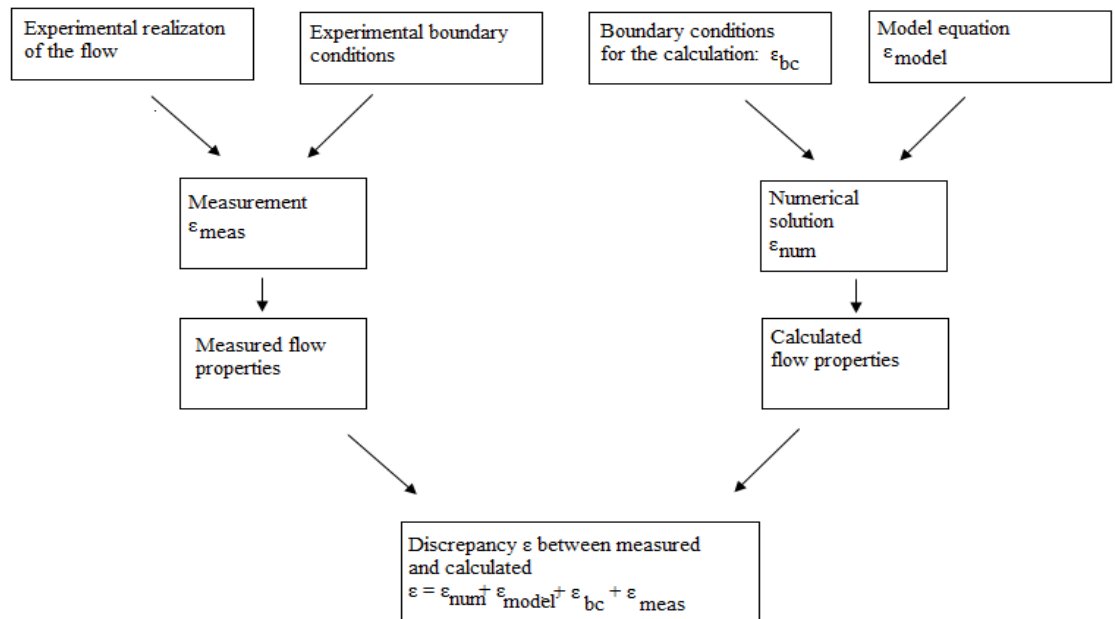
Figure 5: Schematic illustration of accuracy of the model

For a number of reasons, the boundary conditions in the calculations need not correspond exactly to those of the measured flow and they will not necessarily be known and so have to be estimated or taken from experimental data that contain some measurement errors. Numerical solution of the model equations inevitably contains numerical error and errors could occurs also simply because the calculations and the model are performed with insufficient care. The comparison between measured and calculated flow properties determines the accuracy of the model only if the numerical, measurement and boundary conditions errors are relatively small.

The suitability of a particular model for a particular turbulent flow problem depends on a combination of the criteria discussed above, which depends on the problems. Consequently, there is no one "best" model, but rather there is a range

of models that can be usefully be applied to the broad range of turbulent flow problems.

Once described the main features to define a model, it is possible to affirm that each model does not work in the same way for the same problems. Therefore, there are different approaches to solve turbulent flow:

- the direct numerical simulation in which the Navier-Stokes equations are solved to determine the instantaneous velocity field of the flow. All the lenghtscales and timescales have to be resolved and then this method is computationally expensive, depending of the cubic power of Reynolds number. This method is used only to flow with low-to-moderate Reynolds number;
- the Large Eddy simulation approach (LES) which resolve a velocity field representative of the larger scale turbulent motions. The solver equations included also a model for the influence of the smaller scale motions which are not directly represented;
- Reynolds Averaged Navier-Stokes (RANS) model involves the solution of the Reynolds equations to determine the mean velocity field. In particular, the turbulent viscosity model can be obtained from an algebraic relation or it can be obtained from turbulence quantities for which modeled transport equations are solved.

In particular the attention of this report is focused on the RANS turbulent viscosity models which included, in their wide range, also the Spalart Allmaras Original Model (SAO) used in the numerical simulation for the resolution of turbulent flow of the micro hybrid thruster under analysis.

2.1. Spalart Allmaras Model

The RANS models consists of Reynolds equations solved for the mean velocity field of the flow. The Reynolds stresses, unknowns in the Reynolds equations, are determined by a turbulence model, either via the turbulent viscosity hypothesis of more directly from modeled Reynolds stress transport equation. Turbulent viscosity models are based on the turbulent viscosity hypothesis which are not here reported but they are easily research in literature [13].

Among all the RANS model based on the turbulent viscosity, it is possible to consider the Spalart Allmaras model that is a one-equation model developed mostly for aerodynamic applications in which a single model transport equation is solved for the turbulent viscosity v_t.

It is useful to appreciate the context of the development of the Spalart Allmaras model. There is a natural progression in the algebraic, one-equation and two-

equation models. If accuracy is the only criterion of the selection of models for development and application, then the choice would naturally tend toward the models with the higher level of description.

However as discussed before, cost and ease of use are also important criteria that favor the simpler models. Probably, a one-equation model for v_t is the lowest level at which a model can be complete. Spalart and Allmaras developed the model to remove the incompleteness of algebraic and one-equation models to have a model computationally simpler than two-equation models [13].

As told, the SAO model is based on transport equation for the calculation of turbulent viscosity. The model equation includes a destruction term that depends on the distance of the wall.

Unlike early one-equation models the resulting turbulence model is local (i.e. the equation at one point does not depend on the solution at other points), and therefore compatible with grids of any structure, also unstructured ones, and Navier-Stokes solvers in two or three dimensions [14]. It is numerically forgiving, in terms of near wall resolution and stiffness, and yields fairly convergence to steady state.

The wall and freestream boundary conditions are trivial. The models yields relatively smooth laminar-turbulent transition and satisfactory predictions of boundary layers in pressure gradients.

The SAO model is a more onerous than algebraic models but with a wider envelope in terms of flow and grid complexity. The algebraic models sometimes is not optimized for unstructured grid, the e-k model is usually local and requires a finer grid near wall and involve strong source terms that often degrades the convergence. All the others one–equations models are not local and they use length scales related to the boundary layer thickness , than is possible to suppose that one-equation models are not complete.

The choice of using this model for the resolution of the simulation of this report, is due to the fact that the SAO model is a complete model, the lowest level at which a one-equation model can be complete and it provides decent performances and results besides the fact that the computational cost to solve the problem with this method is reasonable. The solvering scheme of the problem here discussed, is presented in the next chapters but it is possible to anticipate that the entire simulation needs about 7 hours to complete, giving a good convergence and values of y^+ more than acceptable.

The center quantity of the SAO model is eddy viscosity v_t. The Reynolds stresses are given by

$$- \overline{u_i u_j} = 2 v_t S_{ij}$$

where

$$S_{ij} \equiv \left(\frac{\partial U_i}{\partial x_j} + \frac{\partial U_j}{\partial x_i} \right) \Big/ 2$$

is the strain-rate tensor. Compared with two-equation model, there is not the term k (turbulent kinetic energy). In the one-equation models which produces v_t but not k, there is also a rough approximation of k as proportional to the stresses given by $v_t S_{ij}$.

All the terms at the basis of the SAO model are derived from v_t, invoking common notions of turbulence to assemble dimensionally correct terms that together can constitute a plausible transport equation for v_t.

The left side of the equation is the Lagrangian of v_t:

$$Dv_t \big/ Dt = \partial v_t \big/ \partial t + U_i \, \partial v_t \big/ \partial x_i$$

On the other side of the equation there is a production and diffusion terms. The production term is given by $v_t S_{ij}$ which consider also the vorticity:

$$\omega \equiv \sqrt{\Omega_{ij}\Omega_{ij}}$$

where

$$\Omega_{ij} \equiv \partial U_i \big/ \partial x_j - \partial U_j \big/ \partial x_i$$

In the flow of interest turbulence is found only where vorticity is, both emanating from the solid boundaries. Then, the production term which restrict the model to homogenous turbulence is:

$$Dv_t \big/ Dt = c_{b1} S v_t$$

where the term v_t varies according to the different kind of flows and c_{b1} has a value between 0.13 and 0.14.

The diffusion term is naturally focused on spatial derivatives of v_t and the classical diffusion operator is ∇. This is a non-conservative diffusion term involving first derivatives of v_t.

Then, it is possible to assemble all together and the basic Spalart Allmaras model is given by the following equation [14]:

$$D\nu_t / Dt = c_{b1} S \nu_t + \frac{1}{\sigma_P}\left[\nabla\cdot(\nu_t\nabla\nu_t) + c_{b2}(\nabla\nu_t)^2\right]$$

with σ_P turbulent Prandtl number and $c_{b2} \leq 1$. The first addend of the expression is the production term and the second the diffusion one. This model is essentially insensitive to non–zero values and this could help some numerical solvers.

Taking into account many others conditions, the model could include also a destruction term for the Reynolds shear stress which lead to a more complex and complete SAO model with the following equation:

$$D\nu_t / Dt = c_{b1} S \nu_t + \frac{1}{\sigma_P}\left[\nabla\cdot(\nu_t\nabla\nu_t) + c_{b2}(\nabla\nu_t)^2 - c_{w1} f_w \left[\frac{\nu_t}{d}\right]^2\right]$$

where f_w is a non-dimensional function, d the distance to the wall and some constants have to be defined:

$$c_{b1} = 1.355 \qquad \sigma = 2/3 \qquad c_{b2} = 0.622 \qquad k = 0.41$$

$$\sigma_P = 0.9 \qquad c_{w1} = \frac{c_{b1}}{k^2} + \frac{1 + c_{b2}}{\sigma}$$

The boundary conditions to solve the equation are set by defining values of ν_t and in particular near the wall it is ideally $\nu_t = 0$.

The contribution of all the terms of the model equation is given in the Fig.6 where it is possible to recognize the budget of ν_t, whit the contribution of the production, destructive and diffusion terms.
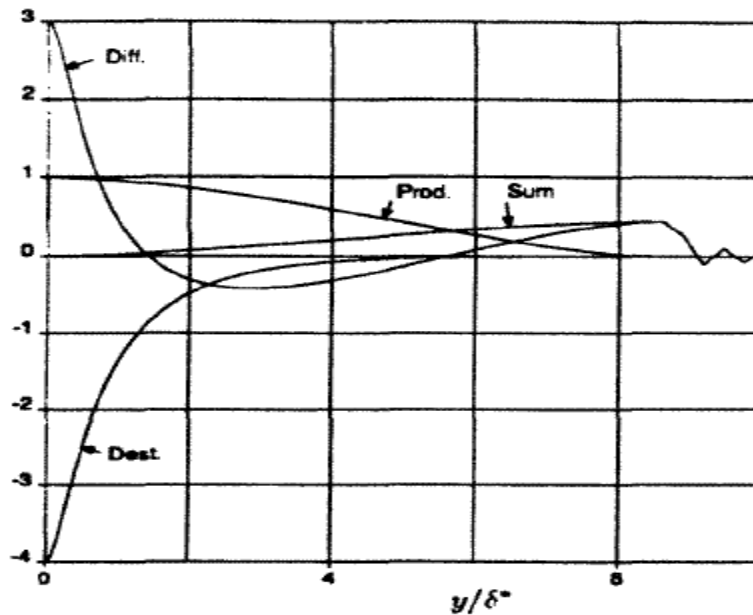
Figure 6: Eddy-viscosity budget in a flat-plat boundary layer. [14]

There are a large number of different SAO models depends on which terms are considered in the analysis, the condition of the flow and the boundary condition. In this study the Spalart Allmaras basic model, shortly described here, is used. The complete and deep analysis of this model is a bit complex then for further details in addition to those here presented, and for the description of other variants of the basic model, refers to the original paper [14] which provides an enlightening account of the construction of the model to achieve particular desired behaviors.

2.2.   Near-wall consideration

According to the theory presented by [13], close to the wall of the section the viscosity and the wall shear stress are important parameters. From these two quantities it is possible to define viscous scales that are the appropriate velocity scales and length scales for the near wall region. These are the friction velocity and viscous length scale.

A strategy for dealing with turbulent flows over a two dimensional surface mounted obstacle using the wall y+ as guidance in selecting the appropriate grid configuration and corresponding turbulence models are investigated deeply in [15].

The non-dimensional distance from the wall measured in viscous lengths, or wall units, often used in CFD to describe how coarse or fine a mesh is for a particular flow, is denoted by:

$$y^+ = \frac{y}{\delta_v} = \frac{u_\tau y}{\nu}$$

where δ_v is the viscous length scale and u_τ the friction velocity, y the distance of the nearest wall and ν is the kinetic viscosity of the fluid. Accurate presentation of the flow in the near-wall region determines successful prediction of wall-bounded turbulent flows.

Its magnitude can be expected to determine the relative importance of viscous and turbulent process.

This value would require a very fine mesh near the wall in order to resolve the turbulent eddies in the boundary layer, considering that turbulence models deal with the flow in the boundary layer. The boundary layer is divided into an inner and outer region, and the inner region can be further subdivided into a laminar (viscous) sublayer and a fully turbulent region. The inner region is referred to the "law of the wall zone" and it is characterized by a log-linear variation of the non-dimensional velocity $u+$. The viscous sublayer where $u^+ = y^+$, is the region between the wall and the first grid point of the geometrical mesh of the model. If the created mesh is too fine near the wall, a low value of y^+ occurs. This will result in overprediction of the near wall velocity. On the other hand, if y^+ is too high, it will cause the code to apply the law of the wall where it is not valid. The main factors that affect the y^+ are the Reynolds number, surface roughness and adverse pressure gradient.

Using the Spalart Allmaras model, the y^+ has to be in the order of 1 or larger than 30, then the grid is considered fine. If not, the grid needs modification.

In general, the non-dimensional wall y^+ is a suitable selection criterion for determining the appropriate mesh configuration and turbulence model.

For a good resolution of the grid and a good solution of the problem, the value of y^+ could be equal to the unit. In this case the grid is sufficiently fine to resolve the inner parts of the boundary layers, otherwise it is possible to occur into problems with convergence of the method and correctness of the solution.

In the next chapters, the y^+ trend is presented for each analysis, confirming the goodness of the mesh and the model used.

3. Geometry, mesh and CFD simulation

The first step of the study here conducted is the realization of the numerical model of the micro hybrid thruster (MHT) to understand and investigate the behavior of the exhaust gases starting from the analysis of the nozzle. Then, it is necessary to generate an adequate mesh consdering the geometry of the nozzle and define the physical model together with the boundary conditions for the resolution of the problem with the use of specialized software.

The numerical study of the micro hybrid thruster´s exhaust gases under examination is made by using DLR Tau code software, whose main modules are the preprocessing, flow solver and adaptation. It is a powerful software to study and predict the viscous and inviscid flows behavior in complex geometries from subsonic to hypersonic flow regime, employing hybrid unstructured grids. Tau code, designed for massively parallel computations, is not able to generate a grid but comprises tools for its modification, adaptation and deformation.

For that reason, a geometry input file is realized using Centaur software, able to realize a high quality hybrid grids consisting of a mixture of prisms, hexahedra, tetrahedral and pyramids. Starting from the grids, Centaur creates a mesh according to automatically or user-specified inputs and regions of interest.

In the case of micro hybrid thruster studied, the geometry is realized from the technical drawing shown below:
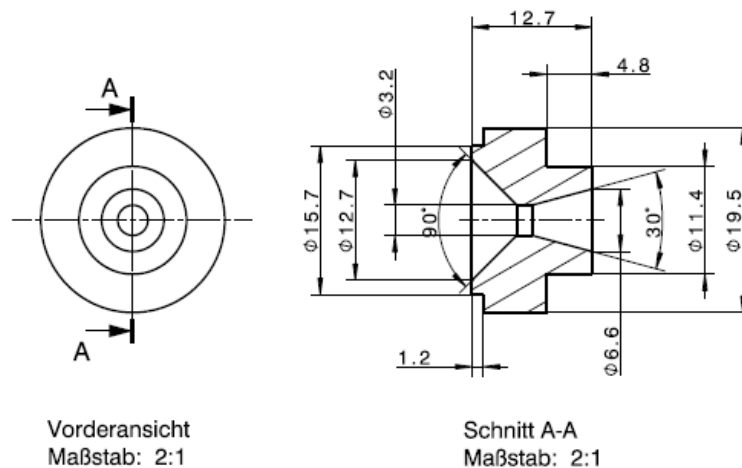
Figure 7: Technical drawing of the nozzle

Considering the symmetry of the nozzle, only half of the whole structure is modeled, generating a symmetry plane for the "mirroring operation" in the post processing visualization. It is a convergent-divergent nozzle.

It is necessary to define a very large farfield with dimensions 1000x2500 mm, much bigger than the longitudinal dimension of the nozzle equals to 9.75x25.4 mm. These in order to permit the complete expansion of the flow below the nozzle, without any kind of interference with the surrounding environment.

The reference system of the nozzle, valid for the whole essay, has the X-axis along the symmetry one and the zero is at the beginning of the combustion chamber, the Z-axis upwards from the symmetry axis and the third Y-axis is binormal to both according to the right-hand rule.
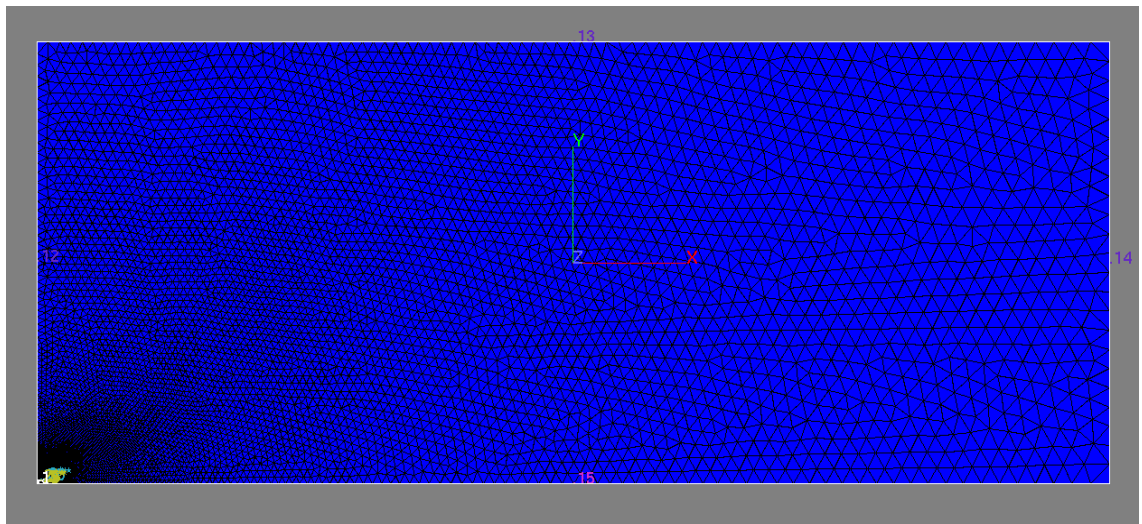
Figure 8: Farfield environment

Different layers are created to distinguish the different areas of interest and to adapt the mesh in these critical zones, where most likely will be high gradient of the values. This has been subsequently confirmed by calculation with Tau code. The created layers are:

- farfield: all the area far away from the nozzle;
- inlet: the area through which the flow enters into the nozzle;
- symmetry: the plane of symmetry;
- nozzle Inside: the whole area inside the nozzle;
- nozzle Outside: the near area outside the nozzle.
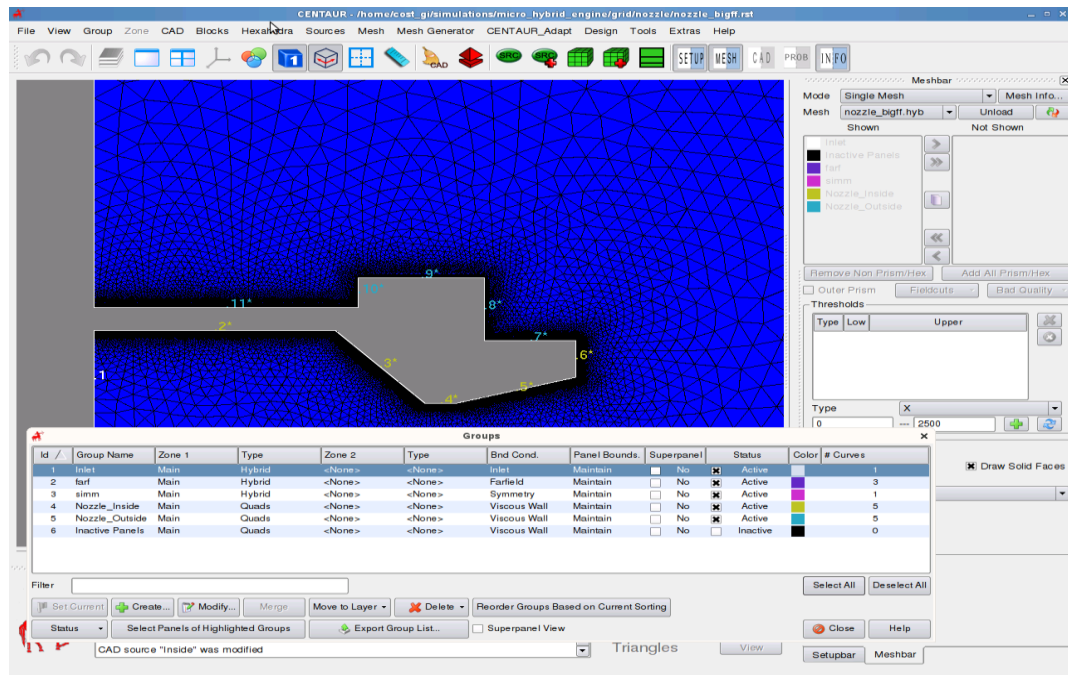
Figure 9: Definition of layers

The main layers are inlet, inside and outside nozzle where an adapted mesh was realized. The cells present a very small dimensions at the edges of the nozzle or near the curvatures and narrowing (i.e. the throat) but, going away more and more, they become bigger, as it is possible to see in the detail below.
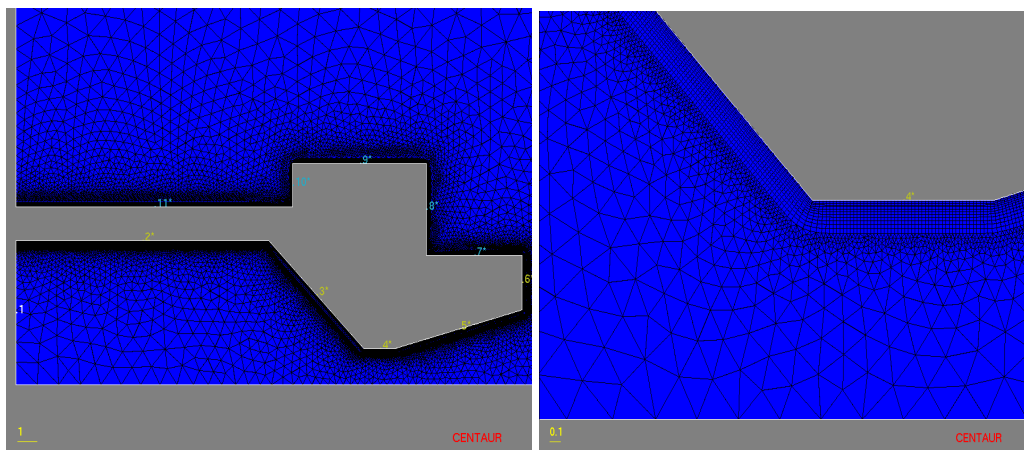
Figure 10: Complete mesh and detail in the throat

Of course the area far away from the nozzle is not so detailed and full of elements, which are bigger than the others.

The resulted mesh presents the following characteristics:

Nodes	30507
Total elements	45108
Quads	14280
Tria	30828

Table 2: Mesh characteristics with Tau code model

This grid file, generated with Centaur, is an input for parallel computation in Tau code. The grid is partitioned in the requested number of domains, defined by user, at the start of the simulation. Therefore a simple bisection algorithm is employed.

After the partitioning, all the modules of Tau compute the requested data for a single domain per process and it is the same for all the others. Grid re-partitioning is performed either if the grid was locally (de-)refinement in an adaptation or if the number of domains is changed [7].

In order to efficiently resolve detailed flow features and obtain accurate results in particular areas, a grid adaptation algorithm based on local grid refinement is used. According to this tool, the grid is automatically adapted to the gradients in each time step, both creating and deleting elements with a percentage of new points of 50%, where the values are very sensitive. This operation allows better resolution at the cost of additional time.

Four local adaptations are necessary for the MHT model to find a right compromise between computational time and accuracy in the results (see Chap.4 for convergence of the method). The area of interest is the whole region inside the nozzle till a distance of 75 mm from the exit to have a correct definition of the exhausts.
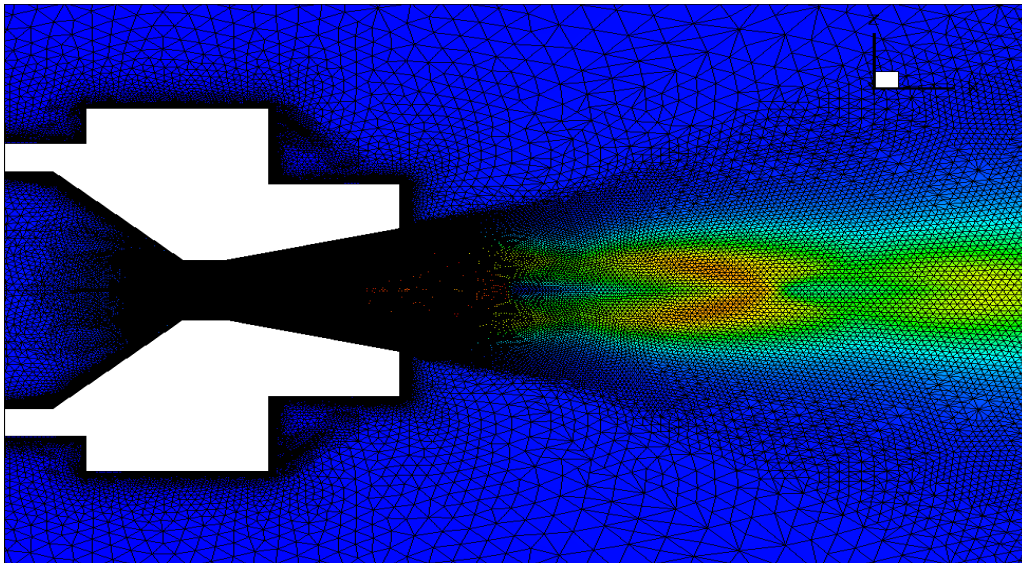
Figure 11: Mesh adaptation

3.1.   Courant Friedrichs Lewy number and simulation logic

A CFL (Courant-Friedrichs-Lewy) loop for each adaptation is used to reduce the errors of computation and make the y$^+$ value (a non-dimensional wall distance for a wall-bounded flow, details in Chap.2.2) as much as possible close to 1, that is the desirable value for a good mesh resolution and a convergent solution in a near-wall modeling [22].

The CFL number, defined as a necessary condition for convergence while solving certain partial differential equations (usually hyperbolic PDEs) numerically by the method of finite differences [23], has the following expression:

$$CFL = \frac{\Delta t}{\Delta x} a \le CFL_{max}$$

where Δt and Δx are respectively the time step and the length interval, and a the velocity of the flow. The time step must be less than a certain time in many explicit time-marching computer simulations, otherwise the simulation will produce incorrect results. In essence, the numerical domain of dependence of any point in space and time (which data values in the initial conditions affect the numerical computed value at that point) must include the analytical domain of dependence (where the initial conditions has an effect on the exact value of the solution at that point) in order to assure that the scheme can access the information required to form the solution.

The value of the CFL_{max} depends on the used method to solve the discretized equation. For explicit schemes is typically $CFL_{max}=1$ while for implicit solver larger values of CFL_{max} are used because they are less sensitive to numerical instability.

The CFL loop used consists of changing the value of the CFL number in the parameters file for Tau code input (the complete parameter file is in Appendix B), from 0.25 to 2 in 4 steps to guarantee a better convergence for each step. This loop considers also to vary the parameter "CFL number (large grad p)" used in the presence of large pressure gradient (i.e. shocks) increasing the stability of the scheme.

Then a total of five loops and four adaptations are necessary for the MHT model.

	CFL NUMBER	CFL NUMBER (LARGE GRAD P)
1 LOOP	0.25	0.05
	0.5	0.1
	1	0.2
	2	0.4
	ADAPTATION	

Table 3: Loop scheme

To verify the usefulness of these loops the value of y^+ should be around 1, like is shown in the following graph.
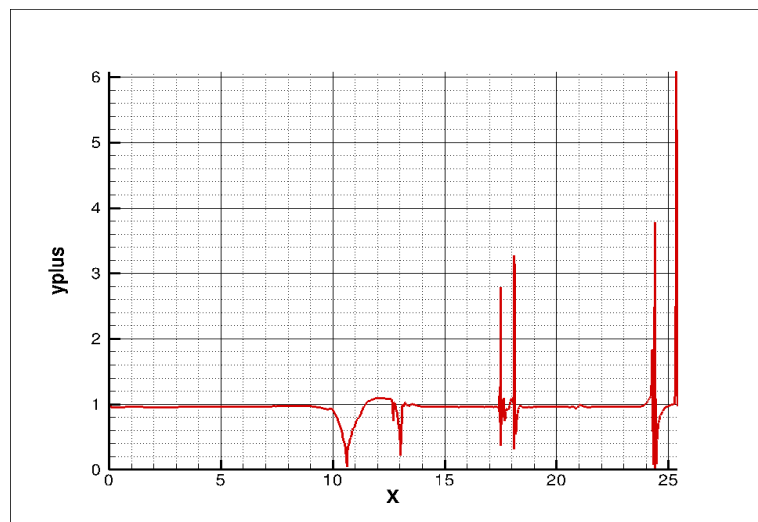
Figure 12: y^+ trend in the nozzle

The presence of the peaks is due to the shocks. Beside the peaks, the mesh can be considered suitable.

3.2.   Tau code basics and parameters

In order to completely describe the flow field, a wide range of turbulence models are available in the Tau code, ranging from simple algebraic approaches to full Reynolds-Stress Transport models linear as well as non-linear eddy viscosity models spanning both one- and two-equation model families (i.e. Explicit Algebraic Stress Models, Reynolds stress transport models, such as flow scales Detached Eddy Simulation and Large Eddy Simulation models). [7].

In the case under analysis, to compute the flow behavior a RANS turbulence model is chosen, which represents also the natural mode of operation for Tau code. In particular the standard one-equation eddy viscosity Spalart-Allmaras model (SAO), is used yielding highly satisfactory results for a wide range of applications while being numerically robust and not so demanding in terms of computational time. For further details about SAO model read [7] and [14] and Chap.2.1.

For the discretization of the convective fluxes of the RANS and turbulence equations, an upwind scheme is used for the resolution of the MHT study. The implicit Backward-Euler method is the scheme for time-stepping solution, consistent with the choice of using the SAO model.

However, this simulation with Tau code does not assume any combustion model for the mixture flow. This is a limitation which implies the study of a frozen flow along the nozzle without considering any combustion products. This means that it is necessary to give, as input to Tau code, the correct thermodynamic values of gas constant R and isentropic expansion factor γ of the mixture flow after the reaction in the combustion chamber. These two values are not so easy to define because it needs to understand how the reaction between the compounds develops.

Before talking about it, it is possible to set other thermodynamic values such as necessary for the numerical analysis:

Chamber Temperature	2000 K
Chamber pressure	$12*10^5$ Pa
Reference Temperature	300 K
Reference Pressure	101325 Pa

Table 4: Thermodynamic values

These informations are defined in the parameters and boundary conditions files, both necessary for Tau Code running.

They are set considering the chamber pressure equals to the inlet one of the nozzle, as well as the temperature. In general the nozzle inlet is the end of the combustion chamber (after chemical reaction between reactants has occurred), so all the values from the chamber are the same for the inlet. Of course the flow velocity in the chamber is zero, so it is supposed to be stationary in that area.

An important assumption is made: the gases are ideal so it is possible to use the ideal gas law.

3.3.   Accuracy and preliminary check of CFD model

A series of simulations is performed to figure out if the model built is correct or it needs some refinement. Because of the exact values of the gas constant R and isentropic factor γ were not yet available at the first phase of the study, different sets of constants are used for different simulations: with fixed gas constant R (188.9 J/KgK) three values of isentropic factor γ (1.1, 1.5, 1.27) and with the same value of γ (1.27) three values of R (150, 188.9, 296.8 J/KgK).
Of course the density of the flow is evaluated and changed in the boundary condition file, according the gas perfect law.

R [J/KgK]	γ
150	1.27
296.8	1.27
188.9	1.27
188.9	1.5
188.9	1.1

Table 5: R and γ values analyzed

This yield to a first interesting result: the variation in the value of R constant, with a fixed $\gamma = 1.27$, produces a difference in the exhausts mass flow. The phenomena appear to be the same but scaled, due to the different mass flow operating. Otherwise, with a fixed value of R (188.9) and different γ, the mass flow is the same but now the behavior of the gas changes: the more γ is high, the more the separation of the flow from the nozzle moves inside of it.
In any case the temperature trend follows the Mach number one.
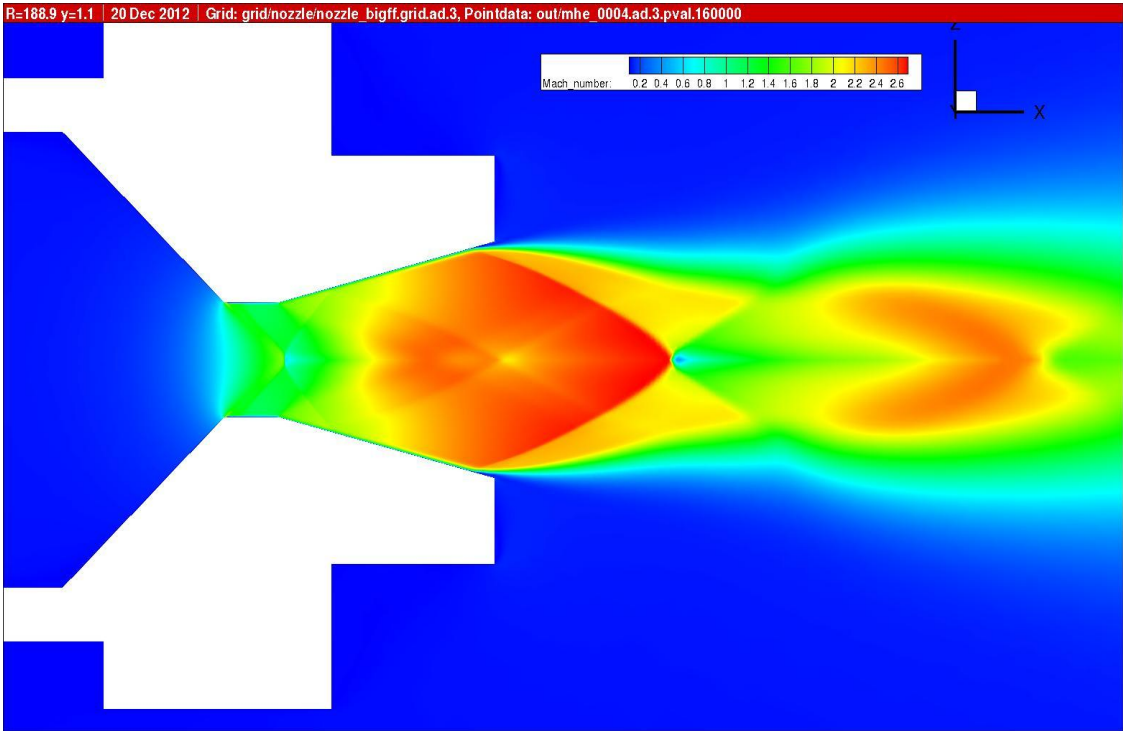
Figure 13: Tau code calculation of Mach number. R=188.9 J/KgK γ =1.1
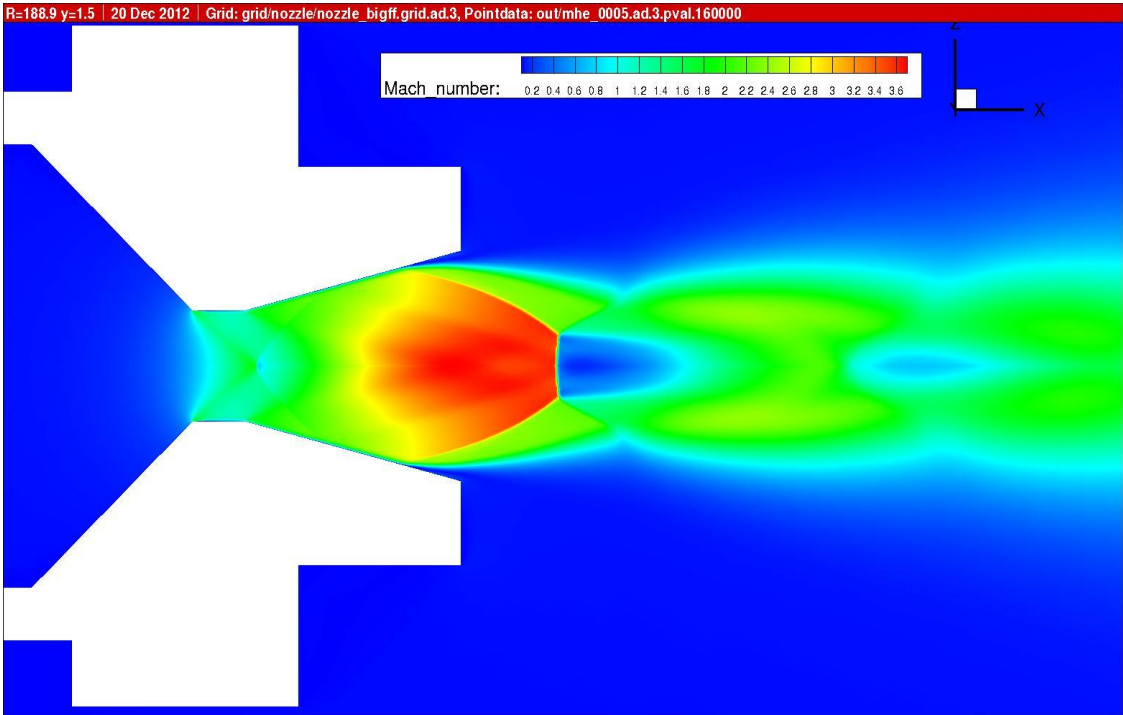
Figure 14: Tau code calculation of Mach number. R=188.9 J/KgK γ =1.5
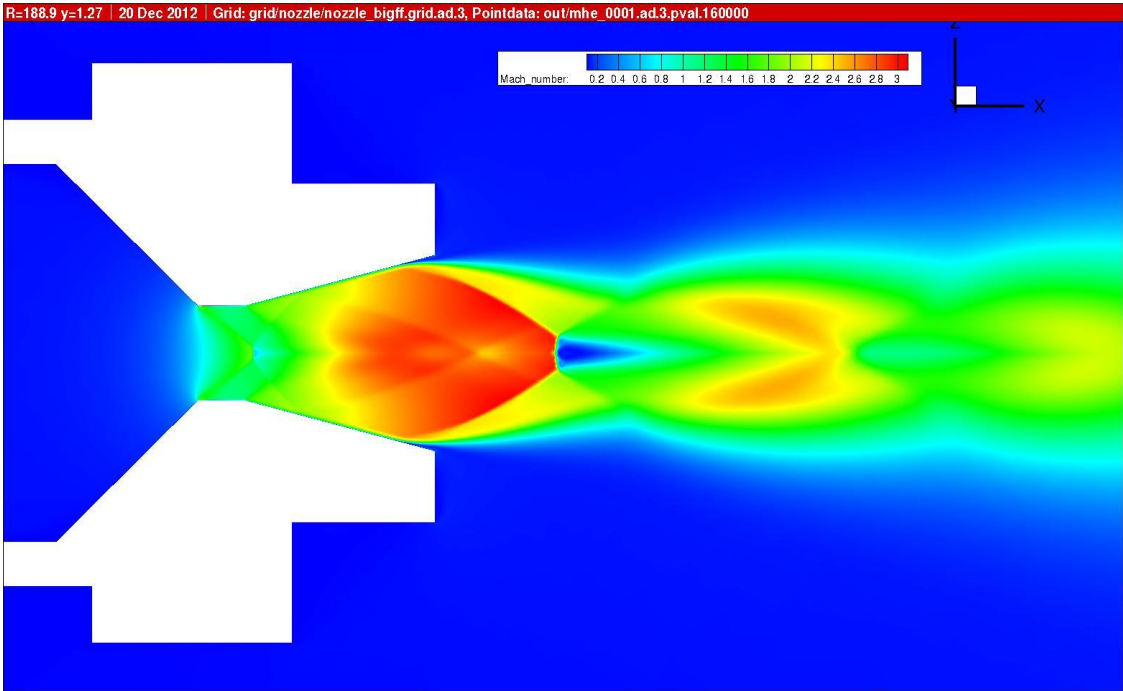
Figure 15: Tau code calculation of Mach number. R=188.9 J/KgK γ =1.27
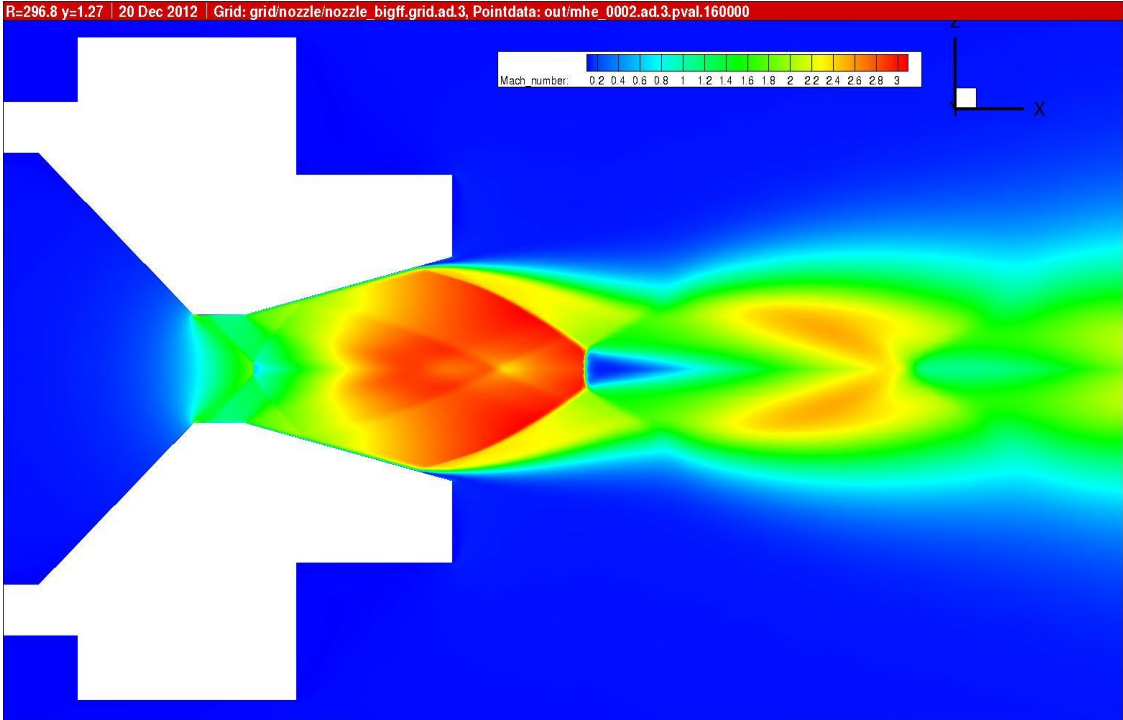
Figure 16: Tau code calculation of Mach number. R=296.8 J/KgK γ=1.27
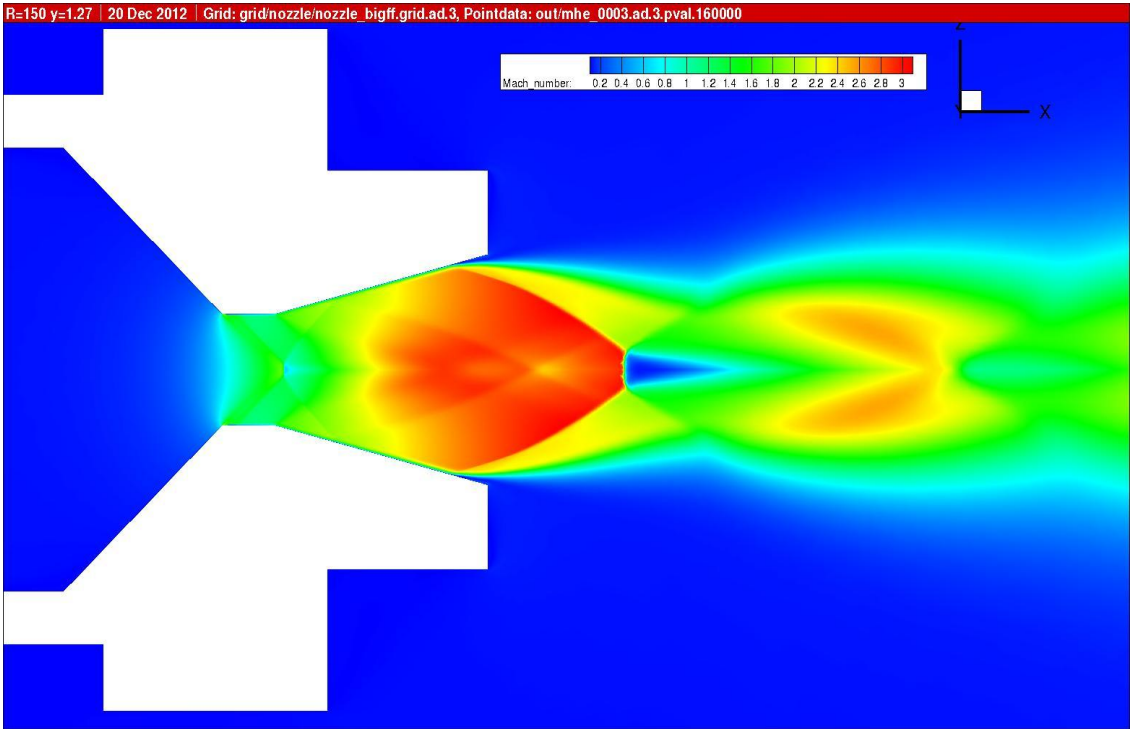
Figure 17: Tau code calculation of Mach number. R=150 J/KgK γ =1.27

Looking to these graphs with mind in a y^+ shown before, it is possible to confirm the accuracy of the model which will be definitively validated with the future experimental data comparison.

4. CFL loop efficacy and convergence of the method

The logic of the simulation with Tau Code is based on the use of five CFL loops, as described in the Chap.3 together with the definition of the *"CFL number"* parameter. The parameter "*CFL number (large grad p)"* is used in the presence of large pressure gradients (i.e. shocks) and through a bridging function the CFL number is reduced to the value defined by user near shocks, increasing the stability of the spatial scheme [7]. These parameters are the input for the simulation and a correct choice of the initial values is a good starting point to reach the convergence of the method.

The main purpose of this paragraph is to demonstrate the efficacy of five loops in combination with the adaptations that give better results than a single simulation with only one couple of values for the parameters interested.

It can be easily noticed, looking the following graphs, how the influence of the complete loops (five CFL loops + four adaptations) is useful to reach a good level of convergence of the method, expressed by the values of y^+ and residual. As already explained in the Chap.2.2, a value of y^+ equals to 1 represents an indicator of how effective is the mesh realized for the entire domain and then a convergent solution in a near-wall modeling.
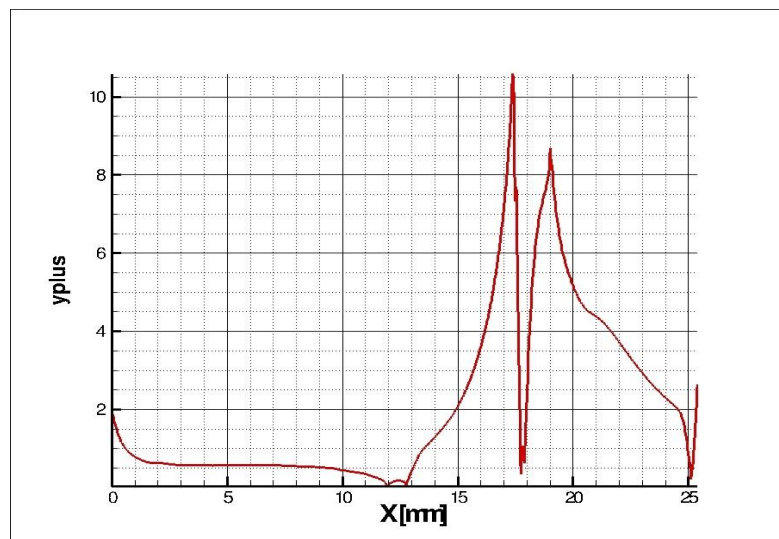
Figure 18: y^+ trend for a simulation with no adaptation and one couple of CFL values (cfl number: 0.25 ; cfl number (large grad p): 0.05)

The Fig.18 shows the y^+ trend for a simulation without adaptations and with only one couple of values for the *CFL Numbers* (CFL Number: 0.25, CFL Number (large grad p): 0.05): the parameter y^+ is far from 1 and the peaks are very extended, reaching a maximum value bigger than 10. In this case the

simulation does not provide a good results and the mesh, not having a good resolution, has not been adapted to the real field and gradients.

The same situation occurs using different values for the couple of CFL number (i.e. CFL Number: 1, CFL Number (large grad p): 0.2): looking at Fig.19, the y^+ trend is very similar to the previous example and still far from to be constant on 1.
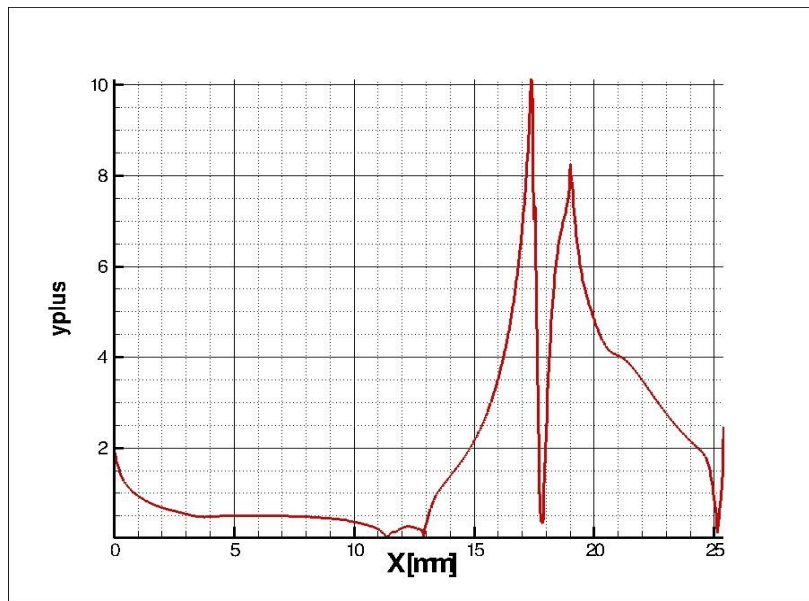
Figure 19: y^+ trend for a simulation with no adaptation and one couple of CFL values (cfl number: 1 ; cfl number (large grad p): 0.2)

Nothing changes if one loop (with no adaptation) is performed and the result for the y^+ is again quite the same (see Fig.20).
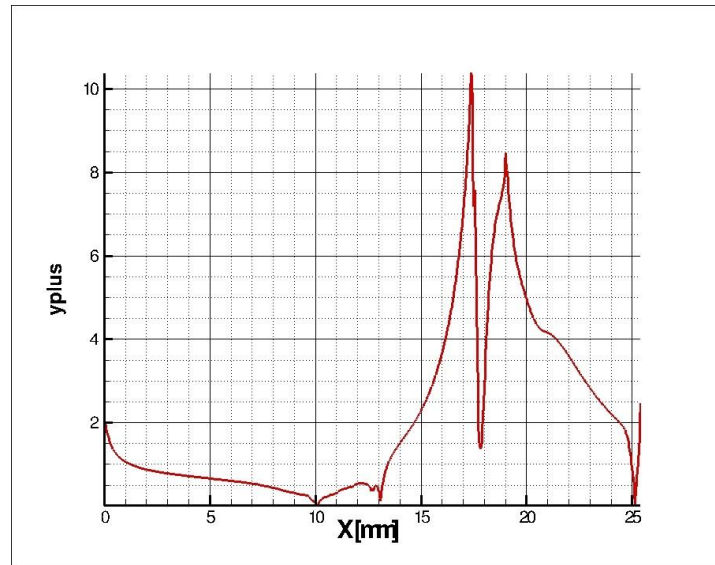
Figure 20: y$^+$ trend for a simulation with no adaptation and one loop (cfl number from 0.25 to 2 ; cfl number (large grad p) from 0.05 to 0.4)

However running the complete scheme of the simulation with five CFL loops and four adaptations, the result shows a more adequate resolution of the mesh and consequently the convergence of the method is satisfied. The demonstration is in the Fig.21 where the trend of y^+ is now very close to 1 for almost all the length of the nozzle, with the presence of the peaks in correspondence of the shocks of limited amplitude.
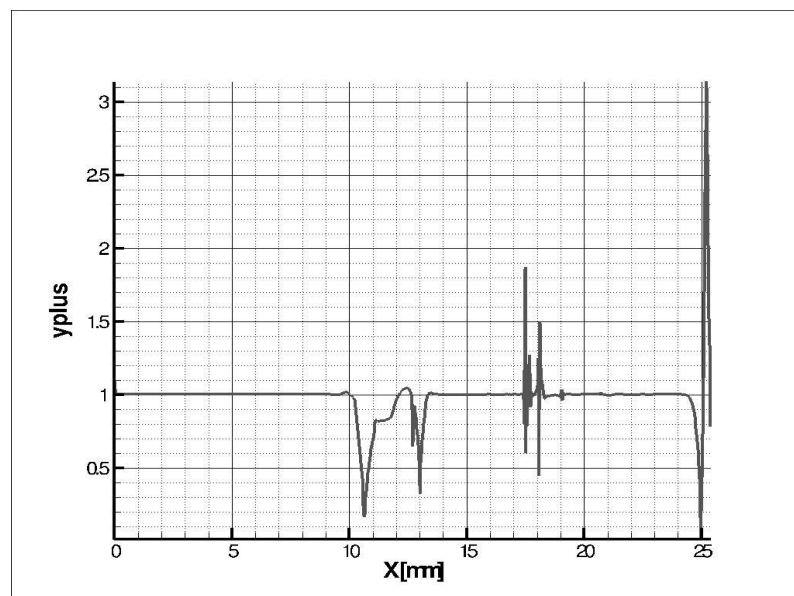
Figure 21: y$^+$ trend for a complete simulation: 5 CFL loops and 4 adaptations

The latest case corresponds at the simulation performed in Chap.11 and 12 using the definitive thermodynamics values related to the PET.

In this case to ensure the correctness of the results and to guarantee the convergence of the method, the monitoring all the interested values during the simulation is necessary. Special attention has to be dedicated at the *residual*, the difference between the values calculated from Tau code in two consecutive iterations and related to the norm of density increments [7]. Observing it, it is possible to see that the value of the residual is high at the beginning of the simulation and after each adaptation, and then it decreases very fast to a value close to zero. This behavior could be detected in the following Fig.22: only the last CFL loop after the fourth adaptation is shown here because the software provides a single file at the end of simulation with the residuals after the last adaptation.
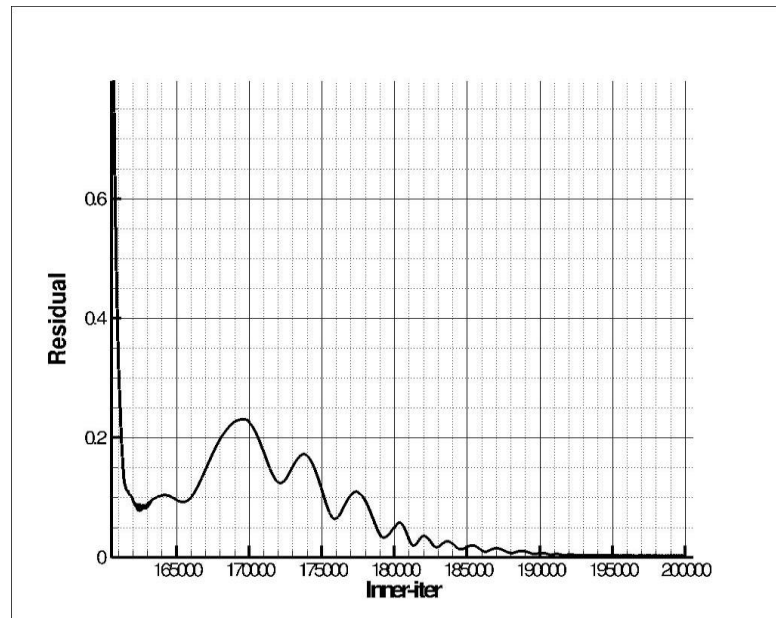
Figure 22: Residual zoom – final loop

It possible to observe how, iteration after iteration, the residual already small for the previous adaptations decreases further, reaching a value closer to zero. The oscillations visible at the end of the simulation are anyway very small and then have not influence for the convergence.

The *minimum residual* is set in the parameter file by the user at 10^{-6} and it means that the solver stops if the current residual is less than the initial residual times the prescribed number [7]. The magnitude of the *residual* reached during the simulation is 10^{-4}, a good result for this method.

The Fig.22 is a zoom of a restricted area of the plot: the complete graph is represented in Fig.23.
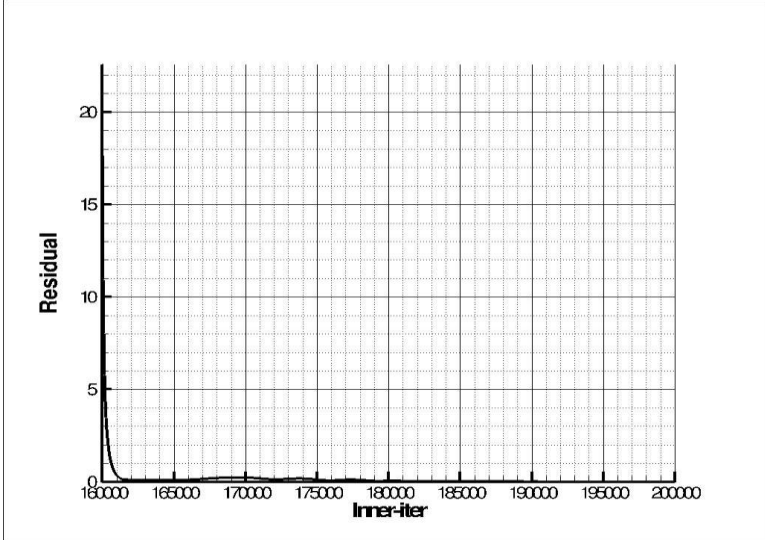
Figure 23: Residual - final loop

For knowledge is necessary to report here in Fig.24 also the graph of the max residual that is the maximum value of the residual reached for each iterations and related to the maxima of density increments.
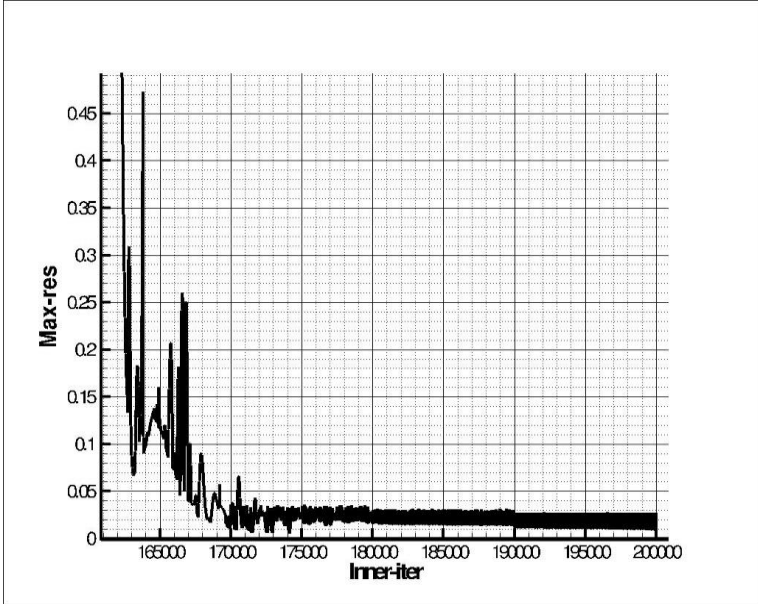
Figure 24: Max residual - final loop

However, the analysis of the residual gives only partial information for the convergence of the method. As already told the residual is just related to the norm of the density increments and looking at this parameter means only monitoring the behavior of the method in terms of convergence in time. To check then the convergence also in terms of spatial discretization, it is useful to monitor integral values involved in the simulation. In this way the method is convergent when the value under control becomes constant [12]. For these reasons also the drag coefficient C-drag is monitored during the simulation and its plot could be seen in the following graph (Fig.25): the C-drag tends to a constant value at the end of the entire simulation and, even though there are some fluctuations, these affect the fourth decimal place of the value.
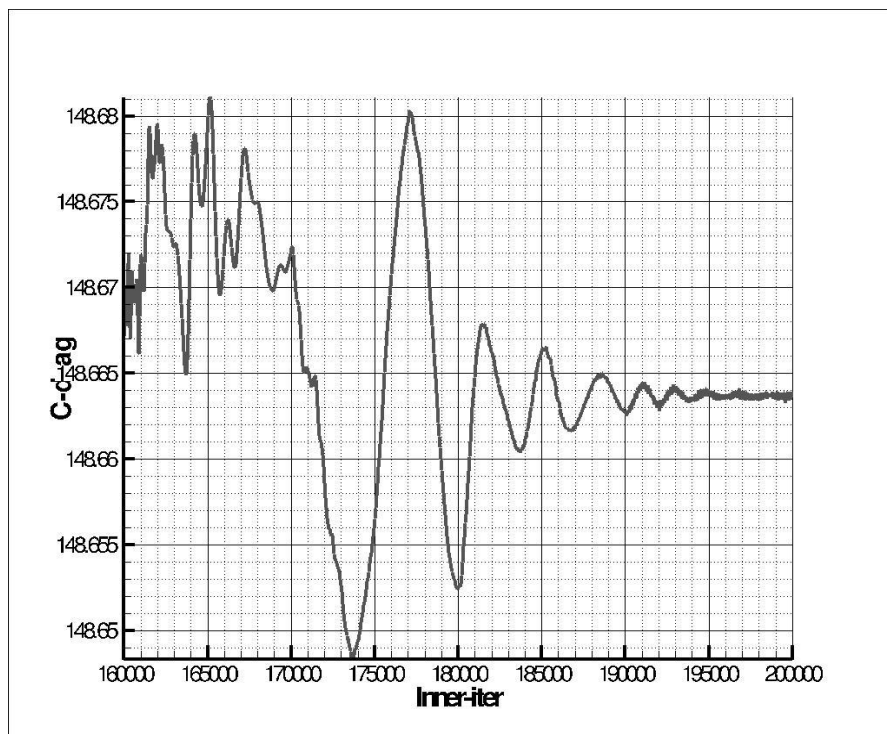
Figure 25: Convergence of the method - C-Drag coefficient

5. **Approximate NASA Cea model**

To obtain reliable thermochemical properties for the mixture flow used made of N_2O and polyethylene terephthalate (discussion on this in Chap.7), it is possible to evaluate the chemical composition of the system through NASA Cea software, developed by Gordon & McBride.

Specifying the kind of problem of interest (i.e. rocket, detonation, assigned enthalpy and pressure problem…) and setting the input data requested the software is able to return the thermodynamic, thermochemical and transport properties of complex mixtures.

The software is based on the well known equations and relations for chemistry and thermodynamics, assuming all gases as ideal and the interaction among phases negligible [10] and then the perfect gas law can be used.

The study of MHT concerns with a "rocket problem" considering a mixture made by 7 grams of Nitrous Oxide N_2O and 3 grams of polyethylene terephthalate (commonly called PET) $C_{10}H_8O_4$. However, the PET is not included in the NASA Cea library. For that reason, as first step of evaluation, the same quantity of simpler Ethylene C_2H_4 is chosen for the simulation with the following input data:

Mixture ratio o/f	2.333
Oxide	N_2O
Fuel	C_2H_4
Chamber Temperature estimated	6000 K
Chamber pressure	12 bar
Supersonic Area ratio A_e/A_t	4.25

Table 6: Input data for NASA Cea simulation

The problem is considered frozen, in agreement with what has been done in Tau Code, and the chamber temperature is 6000 K. It is a high value but is only estimation for the first step of further temperature calculation in the chamber.

NASA Cea produces the following output results:

O/F = 2.33330   %FUEL = 30.000300   R,EQ.RATIO = 4.034390   PHI,EQ.RATIO = 4.034390

	CHAMBER	THROAT	EXIT
Pinf/P	1.000	1.8337	32.232
P [BAR]	12.000	6.5442	0.37230
T [K]	1514.49	1318.29	652.72
RHO [KG/CUM]	1.8047	1.1306	0.12991
H [KJ/KG]	363.01	-13.544	-1213.15
U [KJ/KG]	-301.93	-592.34	-1499.73

G [KJ/KG]	-16578.9	-14760.7	-8514.87
S, [KJ/(KG)(K)]	11.1866	11.1866	11.1866
M, (1/n)	18.937	18.937	18.937
MW, [MOL WT]	17.190	17.190	17.190
Cp, [KJ/(KG)(K)]	1.9405	1.8969	1.6946
GAMMAs	1.2924	1.3012	1.3497
SON VEL,[M/SEC]	927.0	867.8	621.9
MACH NUMBER	0.000	1.000	2.855
PERFORMANCE PARAMETERS			
Ae/At		1.0000	4.2539
CSTAR, [M/SEC]		1223.0	1223.0
CF		0.7096	1.4517
Ivac, [M/SEC]		1534.8	1936.9
Isp, [M/SEC]		867.8	1775.5

Table 7: Approximate NASA Cea output

From these results it is possible to extrapolate the gas constant *R* and isentropic expansion factor γ necessary to the simulation with Tau code. Using the calculated values of temperature, density and isentropic factor for the combustion chamber as new input for Tau code, new results for the CFD simulation are available.
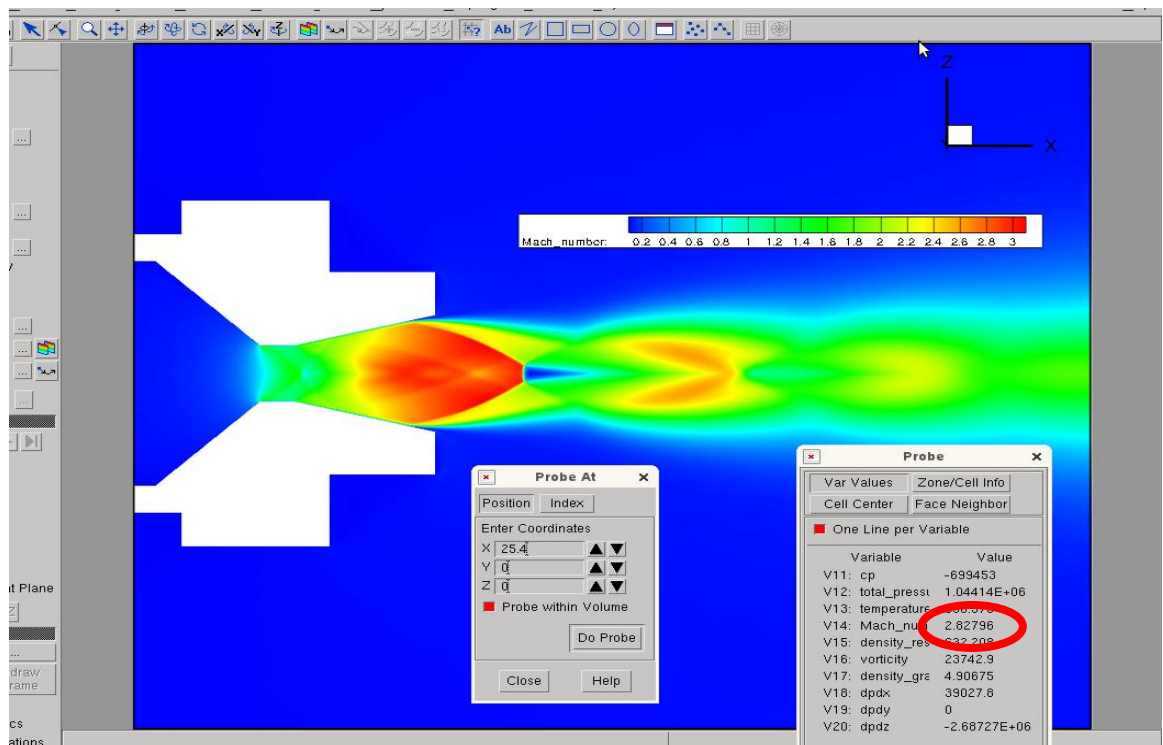
Figure 26: Tau Code Calculation of Mach number. R=439.05 J/KgK γ=1.2924

It is important to notice that the Mach number in the exit of the nozzle obtained with NASA Cea is equal to 2.855 and the Mach number computed by Tau code at the same position is 2.828. It is possible to affirm the efficiency of the two models.

This first analysis, concerned with the use of ethylene instead of polyethylene terephthtalate, is not of course definitive but as initial step it is useful to give a preliminary idea of the orders of magnitude of the variables involved. A complete and detailed analysis of the results provided by NASA Cea is presented in the Chap.10 where the effective PET properties are used.

6. Micro hybrid thruster test campaign

The CFD simulation and analysis give a first idea of how the phenomena develops and behaves in the reality. Modifications and changes are possible in case of not reasonable results to prevent waste in time and money during the experimental test phase. The experimental campaign confirms and validates what has been done with CFD studies.

In this work, a experimental test campaign is conduct with the final aim of the to obtain data sets for comparison between the numerical model presented before and the experimental tests, ensuring the reproducibility of the event.

A broad set of test serves out but the tests from 1 to 5 are used to make practice with assembling and figure out the thrust behavior. The further tests 6 and 7 are used to calibrate the instrumentation and find a reliable reference point to guarantee the reproducibility of the phenomena. Many tests are the bases for optical visualizations, discussed in the Chap.15 and 16, confirm the behave of the thruster.

Actually, the analysis is based on a wide range of tests performed during the campaign which lead to similar results, but the main calculations presented refer to this two tests, chosen as reference.

7. Components and assembling

The current version of MHT used is made of a steal case containing all the constituent elements listed below:

- convergent - divergent nozzle;
- injector system;
- diaphragm;
- piercer;
- arming device;
- metal rings;
- PET fuel package;
- N_2O oxidizer bottle
- igniter pill.

Four O-rings with different dimensions are used to reduce and avoid the gas losses after the opening of the N_2O bottle. Two snaps rings are positioned at the end and at the beginning of the case to keep every element in the correct position. An exploded view of the whole device is presented below:

Figure 27: Thruster components   Figure 28: Injection system
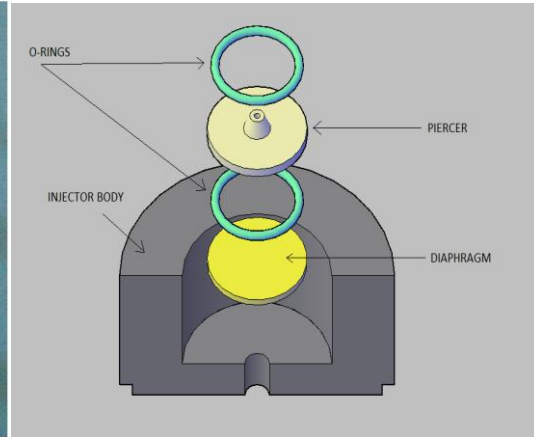
The metal rings are holed and have the task of allowing the measurements through pressure and temperature sensors. Also the case has two holes which permit to measure these physical quantities and a metal ring is positioned between the nozzle and the fuel package for this purpose.

It is necessary to give a short description of all the components to better understand how the MHT is done.

The nozzle is already discussed in the Chap.3 but it is possible to give more details: it is a convergent–divergent nozzle made of graphite and able to operate with supersonic flow. It has a throat diameter of 3.2 mm, a divergent semi-angle of 45° and a divergent semi-angle of 15° (see Fig.7).

The injection system consists of an injection body with the piercer, the diaphragm and 2 small O-rings. It is located between the oxidizer bottle and the fuel package. Screwing the arming bolt, the bottle's top is pushed against the piercer which makes a hole in it. The two O-rings are needed to avoid the oxidizer flowing backward in the thruster. Then the diaphragm is the last obstacle to the gas flow.

To start the combustion process an electric igniter pill is necessary. Using black powder, the pill allows to burn the diaphragm and ignite the fuel-oxidizer mixture.

Figure 29: Electric igniter pill

Hereafter a figure which shows the procedure for the thruster assembling. The accurate description of assembling operations is available in the documentation of the test campaign [1]:
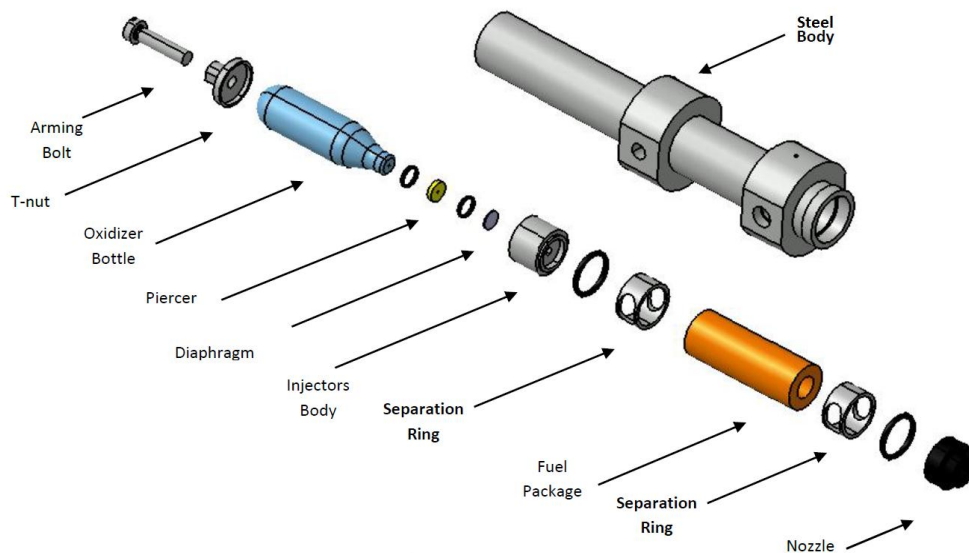
Figure 30: Exploded view of the MHT

7.1.   Properties of oxidizer N_2O

The oxidizer used is nitrous oxide N_2O also known as laughing gas or sweet air. At ambient temperature it is a colorless, non-flammable gas but, at high temperature, it is a powerful oxidizer similar to molecular oxygen.
It has the advantages that it is non-toxic and, due to its stability at standard temperature, easy to store and relatively safe to carry on a flight. Its high density and low storage pressure enable it to be highly competitive with stored high-pressure gas systems and strongly feeds the combustion.

In the Tab.8 the N_2O features are presented:

Molecular weight	44
Freezing point	-90.8°C
Boling point	-88.5°C
Critical temperature	36.4°C
Vapor density (air =1)	1.529
Relative liquid density (water=1)	1.2
Vapor pressure at 20°C	50.8 bar

Table 8: N_2O properties

It is also used as oxidizer in rocketry and in motor racing to increase the engines power. At high temperatures, nitrous oxide is a powerful oxidizer, similar to molecular oxygen and gives rise to NO (nitric oxide) on reaction with oxygen atoms and the nitric oxide NO reacts with ozone. As a result, it is the main naturally occurring regulator of stratospheric ozone and it can be readily decomposed to form breathing air. It is also a major greenhouse gas and air pollutant.

Considered over a 100-year period, it has 298 times more impact 'per unit weight' (Global warming potential) than carbon dioxide.

Several are the statements, experiments and space missions based on the N_2O oxidizer.

In a 1914 patent, American rocket pioneer Robert Goddart suggested nitrous oxide and gasoline as possible propellants for a liquid-fueled rocket. Nitrous oxide has been the oxidizer of choice in several hybrid rockets designs. The combination of nitrous oxide with hydroxyl-terminated polybutadiene fuel has been used by successful SpaceShipOne mission and others. It is also notably used in amateur and high power rocketry with various plastics as the fuel.

Nitrous oxide can also be used in a monopropellant rocket. In the presence of a heated catalyst, N_2O will decompose exothermically into nitrogen and oxygen, at a temperature of approximately 1300 °C [17]. Because of the large heat release, the catalytic action rapidly becomes secondary as thermal auto decomposition becomes dominant. In a vacuum thruster, this can provide a monopropellant specific impulse of as much as 180 s. While noticeably less than the I_{sp} available from hydrazine thrusters the decreased toxicity makes nitrous oxide an option worth to investigate.
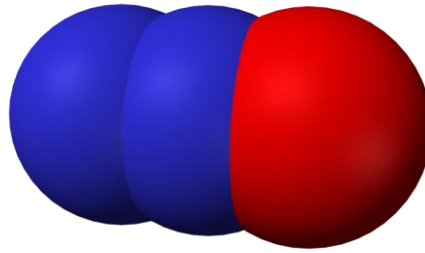
Figure 31: Representation of N_2O molecule

Nitrous oxide is said to deflagrate somewhere around 600 °C at a pressure of 21 atm. It can also easily be ignited using a combination of the two.

Specific impulse can be improved by blending a hydrocarbon fuel with the nitrous oxide inside the same storage tank, becoming a nitrous oxide fuel blend (NOFB) monopropellant. This storage mixture does not incur the danger of spontaneous ignition, since N_2O is chemically stable. When the nitrous oxide decomposes by a heated catalyst, high temperature oxygen is released and rapidly ignites the hydrocarbon fuel-blend. NOFB monopropellants has specific impulse greater than 300 seconds, while avoiding the toxicity associated with hypergolic propulsion systems. The low freezing point of NOFB eases thermal management compared to hydrazine and di-nitrogen tetroxide a valuable property for space storable propellants.

For all the reasons expressed and with the idea of using a worthy and performant oxidizer, the nitrous oxide used for the test campaign is stored liquefied in small bottles having the following characteristics:

Effective mass	Pressure	Temperature	Density
8 g	52.7 bar	293 K	667 kg/m^3

Table 9: N_2O bottle characteristics

Figure 32: N_2O bottle

7.2.   Properties of fuel polyethylene terephthalate (PET)

Ertalyte® PET P is an unreinforced, semi-crystalline thermoplastic polyester based on polyethylene terephthalate (PET-P). It is manufactured from proprietary resin grades made by Quadrant. It is characterized of having the best dimensional stability coupled with excellent wear resistance, a low coefficient of friction, high strength and resistance to moderately acidic solutions. It is especially suitable for the manufacture of precision mechanical parts which are capable of sustaining high loads and enduring wear conditions.
The continuous service temperature is 100°C and its melting point is almost 65.6°C . It retains significantly more of its original strength up to 85°C than nylon or acetal. In addition, PET offers good chemical and abrasion resistance. Its low moisture absorption enables mechanical and electrical properties to remain virtually unaffected by moisture. It can be machined to precise detail on standard metal working equipment [19].
The polyethylene terephthalate is in form of polymer chain with the basic unit repeated thousands of times, generating a product complex to study for the combustion process. In the Fig.33 it is possible to see the monomer repeated several times.
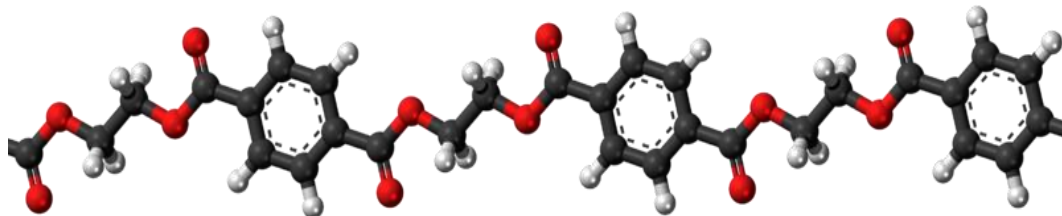
Figure 33: PET polymer chain

The choice to use PET as fuel could be find in the attitude of hybrid propulsion system to use every kind of fuel for the combustion, as described in the Chap.1. Several are the tests to characterized the performance of polymer and plastic material as fuel because they are easily product and available.
Some NASA studies had the aim to use the waste plastic products of the ISS as fuel for hybrid propulsion system. Then, the PET as fuel could be also a possibility to reduce environmental pollution using it in alternative way. That's why the properties and combustion behavior of PET is worth to be studied deeper, also because it is not so easy as seems.

In the Chap.7.3 an accurate analysis about problems and difficulties related to the PET, and in particular its heat of formation, is discussed to define the input data for numerical analysis.

The fuel used as propellant in the study of the micro hybrid thruster in this report, consists of PET in the form of hollow cylinder in which the central port is the combustion chamber (see Fig.27).

7.3.   Standard heat of formation evaluation for PET

The combustion of the PET is a complex and tricky argument to discuss. A lot of studies could be find in literature about that but, considering the requested data input for NASA Cea simulations, the most interesting problem to focus on is the heat (or enthalpy) of formation of PET, important to characterize and define the combustion properties of nitrous oxide and the selected fuel.

The standard heat of formation, also known as standard enthalpy of formation, at certain temperature is the variation of enthalpy for the formation of 1 mole of the compound from its elements, with all substances in their standard states. Its symbol is ΔH_f^0 and it gives a negative values when the process of formation of the molecule is exothermic with production of energy toward the ambient. Contrariwise ΔH_f^0 is positive for endothermic process increasing the energy of the molecule system. All the elements in their standard states have a standard heat of formation of zero, as there is no change involved in their formation.

In this paragraph several possibility to evaluate the heat of formation of the PET are discussed considering different theories.

All the reported results till this point are related to the use of ethylene as fuel for which the standard heat of formation is known. But the real fuel used in the experimental campaign is the polymer polyethylene terephthalate with a molecular structure very different from the Ethylene and whose enthalpy is now discussed.
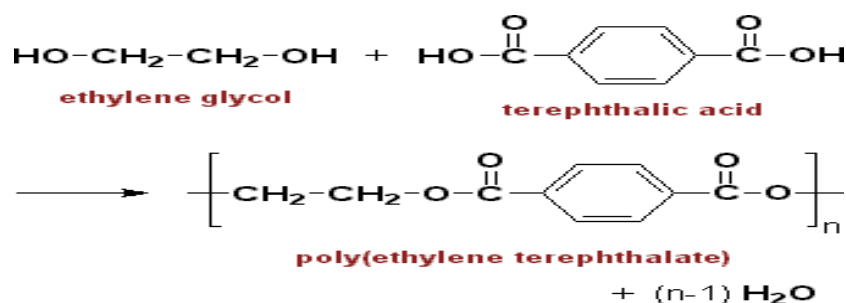
Figure 34: Chemical reaction and molecule of PET

The Fig.34 represents only the PET monomer: this recurring unit is repeated thousands of time in order to create the chain of polymer of polyethylene terephthalate.

This molecule comes from the reaction between ethylene glycol, well known in literature, and terephthalic acid, more complex, coming from a complex reaction and it is based on the aromatic ring in it.

Since PET is not included in NASA Cea library, its heat of formation should be defined. This value is not so easily found in literature. For that reason, different strategies have been adopted for the evaluation of the heat of formation of PET.

According to the *Hess Law*, it could be possible to compute the PET heat of formation from the reactants one. But as told before, while the heat of formation for ethylene glycol is known, the terephthalic acid one is difficult to obtain due to the presence of aromatic ring. Then, this solution was discarded.

Another possibility is to sum up the energy of each chemical bond forming the molecule but also in this case, the problem is the aromatic ring. It is not so clear how to evaluate the bond heat of formation forming the ring.

This procedure is the same used in [20]. In this work the PET heat of formation is equal to -333.648 KJ/mol at the temperature of 25°C but this value has to be validated.

From the bibliographic research carried out, it was possible also to find the following formula for polymers [21]:

$$\Delta H_f^{\ 0} = -9.85 X \ {Kcal}/{mol}$$

where *X* is the degree of polymerization, ratio between molecular weight of the polymer and molecular weight of the repetitive unit:

$$X = \frac{PM_{polym}}{PM_{ru}}$$

Considering:

$$PM_{ru} = 192.2 \ {g}/{mol}$$

$$PM_{polym} = 20000 \div 40000 \ {g}/{mol}$$

the degree of polymerization is (the value of 30000 g/mol is used as average for PM_{polym}):

$$X = 156.11$$

and then

$$\Delta H_f{}^0 = -1537.7 \, Kcal\!/\!_{mol} = -6433.7 \, KJ\!/\!_{mol}$$

It must be consider that this value, though completely different from the previous one, is related to standard polyethylene and not to polyethylene terephthalate.

Of course, further possibilities to evaluate the heat of formation of PET are by experimental campaign but it takes a lot of time, or using as first step of numerical simulation, compounds similar in the behavior and molecular structure to the PET (i.e. ethylene C_2H_4, acetylsalicylic acid $C_9H_8O_4$) to obtain $\Delta H_f{}^0$ with the same order of magnitude of the real one.

More realistic studies about the heat of formation of the PET are related to the Van Krevelen-Chermin theory.

This theory hereafter discussed is based on the *additivity of group properties of Van Krevelen-Chermin method*. According to this method, the molecular structure of the polymer is sufficient for the evaluation of the heat of formation that can be easily found by [3], [4]:

$$\Delta H_f^0 = \sum contribution \ of \ component \ groups + \sum structural \ correction = A + B*T$$

Next to the group contributions, also corrections must be taken into consideration, which allow for structural corrections and for the degree of symmetry of the molecule. The group contributions are considered as linear functions of the temperature and these, together with structural corrections, are based on experimental data [5].

The heats of formation of the polyethylene terephthalate constituent groups at T = 25 °C = 298 K are ([3], [5] and [6]) :

$$2*(C=O) = 2*(-132000 + 40*T) = -240160 \, J\!/\!_{mol}$$

$$2*(-O-) = 2*(-120000 + 70*T) = -198280 \, J\!/\!_{mol}$$

$$2*(-CH_2-) = 2*(-22000 + 102*T) = 16792 \, J\!/\!_{mol}$$

$$ = (96000 + 185*T) = 153640 \, J\!/\!_{mol}$$
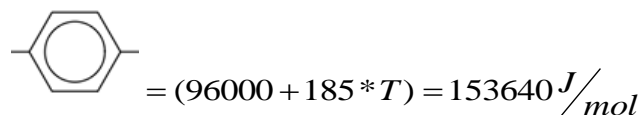
then summing these group contributions, it is possible to evaluate the heat of formation of the Pet monomer:

$$\Delta H_f^0 = -268008 \, J\!\!\Big/\!\!_{mol} = -268.008 \, kJ\!\!\Big/\!\!_{mol}$$

An important hypothesis is behind these considerations: the structural corrections and group contributions are based on experimental data and all the values are standardized for an ideal gas in its standard state [4].
This calculation is confirmed and validated by the Van Kreveler-Chermin theory and the model explained in [6]. Then for all the next calculations with NASA Cea this new value of heat of formation for PET will be used, which should be conformed to the real value of the fuel used in the experimental tests.

The work considers an experimental campaign on the MHT and compare the results with the numerical ones. This also provide a further confirmation of the goodness in the evaluation of heat of formation of PET using the Van Kevlern-Chermin theory.

8. Operation principles and configuration

Once the MHT is completely assembled, it is ready to be armed by screwing a bolt on the top of the oxidizer bottle. This allows, by pushing the bottle on the piercer, to make a little hole in it. Then the nitrous oxide is free to flow from the bottle to the combustion chamber but it is held back by the diaphragm. When the ignition system is activated the electric pill generates a spark and, thanks to the black powder surrounding it, the diaphragm is burned, the gas expands from the bottle and is able now to flow. This operation permits to have simultaneously the break of the diaphragm and the start of the combustion generating a heat source.

All the exhausts are free to flow from the combustion chamber to the nozzle producing thrust.

The first configuration adopted consists in the electric pill passing through the nozzle to reach the correct position near the diaphragm. This is the easiest way for positioning the electric pill head close to the injector body but the presence of the wires coming out from the nozzle makes difficult and disturbed the visualization of the exhaust flow, mostly when a fixed camera is used to record it.

To avoid these disturbances a new configuration is necessary which permitt to insert the electric pill not from the nozzle but using the couple of holes in the external case of the MHT and fill all the space around it between the metal ring and the injector body with black powder. Doing so, the head of the igniter is still close to the diaphragm and the wires do not interfere with the exit of the nozzle and a clearer view of the exhaust is possible. This configuration creates sometimes problems due to the fact that is not possible to control exactly the position of the electric pill that could turn or flip and, if the amount of black powder it is not enough, the diaphragm may not burn and no ignition is possible.

8.1.   Measurement chain and sensors calibration

The only required measurements are relative to the temperature and pressure in the combustion chamber and the thrust. Further evaluation of the exhaust will be realized using optic and laser system.

Sensor	Range
Temperature (Type S)	$273 \div 2040$ K
Pressure	≤ 100 bar
Thrust	$0 \div 490$ N

Table 10: Sensors characteristics

All the sensors, except the temperature ones, are wired to an amplifier box composed of several amplifiers with adjustable gain. For the case studied, a gain factor of 100 and input voltage of 10 V are set for all the channels.

All the values are recorded due to an oscilloscope which permits to visualize, analyze and store the data. For that reason four channels are necessary.

In the following picture, a drawing of the measurement chain is shown:
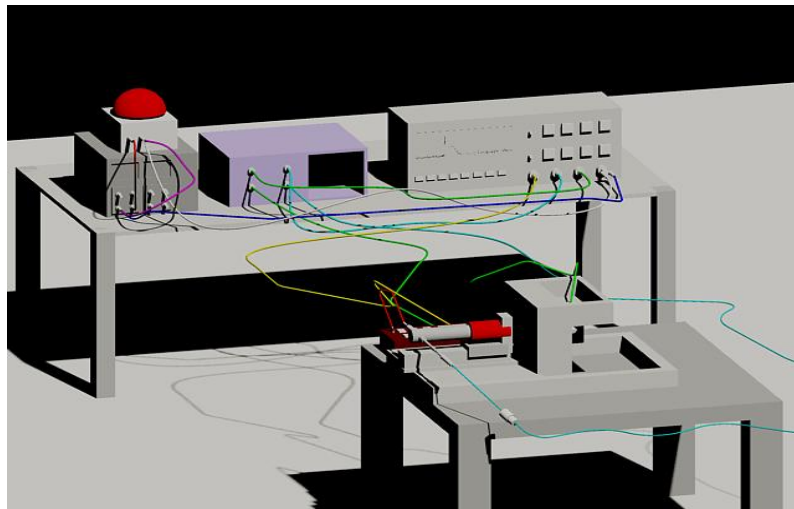
Figure 35: Measurement chain representation (courtesy of Padoan L.)

The thrust sensor, shown in Fig.36 and 37, is ALTHEN AOBU-50k and installed on the test rig.

The pressure sensor is manufactured by Honeywell and it's mechanically linked to the thruster by screws. It measures the total pressure just before the nozzle as shown in Fig.38.

Both the signals are sent by cables to the amplifier for the amplification before going to the oscilloscope.

Figure 36: Thrust sensor   Figure 37: Thrust sensor detail
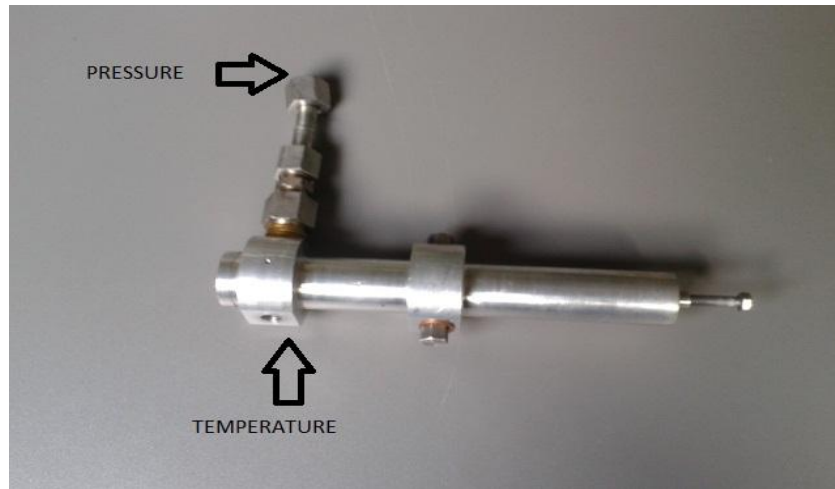
Figure 38: Pressure sensor

The temperature sensor is a thermocouple type S coupled with a thermometer which is specific for thermocouple type K. For that reason a specific calibration is needed.

This sensor is mechanically connected to the thruster by screws, linked to a thermometer which elaborates and amplifies the signal bringing it directly to the oscilloscope without passing from the amplifier.

All these sensors bring the signals to the four channels oscilloscope (mod. TEKTRONIX MSO 2024) which applies a further amplification of a factor 10 for a correct and better visualization on its display. Then, summing, the thrust and pressure signals are amplified of a total factor 1000 while the temperature and the igniter ones only of a factor 10 due to the oscilloscope.

Each channel needs to be set in a proper way according to the level of noise and amplification of the sensors. The following tables show the amplifier and oscilloscope setting channel by channel:

Channel	Measure	Input voltage	Gain
1	Thrust	10 V	100
3	Pressure	10 V	100

Table 11: Amplifier setting

Channel	Measure	Vertical scale	Physical scale*	Horizontal scale	trigger
1	Temperature	100 mV/sq	475.63 °C/sq	400 ms	X
2	Pressure	2 V/sq	17.71 bar/sq	400 ms	X
3	Thrust	500 mV/sq	17.81 N/sq	400 ms	X
4	Igniter	5 V/sq	/	400 ms	2 V

Table 12: Oscilloscope setting
*calculated with T0013

The fourth column in the Tab.12 represents the physical conversion in terms of correspondence between the measured signals and the effective physical quantities per square. This calculation must be checked with what the oscilloscope displays.

All the values measured and stored by the oscilloscope are given in *mV* and for evaluating the effectiveness of the measurement and dealing with reasonable values in the correct unit of measure, a calibration is necessary for each sensor.

Starting from the pressure sensor, its calibration curve is available from the DLR database of the instruments which provides the following expression [2]:

$$y = A0 + A1*X + A2*X^2$$

with the constants equals to:

- $A0 = 5.084175\,bar$
- $A1 = 4.858978\,bar/mV$
- $A2 = 1.33235e-03\,bar/mV^2$

In this case, using the dataset measured from the pressure sensor and provided from the oscilloscope (cut the values of all the amplifications) as variable *X*, is possible to know the correspondent value of the pressure in *bar*. It is possible to notice the coefficient *A2* is very small and then close to be negligible generating a linear calibration.

Regarding to the thrust sensor, the expression of calibration is not available from the DLR database and then different sets of measurement with different kind of loads are necessary. Considering the impossibility of measuring loads in horizontal test rig configuration, only two measures are taken to evaluate the offset of the sensor. Further measurements in vertical configuration are performed with the aim to produce calibration curve. All the configurations are

presented in the following table and the correspondent values are recorded by a voltmeter:

Rig position	Spring	Load [Kg]	Voltage measured [mV]
Horizontal	Yes	-	67
Horizontal	No	-	40.1
Vertical	Yes	-	132
Vertical	No	-	108.8
Vertical	Yes	5.274	310.8
Vertical	No	5.274	281.7
Vertical	Yes	9.105	446.2
Vertical	No	9.105	422.9

Table 13: Thrust sensor calibration

With a vertical and horizontal offsets respectively equal to 132 *mV* and 67 *mV*, the approximating calibration curve (evaluated by using Matlab) is:

$$y = P1 * X + P2 * X^2$$

with the coefficients :

- $P1 = 29.6076 \, N/mV$
- $P2 = -0.3755 \, N^2/mV$

Using the dataset measured from the thrust sensor and provided from the oscilloscope (cut the values of the offset) as variable *X*, is possible to know the correspondent value of the force in *Newton*.

The logic behind the calibration of the temperature sensor is quite the same with a small difference: an intermediate calibration is necessary to transform the values registered in *mV* from the oscilloscope to *°C* describing the phenomenon in a more understandable way.
For that reason the same phenomenon is recorded with two different setting: thermocouple type S with thermometer for type S thermocouple (correct configuration); thermocouple type S with thermometer for type K thermocouple (used configuration). It is possible in this way to find a relation between the values measured and the correct ones, that is:

$$y = D0 + D1 * X + D2 * X^2$$

with the constants equals to:

- $D0 = -74.9246$
- $D1 = 5.1129$
- $D2 = -0.0032$

After this, due to the fact that the conversion from *mV* and the values measured in $°C$ is known and characterized only by the amplification of the oscilloscope (remember the temperature sensor doesn´t pass through the amplifier) , it is finally possible to convert the *mV* data to values measured correctly in $°C$.

It is important to affirm that the calibration of the temperature sensor is not very reliable because of the rough and not accurate measuring used for it but anyway the magnitude of the values is correct. Another problem related to the temperature sensors is important: it is not possible to push the thermal element completely into the flow due to constructive limit of it. This influences the values measured that are probably lower than the real ones.

For each channel and sensor, is important to remember the level of amplification due to the amplifier and oscilloscope gain for the calibration computation and, also, the measurement unit reported in the datasheet saved from the oscilloscope.

9. Reference point - Test 006 & Test 007

Many tests are performed on MHT. Most of them with the only aim of make practice with the assembling, the test rig, the instrumentations and the process of combustion. However, two of these tests are used as reference tests and for the calibration of the sensors. These are the test 6 and 7 (T006 & T007) which present the following graphs for pressure, thrust and temperature:
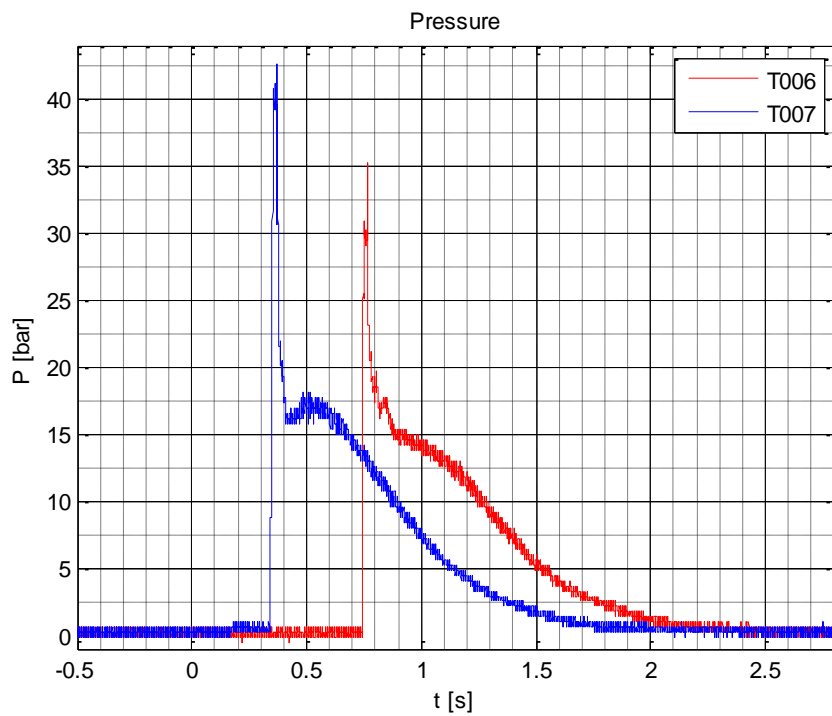
Figure 39: Pressure trend
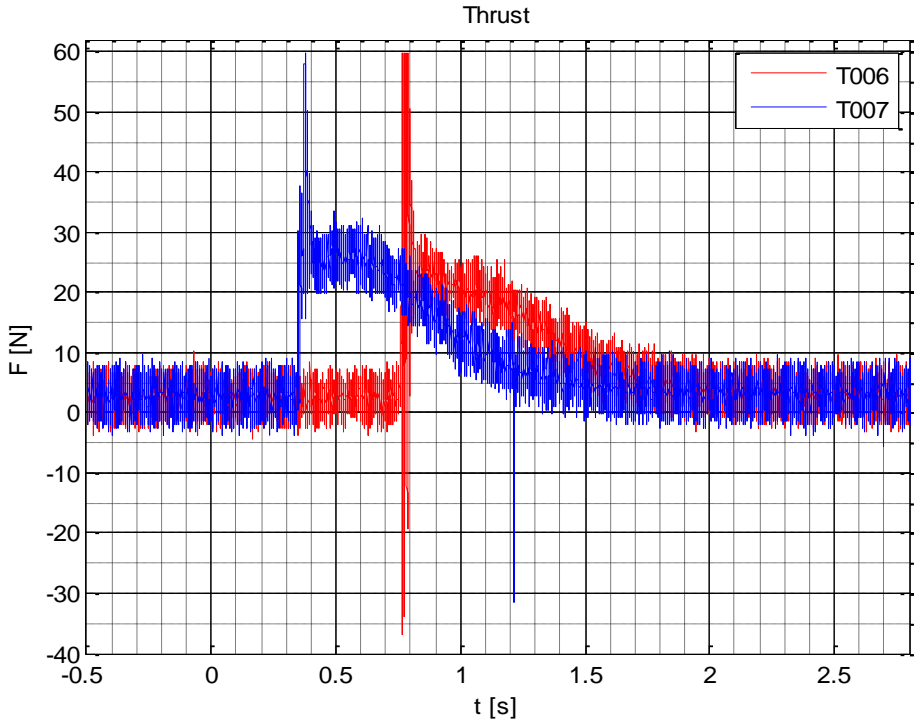
Figure 40: Thrust trend
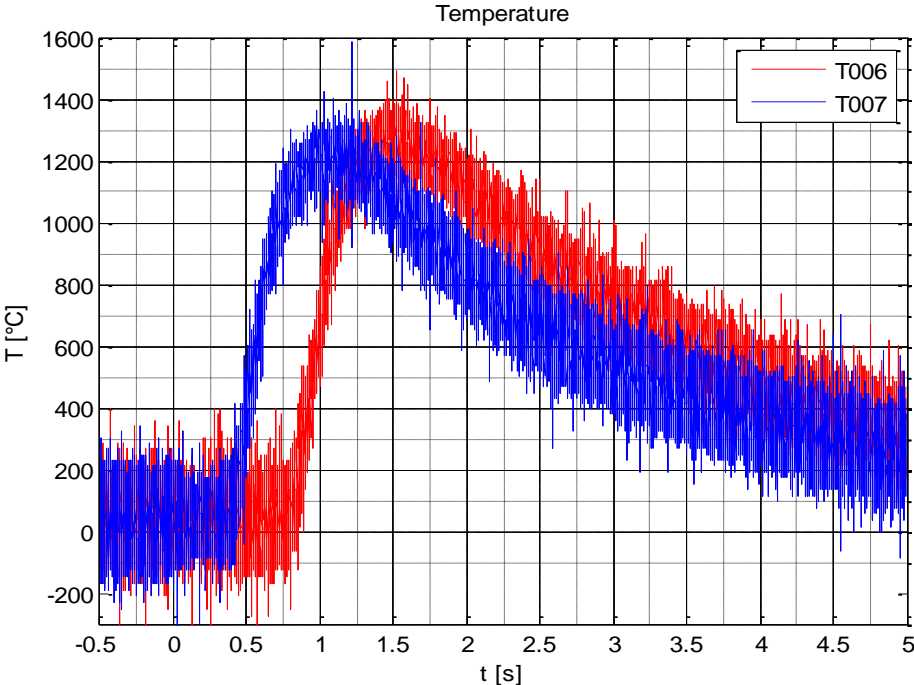
Figure 41: Temperature trend

It is possible to notice delay of about 0.5 *s* in the startup of the test T006 due to the fact that this test showed an effective delay between the moment the igniter makes spark and the start of combustion. This phenomenon will be investigate further but it is possible to make some assumptions: the N_2O bottle is not completely open at the moment of the ignition and the solicitation due to the spark completes the opening; the electric igniter pill is not so close to the diaphragm and unable to burn it immediately; the black powder surrounding the electric pill is not enough to produce a spark able to burn the diaphragm immediately.

It is necessary to evaluate and find on these curves one point, defined as *reference point*, which permit to consider certain values of temperature, thrust and pressure for the theoretical and numerical analysis. The reference point, when it fits among all the tests providing the quite similar values of pressure temperature and thrust, can be considered as evidence for the reproducibility of the event studied. This point is used also as comparison point for the numerical simulation with NASA Cea and Tau-Code.
A good reference point is chosen with the following values:

Test	Time [s]	Temperature [°C]	Temperature Peak [°C]	Temperature Peak - mean value [°C]	Pressure [bar]	Thrust [N]
T006	0.86	211.42	1488.9	1248.7	16.56	23.73
T007	0.45	211.71	1426.9	1193.2	16.57	23.74
<u>Ref Point</u>	-	211.5	1457.9	1220.95	16.6	23.73

Table 14: Reference point

The column "*Temperature peak*" in the Table 14 above is related to the peak recorded from the sensor during the experiments. Looking at the Fig.41, it is possible to see a high peak of 1584 °C for the test T007 at around 1.25 seconds. It is just a single value over the mean values of the plateau and for this reason it is discarded and not considered as the peak. The column "*Temperature peak- mean value*" instead refers to the maximum value of the approximating curve which describes the trend of the noisy signal recorded by the thermocouple. These approximating curves could be seen in the following plot Fig.42.
The values of the *reference point* are the average of those selected from the two tests.
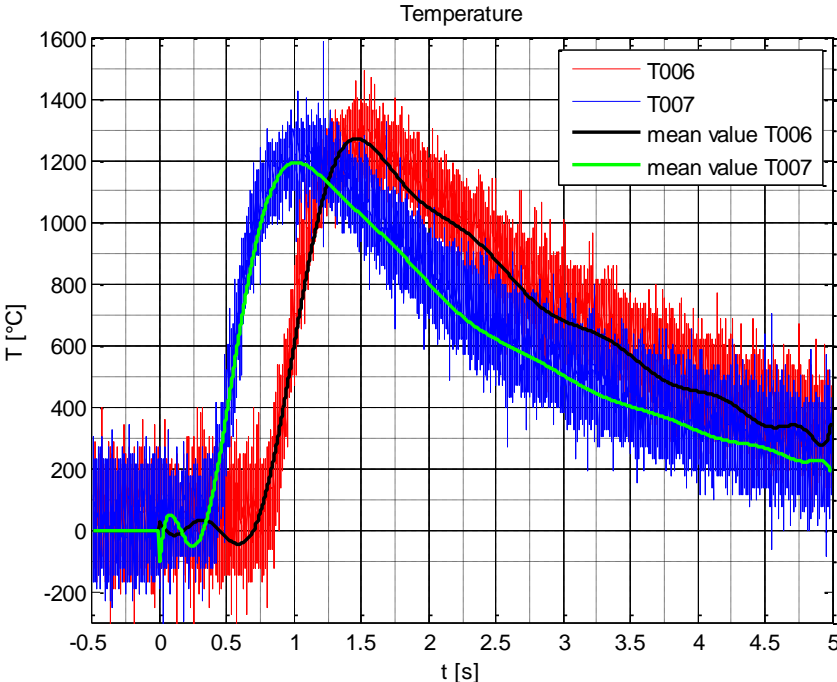
Figure 42: Temperature mean curves

10. Definitive NASA Cea model

After and before the tests 6 & 7, all the oxidizer bottles are weighted with the following results:

N$_2$O bottle	
Full	Empty
28 g	20 g

Table 15: Oxidizer weight and consumption

Regarding to the fuel package mass and its consumption during the combustion, several measurements are made during previous analysis by Padoan L. and the following values are recorded before and after the experiments:

PET packages			
Package Id	**Before comb.**	**After comb.**	**Δ mass**
b001	15.701 g	14.549 g	1.152 g
b002	15.651 g	14.590 g	1.061 g
b004	15.691 g	14.6054 g	1.0856 g
b005	15.7867 g	14.6554 g	1.1313 g
b012	15.6767 g	14.4554 g	1.2213 g
Average	**15.7013 g**	**14.5710 g**	**1.1303 g**

Table 16: Fuel packages weight and consumption

Then, a new value for the mixture ratio can be computed considering only the amount of propellant burned during the combustion process. This, together with the pressure related to the measured reference point, is used as new input data for further NASA Cea simulations.

As the amount of N$_2$O burned is only 8 g and the PET average one is 1.1303 g, the mixture ratio o/f is:

$$o/f = \frac{8}{1.1303} = 7.0778$$

The new measurements obtained by sensors, the correct mixture ratio and the same consideration about the use of NASA Cea software made in Chap.5, are used for this new simulation.

Moreover, the evaluation of the enthalpy of formation for the PET discussed in the Chap.7.3, leads to a new calculation with NASA Cea able to simulate the combustion in the chamber closer to the real one, using polyethylene terephthalate and not ethylene as fuel.

Due to the fact that the PET is not included in the NASA Cea library, a definition of this reactant is need by user-provided name and properties. It means that the name, amount, chemical formula and heat of formation have to enter by the user [10].

The following data input are in relationship with the reference point set before:

Mixture ratio o/f	7.0778
Oxide	N_2O
Fuel	$C_{10}H_8O_4$
Heat of formation PET	-268.008 kJ/mol
Chamber Temperature estimated	6000 K
Chamber pressure	16.6 bar
Supersonic Area ratio A_e/A_t	4.2539

Table 17: Input data for new NASA Cea simulation

Also in this case the problem is considered frozen in agreement with what has been done in Tau code. Some parameters, such as the geometry and estimated chamber temperature, are of course not changed from the previous simulation.

The complete output file produced by NASA Cea is reported entirely in the Appendix C . Here only the significant values are shown:

O/F = 7.07780   %FUEL = 12.379608   R,EQ.RATIO = 0.687620   PHI,EQ.RATIO = 0.647186

	CHAMBER	THROAT	EXIT
Pinf/P	1.000	1.7980	27.930
P [BAR]	16.600	9.2325	0.59434
T [K]	2528.58	2256.01	1295.79
RHO [KG/CUM]	2.4203	1.5088	0.16910
H [KJ/KG]	-172.65	-552.96	-1845.75
U [KJ/KG]	-858.51	-1164.89	-2197.22
G [KJ/KG]	-21813.5	-19861.0	-12935.7
S, [KJ/(KG)(K)]	8.5585	8.5585	8.5585
M, (1/n)	30.654	30.654	30.654
Cp, [KJ/(KG)(K)]	1.4026	1.3874	1.2892
GAMMAs	1.2397	1.2430	1.2665

SON VEL,[M/SEC]	922.1	872.1	667.2
MACH NUMBER	0.000	1.000	2.742
PERFORMANCE PARAMETERS			
Ae/At		1.0000	4.2539
CSTAR, [M/SEC]		1261.5	1261.5
CF		0.6913	1.4500
Ivac, [M/SEC]		1573.8	2021.4
Isp, [M/SEC]		872.1	1829.3

Table 18: Definitive NASA Cea output

It is important to observe the value of Mach number at the exit of the nozzle, useful to make a comparison with the results provided by Tau code and presented in the next chapter.

From these results it is possible to calculate the gas constant *R* and isentropic expansion factor γ equals to:

$$R = \frac{P}{\rho T} = \frac{16.6 * 10^5}{2.4203 * 2528.58} = 271.245 \, {J}\!/\!{KgK}$$

$$\gamma = 1.2397$$

Using the values of temperature, density and isentropic factor from the given output values in the combustion chamber as new input for Tau code, definitive results for the CFD simulation could be performed (see Chap.11).

It is possible to notice that the temperature value in the combustion chamber results from NASA Cea is much higher than the one measured during the experiment by the sensors. A possible reason for that could be the not correct position of the thermal element into the flow and the rough measurement and calibration, as explained before (Chap.8.1). The discrepancy is due also to radiative problems related to the temperature sensors into the combustion chamber which lead a loss of temperature of about 500 °C.

Nevertheless, the comparison between the mathematical model and the experimental data may disagree due to the fact the hybrid combustion could generate particles and unburnt products not able to be reproduced in the mathematical model (especially with Tau code).

Further simulation with the new data will be performed by using Tau code.

11. Definitive Tau Code model

A more precise and close to the real phenomena simulation can be performed providing a set of results more reliable and realistic using data provided from the experiment and computed by NASA Cea. Adopting the same logic of the simulation consisting of five CFL loops and four adaptations, the percentage of points and elements which could be added or removed in each adaptation has changed from 50% to 30%. With this last modification, a reduction in the computational time is obtained but with the same accuracy in the results. The adaptations affected area of the mesh and the whole geometry do not change.
At the end of the simulation, the mesh is modified from the initial grid to the refined one as follows:

	Prism	Hexa	Points
Adaptation 1	49489	16188	83734
Adaptation 2	79591	18612	119016
Adaptation 3	127861	20244	170910

Table 19: Refined grid after 3 adaptations

and in the Fig.43 it is possible to observe the adapted mesh in the nozzle and the outside area.
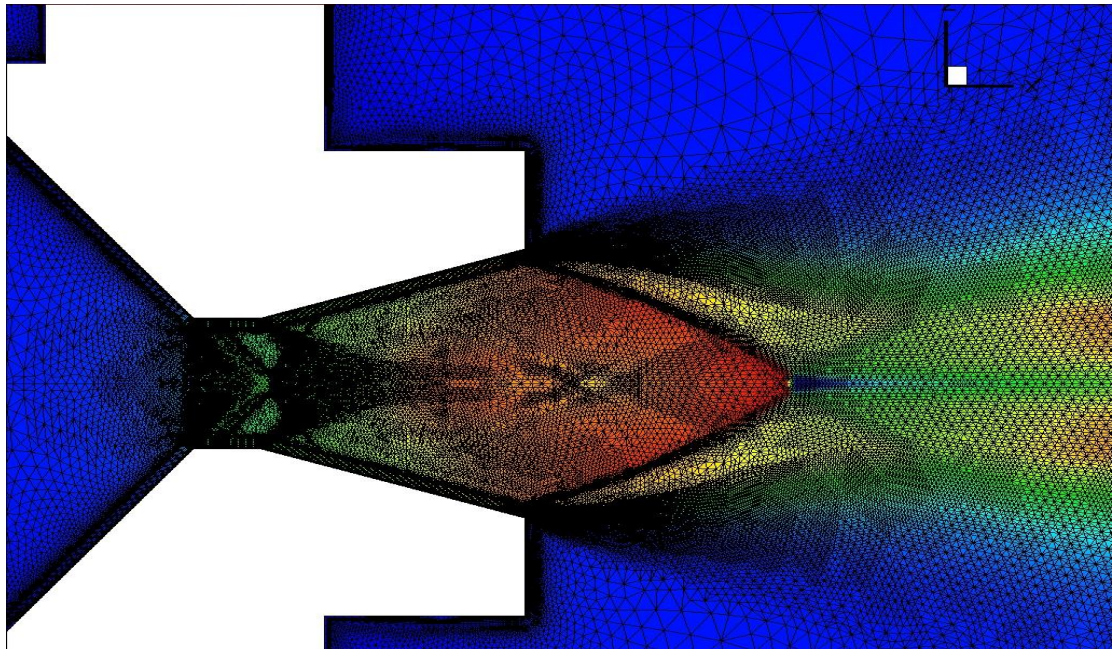
Figure 43: Adapted mesh in the nozzle and outside area

However, new thermodynamic flow values are set for this simulation, using data from experimental and NASA Cea results:

Chamber Temperature	2528.58 K
Chamber pressure	$16.6*10^5$ Pa
Reference Temperature	300 K
Reference Pressure	101325 Pa
Chamber density	2.4203 kg/m^3
Gas constant R	271.245 J/kgK
Isentropic factor γ	1.2397

Table 20: Thermodynamic values for PET simulation

All the assumptions and hypothesis expressed in Chap.3 still remain valid.
This new simulation provides the following results:
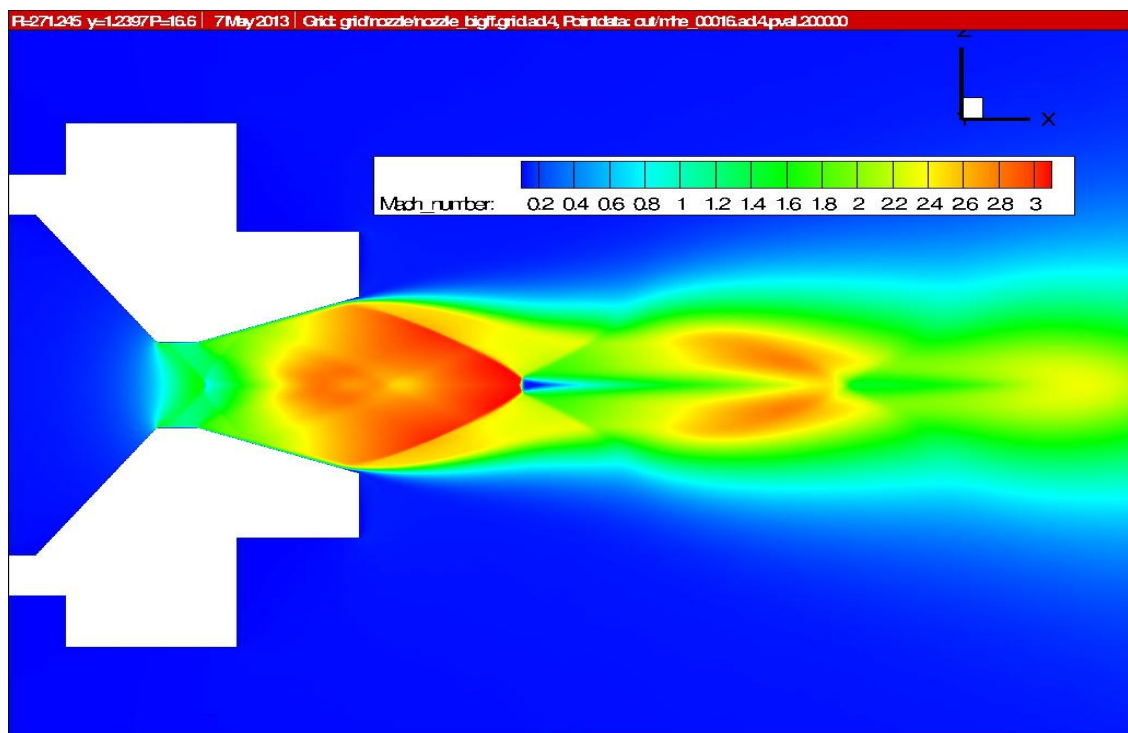
Figure 44: CFD simulation - Mach distribution - R= 271.245 J/kgK γ=1.2397
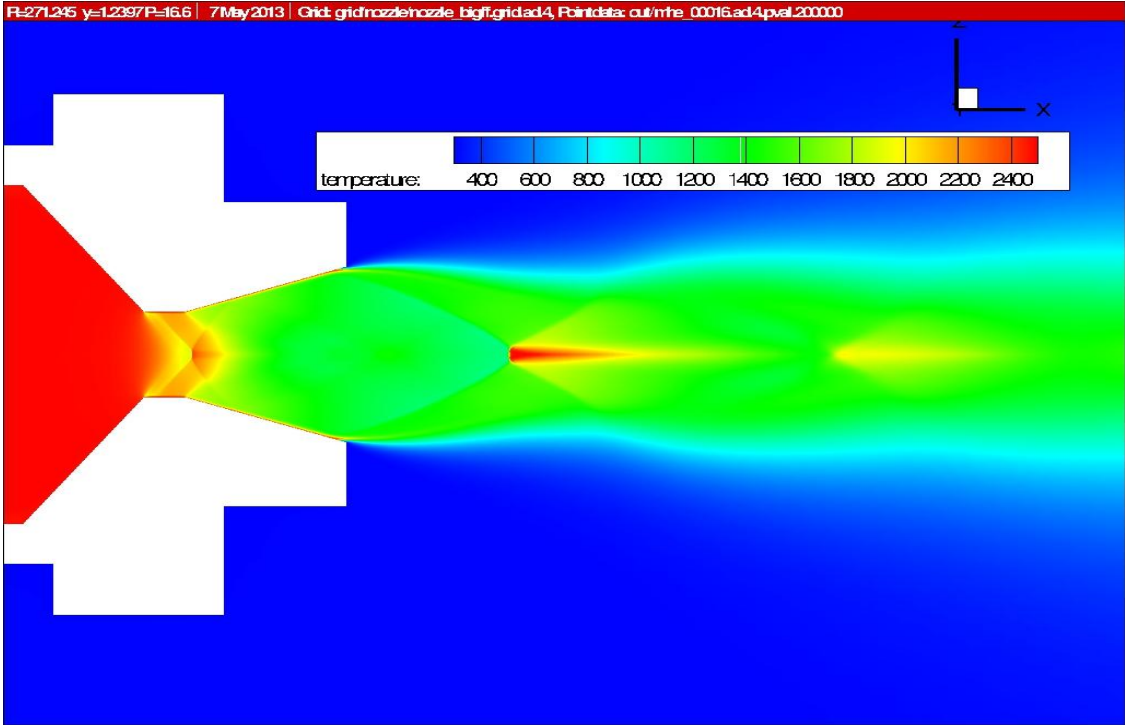
Figure 45: CFD simulation - Temperature distribution - R=271.245 J/kgK γ=1.2397
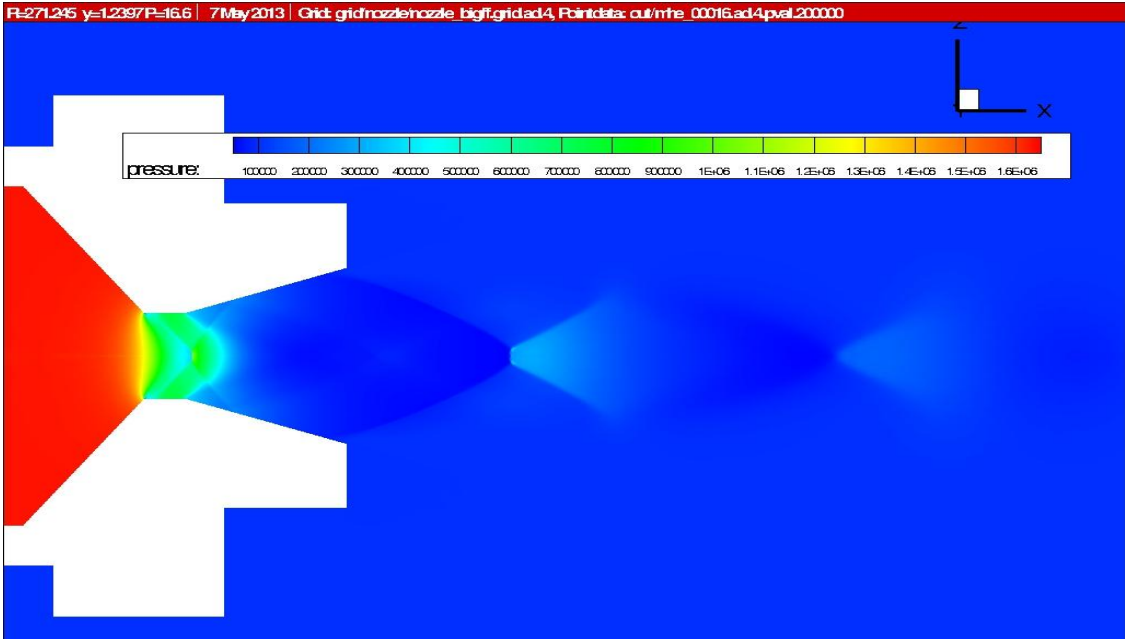
Figure 46: CFD simulation - Pressure distribution - R=271.245 J/kgK γ=1.2397

The trend of y^+ is very close to the values of 1, which is the confirmation of a good mesh resolution and a convergent solution in a near-wall modeling:
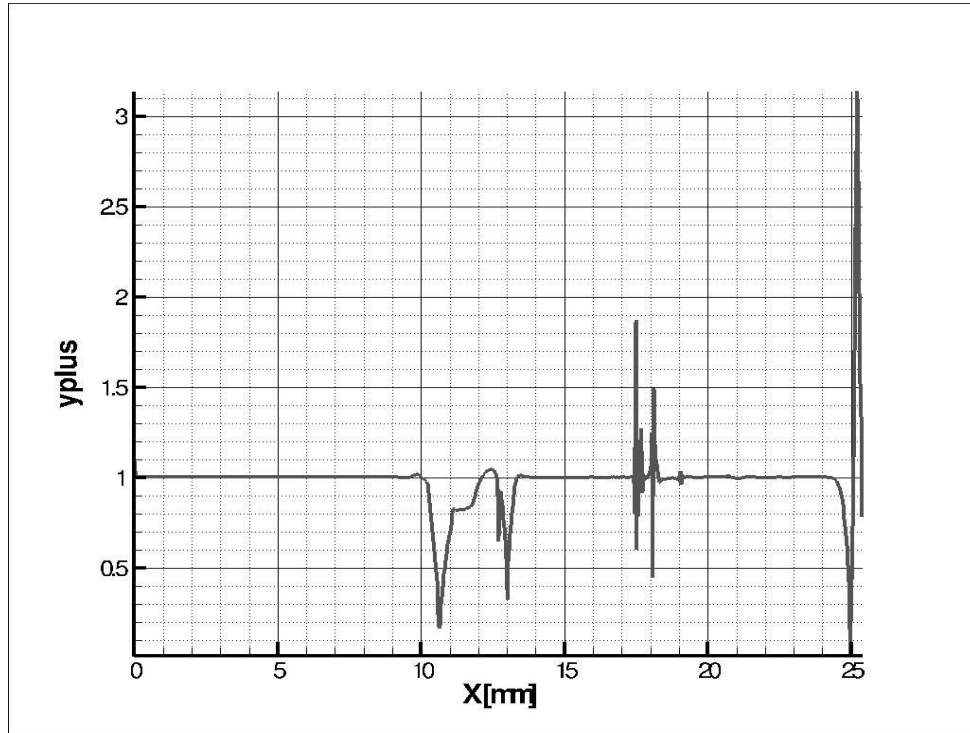
Figure 47: y+ trend in the nozzle - R=271.245 J/kgK γ=1.2397

Making a comparison between the two numerical models computed with Tau code and NASA Cea, it is possible to notice a good accordance in the Mach number values . With referring to the Fig.48 the Tau code provides a value of 2.716 at the exit of the nozzle while the previous analysis with NASA Cea gives a Mach number of 2.742 in the same postion. These two values are close together with an error of just less than 1%. This gives the possibility to affirm and confirm again the efficiency of the two models.
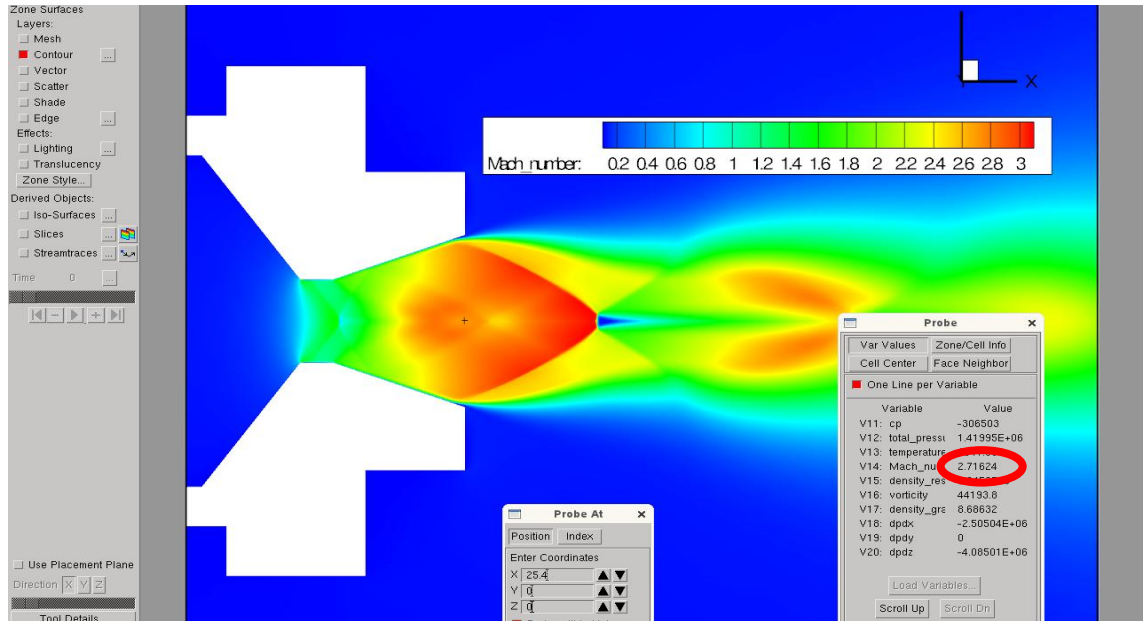
Figure 48: Tau Code Calculation of Mach number. R=271.245 J/kgK γ=1.2397

Further analysis gives the possibility to understand better the behavior of the system. In particular it is possible to focus the attention on the distribution of the Mach number along the symmetry axis of the nozzle (coordinate Z=0 mm) only for short part of the field behind the nozzle (approximately a distance of 55mm from the exit) because the whole field is not of interest and the Mach goes to zero when the flow is extinguished.
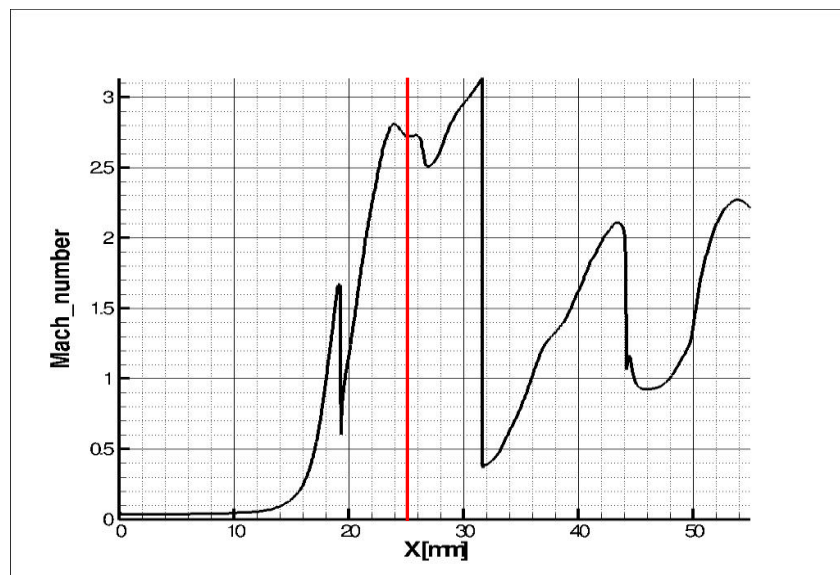
Figure 49: Mach distribution along x-axis. R=271.245 J/kgK γ=1.2397

It is necessary to remember that the length of the nozzle is 25.4 mm to notice another important feature looking to the Mach trend Fig.49, in which the nozzle exit is represented by the red vertical line. Between 18 mm and 20 mm, then inside the throat, the Mach number passes from a supersonic condition to a subsonic one and then returns at value higher than 1. This behavior leads to a loss in the nozzle performance, not able to generate the highest possible exit velocity and then it turns into limitation in the thrust. This is due to the shape of the nozzle: looking at the technical draw in Fig.7, it easy to see that the walls of the throat are parallel. This is not a perfect geometry to reach the optimal performance for the nozzle, which should have the throat walls with an angle that follows the divergent part of the structure of the nozzle itself. In that way the separation and recirculation of the flow near the sharp edges could be prevented and the throat is able to accelerate the flow as much as possible. Then a possible step forward could be a modification in the geometry of the nozzle in this sense, and investigate the results in this new configuration.

Hereafter the distribution of the velocity in x-direction along the exit section of the nozzle:
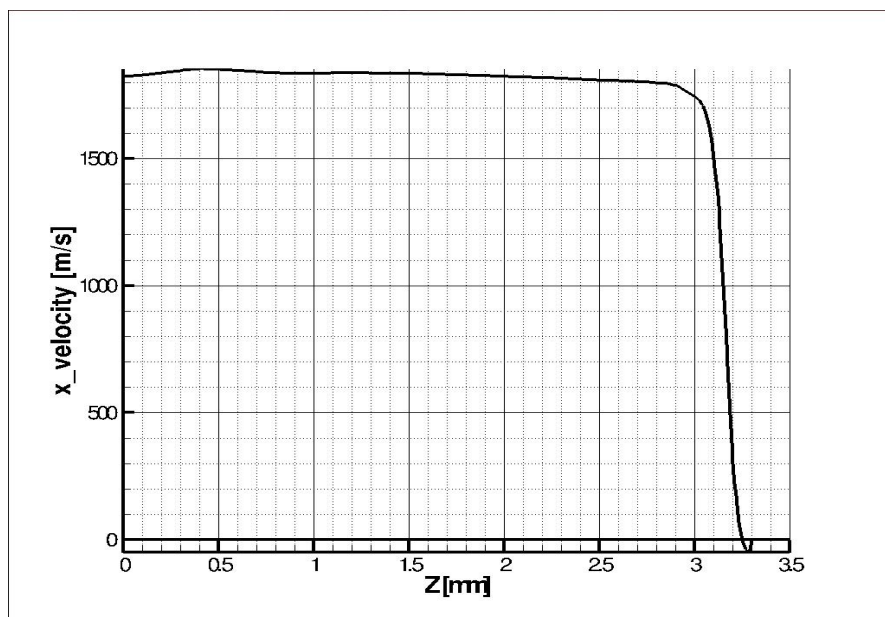
Figure 50: x-velocity in the exit section of the nozzle. R=271.245 J/kgK ϒ=1.2397

Of course the maximum of x-velocity is in correspondence of the center line at Z=0 mm (nozzle axis) while it turns rapidly to zero along the surface of the nozzle. There is also a small area in which the velocity is negative and this is due to the fact that there is a separation of the flow inside the nozzle and then it is overexpanded generating recirculation of the flow.

The Fig.51 shows the Mach trend along the Z-coordinate but at a distance from the exit of the nozzle of 34.6 mm (total distance from the center axis X=60 mm).
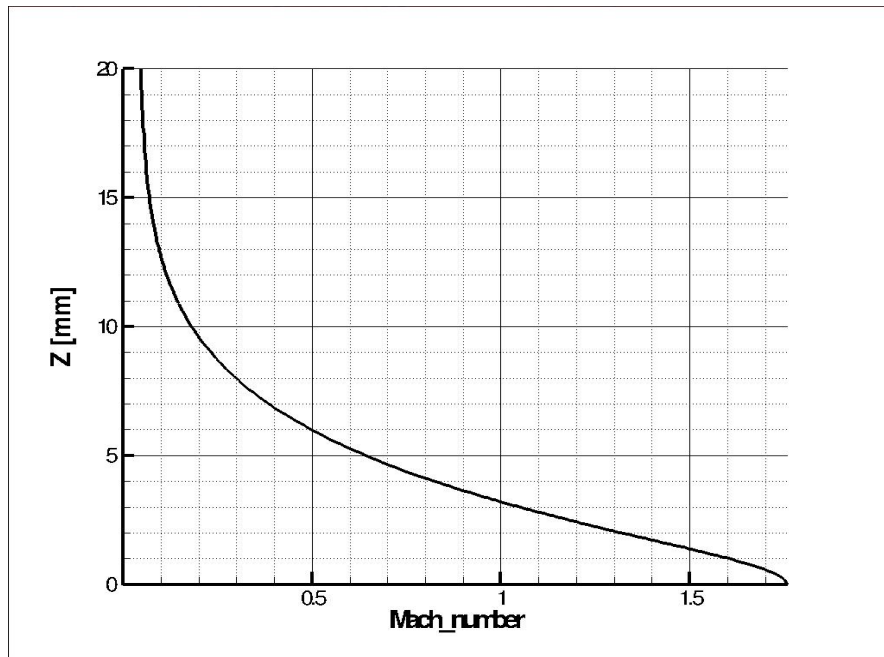
Figure 51: Mach number in z direction at x=60 mm

The point in which the Mach number turns from subsonic to supersonic is at a distance of 3.1945 mm from the symmetry axis, just close to the border of the jet (Fig.52).
It is easy to understand that the Mach number tends to zero far from the nozzle and outside the jet in which there are stationary condition with *V=0 m/s* and, for this specific case at X=60mm, it reaches a maximum at the symmetry axis of the nozzle (Z=0) where the velocity is high (refers to Fig.51). Of course, the maximum of Mach number is not always along the symmetry axis as could be seen in Fig.44 but it depends of the x coordinate chosen (i.e. across the Mach disk).
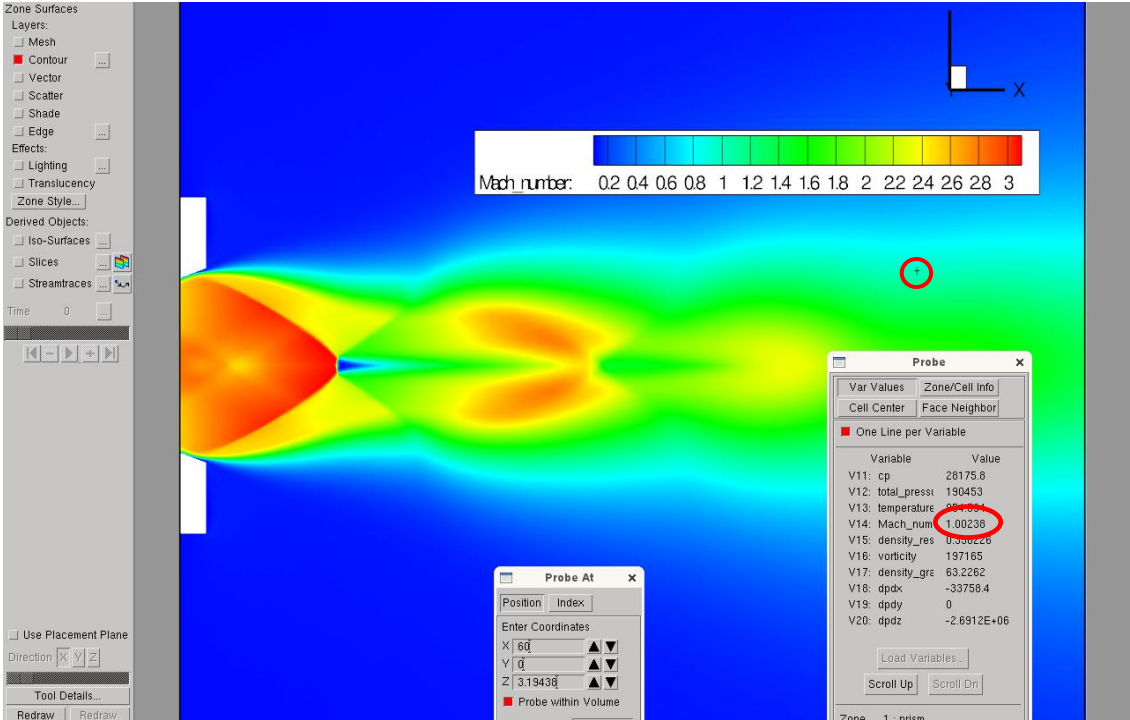
Figure 52: Transition point from subsonic to supersonic flow at x=60 mm

12. Thrust evaluation

NASA Cea and Tau code do not implement directly the value of the thrust generated by the MHT in the specified conditions. However it is easy to compute it starting both from the results provided by NASA Cea and Tau Code and making a comparison between these and the experimental ones.
The well known thrust equations is:

$$T = I_s \dot{m} + (P_e - P_\infty) A_e$$

where I_s is given by NASA Cea in *m/s,* then it is a velocity of the flow at the exit of the nozzle V_e . Of course the real specific impulse is I_s/g , with *g* gravitational acceleration. The static term of the thrust considers the difference between the nozzle exit and the environmental pressure (the same defined for Tau code) multiplied for the exit area of the nozzle. As first step the NASA Cea results are analyzed and the input values for this calculation are in the Chap.10.
The only value needs to be calculated is the mass flow rate according to this relation where the data from the NASA Cea output sheet are already substituted:

$$\dot{m}_e = \rho_e u_e A_e = 1.6910 * 10^{-1} \, Kg\!\!\Big/\!\!_{m^3} * 1829.98 \, m\!\!\Big/\!\!_s * 3.422 * 10^{-5} m^2 =$$
$$= 0.010589 \, Kg\!\!\Big/\!\!_s = 10.589 \, g\!\!\Big/\!\!_s$$

where *e* indicates for nozzle exit where all the variables are evaluated.
Another possible method to evaluate the mass flow rate is using the *characteristic exhaust velocity C** given by NASA Cea:

$$\dot{m} = \frac{P_c A_t}{C^*} = 0.010574 \, Kg\!\!\Big/\!\!_s = 10.574 \, g\!\!\Big/\!\!_s$$

Of course the two different expressions give the same result for the mass flow rate.
Then, it is possible to compute the thrust resulting from the NASA Cea evaluation:

$$T_{Cea} = I_s \dot{m} + (P_e - P_\infty) A_e = 1829.98 \Big[m\!\!\Big/\!\!_s \Big] * 0.010589 \Big[Kg\!\!\Big/\!\!_s \Big] +$$
$$+ \left(0.59434 * 10^5 [Pa] - 101325 [Pa] \right) * 3.422 * 10^{-5} = 17.94 N$$

The same calculation is presented using the Tau code solutions that lead to the following results:

$$\dot{m}_{e\tau} = \rho_{e\tau} u_{e\tau} A_{e\tau} = 0.14733 \, \frac{Kg}{m^3} * 1824.45 \, \frac{m}{s} * 3.422 * 10^{-5} \, m^2 =$$

$$= 0.009198 \, \frac{Kg}{s} = 9.198 \, \frac{g}{s}$$

with an error of about 13% from the NASA Cea value. It is also possible to notice that the two velocities u_e are very close together with only 5.5 m/s of difference.

Easily the specific impulse is:

$$I_{s\tau} = \frac{u_{e\tau}}{g_0} = 185.97s$$

(the specific impulse by NASA Cea is equals to 186.542 *s*, then the values are very similar).

Finally, the thrust calculation with Tau code gives this value:

$$T_\tau = I_{\tau s} \dot{m}_{e\tau} + (P_{e\tau} - P_\infty) A_e = 1824.45 \left[\frac{m}{s} \right] * 0.009198 \left[\frac{Kg}{s} \right] +$$

$$+ (53618.4 [Pa] - 101325 [Pa]) * 3.422 * 10^{-5} = 15.15N$$

The thrust defined by the reference point chosen in the Chap.9 is not so in accordance with the theoretical one, both Tau and NASA Cea model also if the correct fuel PET and its heat of formation are used for the simulation. Another reason for this discrepancy could be the hypothesis of *frozen condition* in NASA Cea simulation, while the combustion in the real phenomena is in *equilibrium*. Anyway it has to keep in mind that the environmental conditions (reference temperature and pressure) during the experimental test are variable and different from numerical hypothesis.

The deviation between NASA Cea and Tau code results has to be also investigated deeper but in first analysis it is possible to say that is due to very important approximation made by Gordon-McBride software: all the transformation during the simulation is considered to be isentropic.

Moreover, the thrust evaluated with experimental data is higher than the numerical computed ones and the reason should be investigate but an hypothesis is related to the fact that Tau code does not consider the combustion process. Probably it is also necessary to find a better reference point, chosen when the temperature is more or less stable along the process.

Here the different values obtained with different methods:

$$T_\tau = 15.15N$$

$$T_{Cea} = 17.94N$$

$$T_{ref\_po\text{int}} = 23.73N$$

13. NASA Cea model: imposed temperature

Because of the use of the sensors in the test campaign detect precise values of temperature, pressure and thrust, these could be used for the numerical simulations. The previous calculations with NASA Cea involve the use of some of these measured quantities as the pressure in the combustion chamber. Regarding to the combustion chamber temperature, the software provides an estimation of it starting from a value of 6000 K as first step of calculation. The computational result gives a chamber temperature of 2528.58 K for the simulation using the PET as fuel (see Chap.10).

This temperature is however divergent from the one measured with the sensors and considered as properties of the reference point but the reasons of the difference are already discussed in the Chap.10 and 11.

Then a new simulation is presented which considers exactly the sensors measured values as input for the calculation and in particular the combustion chamber temperature is set as 1458 K, while all the others inputs remain the same. This simulation is only to understand the behavior of the thermodynamic combustion process and figure out how this variation in the temperature input value affects all the other performance parameters.

These are the results obtained:

O/F = 7.07780   %FUEL = 12.379608   R,EQ.RATIO = 0.687620   PHI,EQ.RATIO = 0.647186

	CHAMBER	THROAT	EXIT
Pinf/P	1.000	1.8114	29.813
P [BAR]	16.600	9.1642	0.55681
T [K]	1458.0	1289.12	692.49
RHO [KG/CUM]	4.2213	2.6357	0.29812
H [KJ/KG]	-1782.54	-2002.4	-2732.26
U [KJ/KG]	-2175.78	-2350.09	-2919.03
G [KJ/KG]	-13071.8	-11984.1	-8094.20
S, [KJ/(KG)(K)]	7.7430	7.7430	7.7430
M, (1/n)	30.827	30.827	30.827
Cp, [KJ/(KG)(K)]	1.3143	1.2886	1.1416
GAMMAs	1.2582	1.2647	1.3094
SON VEL,[M/SEC]	703.4	663.1	494.5
MACH NUMBER	0.000	1.000	2.787
PERFORMANCE PARAMETERS			

Ae/At		1.0000	4.2539
CSTAR, [M/SEC]		949.8	949.8
CF		0.6982	1.4511
Ivac, [M/SEC]		1187.4	1513.7
Isp, [M/SEC]		663.1	1378.2

Table 21: NASA Cea output - imposed temperature

The gas constant is equal to:

$$R = \frac{P}{\rho T} = \frac{16.6 * 10^5}{4.2213 * 1458} = 269.71 \ {J}/{KgK}$$

and the isentropic factor is

$$\gamma = 1.2582$$

In this case is possible to see that the combustion chamber temperature is fixed at 1458 K and it leads to a variation in the Mach number and performance parameters.
However this kind of simulation setting is not so correct due to the fact that it is a forcing in the replication of the phenomena keeping fixed the mixture ratio and chamber temperature, preventing the software to perform the iterations required to define the exact temperature in the combustion chamber.

14. Tau code model: imposed temperature

At NASA Cea analysis follows the Tau code simulation with the same hypothesis used for the Chap.11. Also in this case the percentage of points and elements which could be added or removed in each adaptation is 30% and the complete loops is performed. The thermodynamic values set for this simulation are:

Chamber Temperature	1458 K
Chamber pressure	$16.6*10^5$ Pa
Reference Temperature	300 K
Reference Pressure	101325 Pa
Chamber density	4.2213 kg/m^3
Gas constant R	269.71 J/kgK
Isentropic factor Υ	1.2582

Table 22: Thermodynamic values - R=269.71 J/kgK Tc=1458K

Also in this case, the Tau code simulation has the only aim to investigate the behavior of the flow with the new configuration with different chamber temperature. It is possible to notice that due to a reduction in the temperature, also the gas constant R decreases while the chamber density increases as the pressure remains constant. The isentropic factor in this case is higher than the one computed without forcing the combustion (see Chap.12). These are the results:
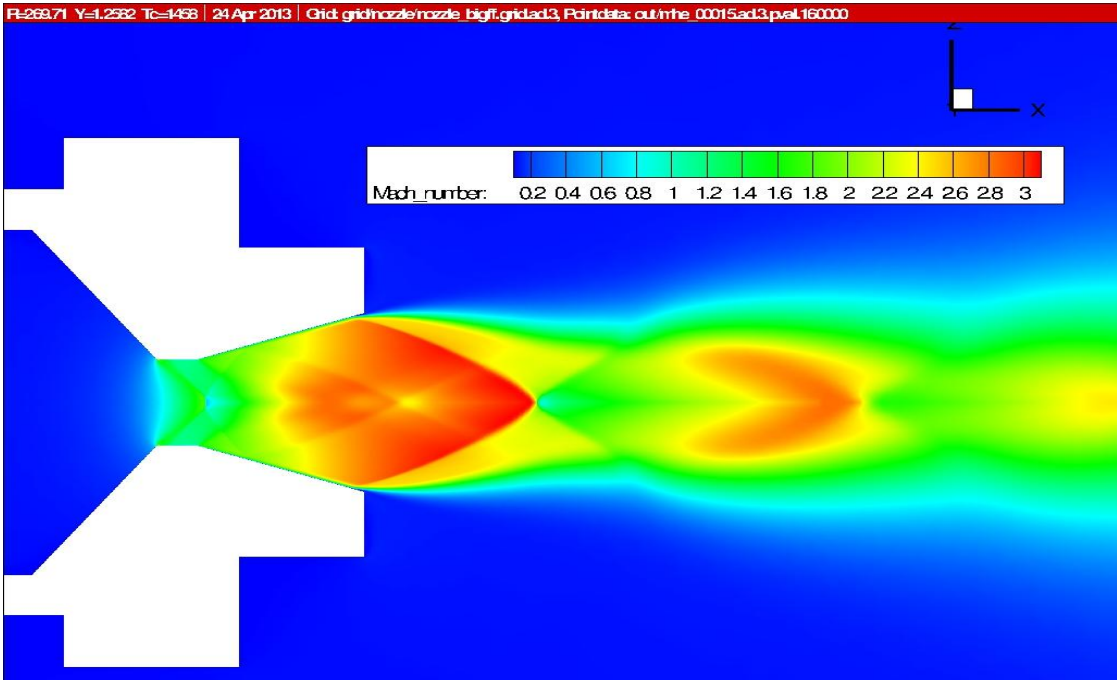
Figure 53: Tau Code simulation - Mach distribution. R= 269.71 J/kgK γ=1.2582
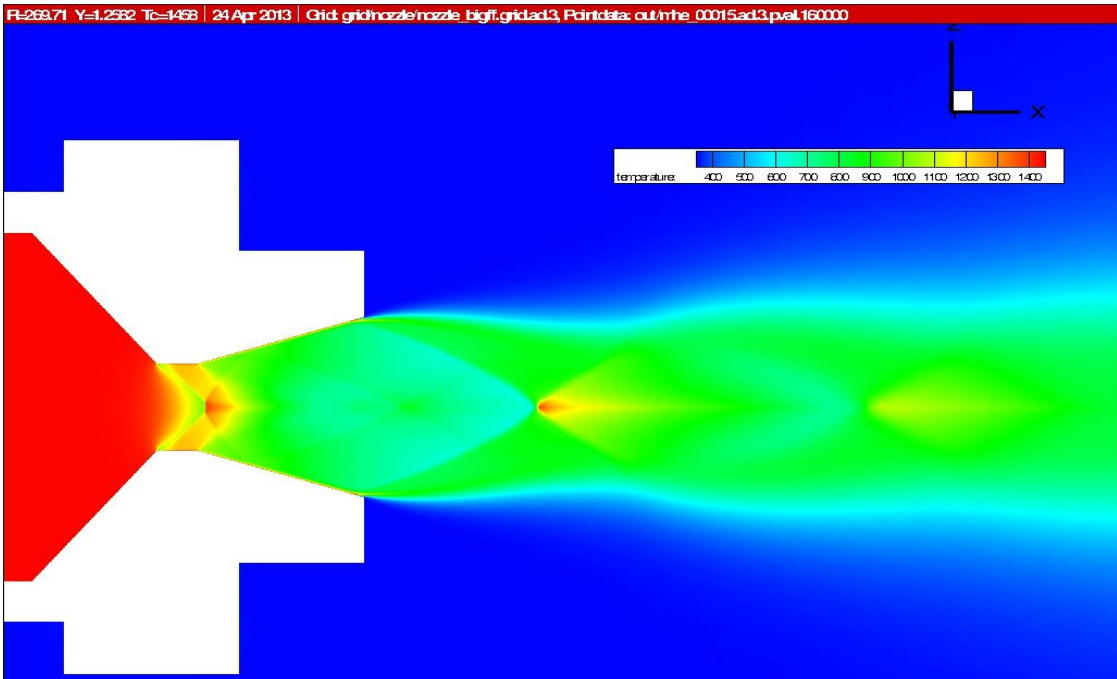
Figure 54: Tau Code simulation - Temperature distribution. R= 269.71 J/kgK γ=1.2582
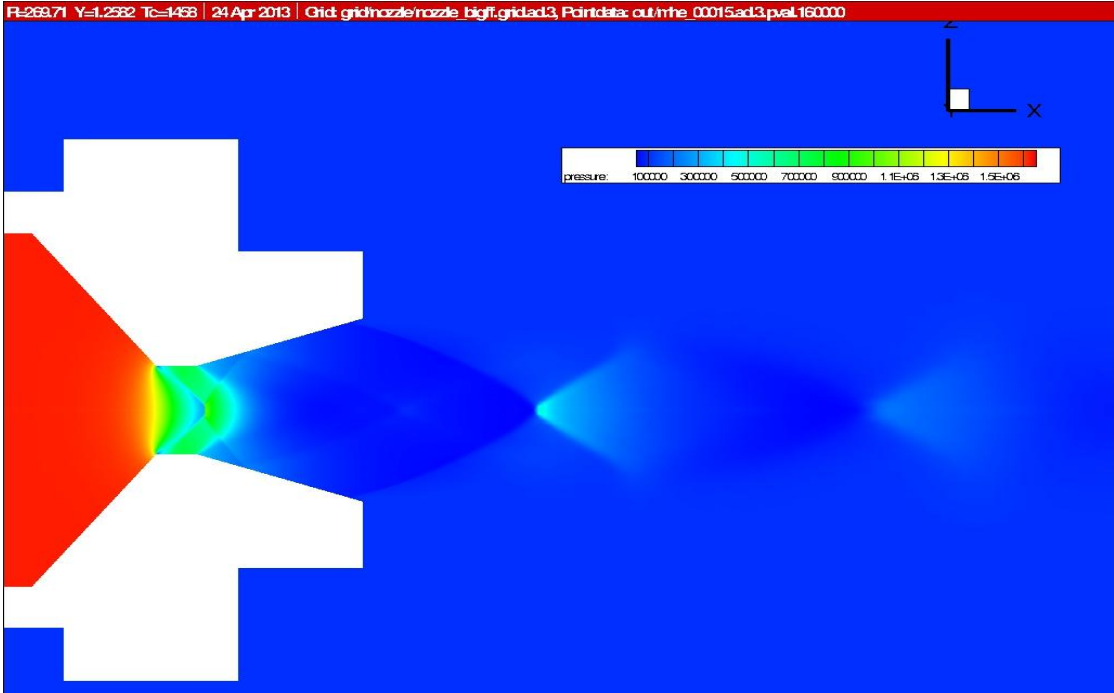
Figure 55: Tau Code simulation - Pressure distribution. R= 269.71 J/kgK γ=1.2582

A good mesh resolution and a convergent solution in a near-wall modeling is obtained, confirmed by the value of y^+ almost always close to 1:
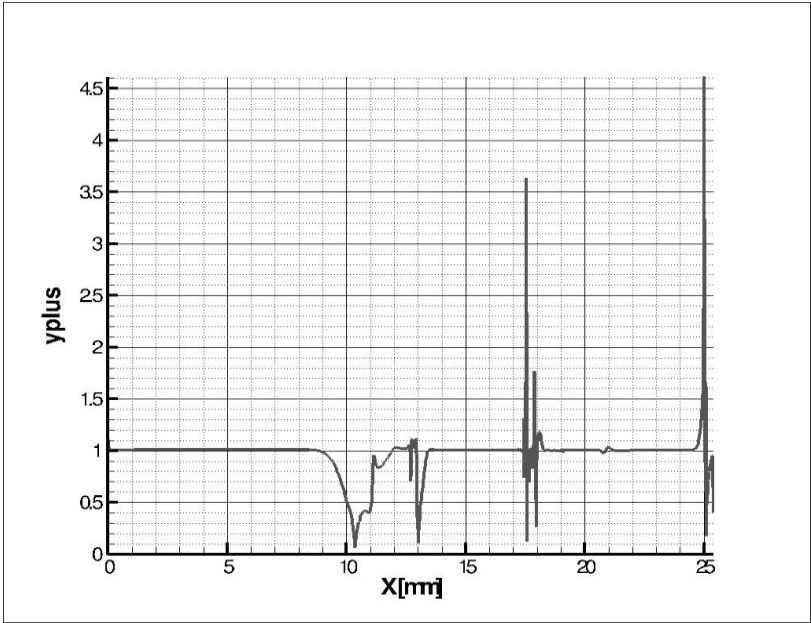
Figure 56: y^+ trend in the nozzle - R=269.71 J/kgK γ= 1.2582

The comparison between the Mach numbers provided by Tau code and NASA Cea demonstrate and confirm definitely the accordance between these two numerical models, due to an error of only 3% between these two results.
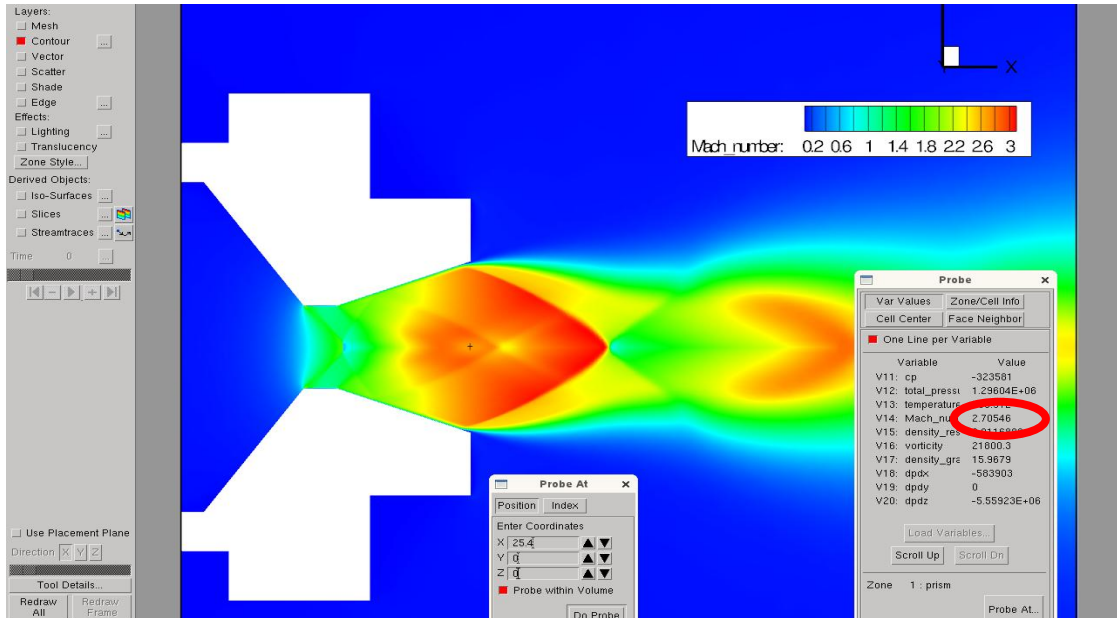
Figure 57: Tau Code calculation of Mach number. R=269.71 J/kgK γ=1.25828

The Mach and x-velocity trends are quite similar to those of the previous analysis. The thrust evaluation follows the same step and assumption of the Chap.12 and, due to the fact that this case of forced simulation is not of much interest, all these analysis are not reported here.

15. Infrared visualization

The main purpose of MHT study is to compare the numerical model and its results with the real phenomena and data come from the experimental campaign. The first comparison is made analyzing the sensors measurements and evaluating the most important performance parameters of a nozzle (mass flow rate, thrust…). A calculation of these parameters is in the Chap.12 in which the mass flow rate, specific impulse and the thrust for Tau code, NASA Cea and physical models are compared.

The next step concerns the study of temperature field which characterizes the whole system under analysis using an infrared camera. In this way is possible to record and take pictures of the experiment and in particular of the exhaust gases and of all the area surrounding the nozzle.

The operating principles of infrared imaging are based on the property of all the objects to emit a certain amount of radiation as a function of their temperature and the higher the object´s temperature is, the higher is the amount of infrared radiation emitted. The infrared radiation is the electromagnetic radiation with wavelength between 0.7 µm and 300 µm and it is strictly related to the vibrations of the molecules [8].

With an infrared camera is easy to detect these radiations and the integrated software transduces them into temperature variations. Different colors of the pictures imply different temperatures and the brightest and warmest areas are colored white, intermediate temperatures are reds and yellows while the dimmest and coolest parts blue and green.

With these simple notions it is possible to read and understand the following pictures related to some tests performed with the MHT:
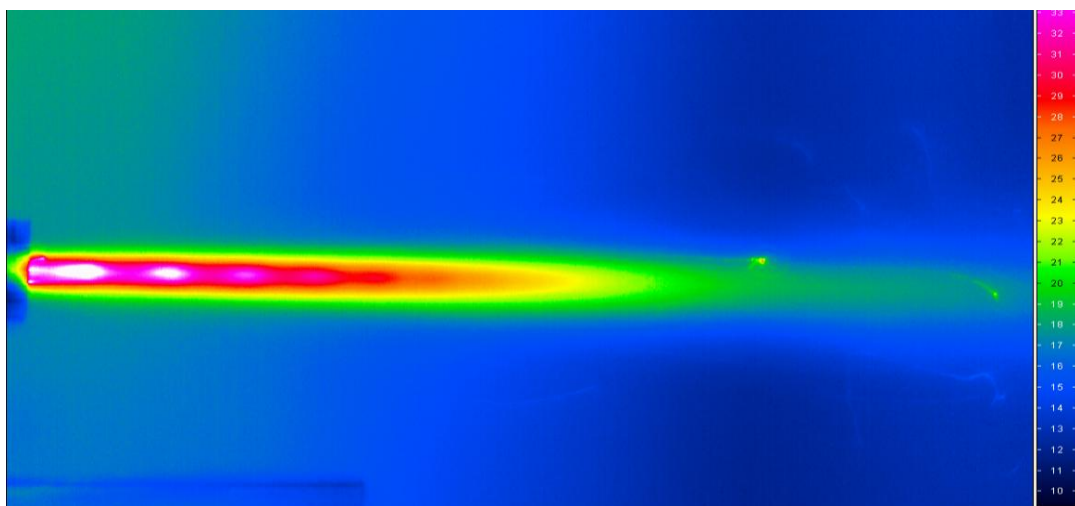
Figure 58: Infrared imaging of the exhaust gas temperature

All the infrared pictures are taken after about 0.5-0.6 s from the beginning of the combustion. It is the same moment detected from the sensors in which the exhaust flow is stabilized and there is a plateau in which the temperature reference point is evaluated.
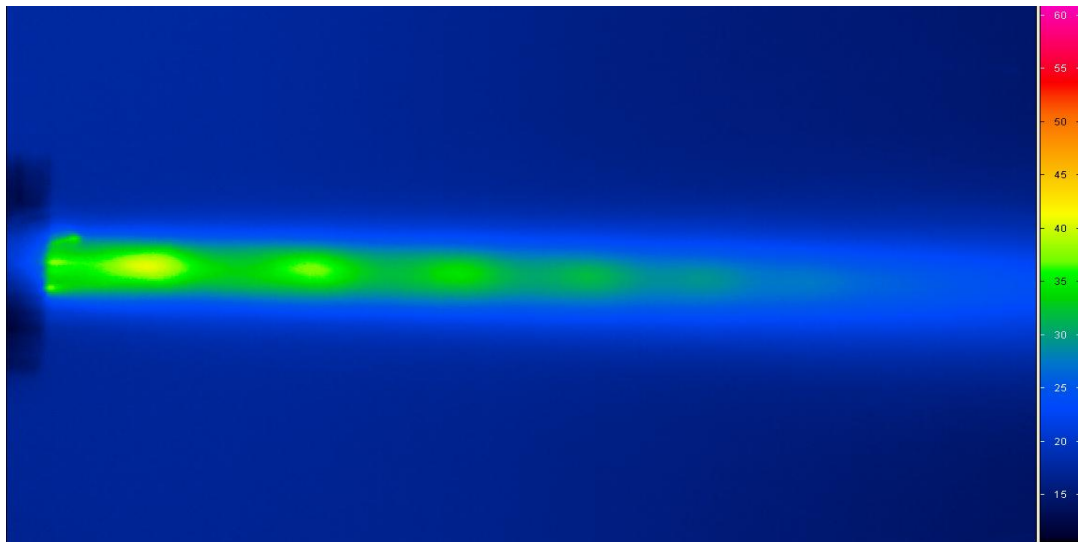
Figure 59: Infrared Mach pattern details in the exhaust

The thermal field is easy to investigate in the previous pictures where the areas with the highest temperature are described with different colors linked to the scale in the margin of the pictures. An important point has to be clarified: the values defined in the scale, are not the real temperature values in the field, because the camera used to record the experiment is calibrated to work and detect the electromagnetic radiation for solid objects while in this case, the main subjects of study are the gases flowing from the exit of the nozzle. Notwithstanding, the infrared imaging provides very important information about the distribution of the temperature and how it evolves giving a qualitative impression of the field.

As first, it is possible to evaluate the distance of the Mach disks from the exit of the nozzle looking both in the experimental infrared pictures and in the Tau code results. This analysis confirms that the temperature fields present the same distribution, and the numerical model and the experimental phenomena fit together.

The measurements on the infrared pictures are made with a simple ruler and, because of the distances have order of magnitude of few millimeters, they could be affected by measuring errors. However, the Mach patterns are very close to be at the same position in these two cases with small differences of 2-3 millimeters.

Looking at the following pictures, related to the previous simulation explained in the Chap.11,
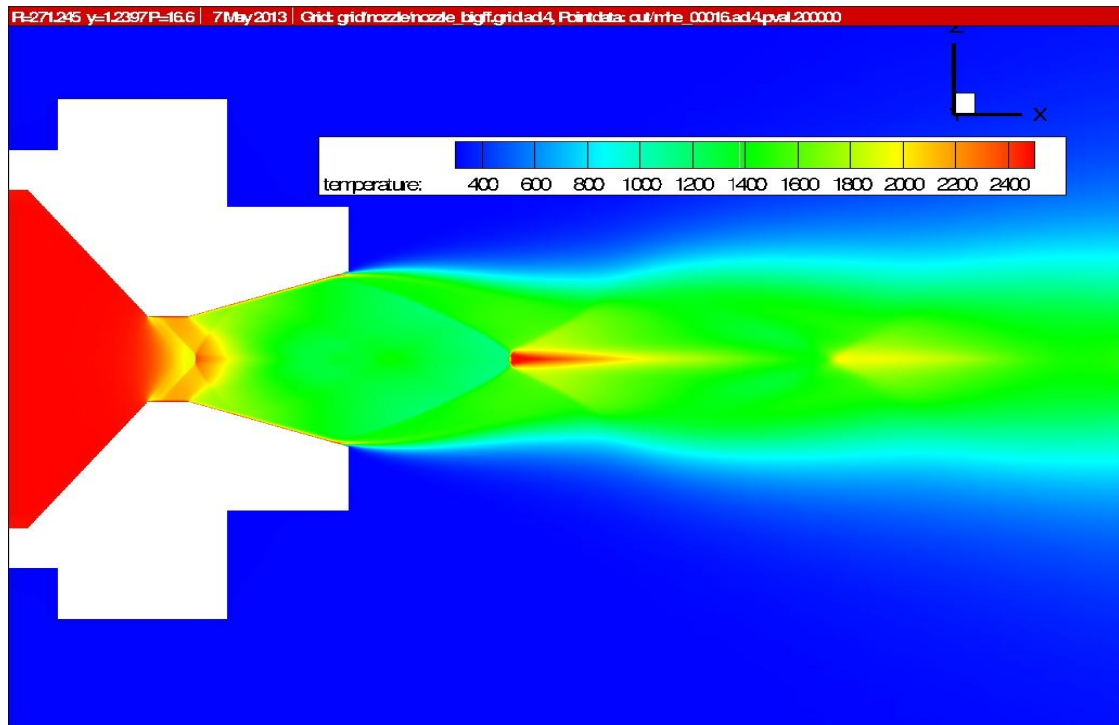
Figure 60: Temperature field with R=305.48 J/KgK and γ=1.2365

and making a comparison with the Fig.59, considering only the first two Mach disk, the following results emerge:

	IR picture	**Tau simulation**
1° Disk	33.15 mm	32.39 mm
2° Disk	47.8 mm	45.5 mm

Table 23: Mach patterns evaluation

There is a good accordance in the temperature distribution between the reality and the numerical simulation.

16. Schlieren technique visualization

The schlieren imaging is a powerful technique to study the behavior of a flow. The basic principle of the schlieren technique is the combination of the optical projection of an object with an indication of its light deflection [11].
Effectively the schlieren resulting image is an optical image formed by lens and lead a conjugate optical relationship to the schlieren object. This imaging method needs also a knife-edge able to cut off part of the reflected light otherwise it would be just a shadowgraph, not showing the density distribution in the observed area (as is in the schlieren purpose) but only some shadow of the flow. The description of each component and principles of the schlieren technique are discussed in this chapter.

16.1.   Introduction to schlieren technique

A definition of schlieren could be given according to [11]: the gradient disturbances of inhomogeneous transparent media is defined schlieren. These disturbances are relatively small refractive differences within the overall background and they bend the light rays in any direction other than normal direction z.
Schlieren phenomena occurs in solid, liquid and gases and they can be the consequences of temperature changes, high-speed flows, or the mixing of dissimilar materials. Some of these disturbances refract light very strongly, others barely at all. Some schlieren disturbances have also complicated structures and are sharply defined, while others are gradual but anyway distinguishable from the background.
The phenomena to be studied with the schlieren technique is called "schlieren objectives".
The basic principle of the schlieren technique is the combination of the optical projection of an object with an indication of its light deflection. The human eye has no way to distinguish the phase differences in a light beam but it can discern only amplitude, color contrast and polarization. With the schlieren techniques it is possible to see deeper: it translate phase differences into amplitude [11].
The features of this method of visualization is based on the characteristics of the light. It is useful then spent some words on that.
Light propagates uniformly through homogeneous media but, considering the atmosphere, the medium is not uniform. There are a lot of disturbances and inhomogeneities due to turbulence, thermal convection, weather phenomena and much more else. The disturbance changes the atmospheric density on a relatively small scale and with it, also the refractive index will change. As

consequences, the light rays are bent. That is what happened also in a small scales and characterized the real daily life phenomena.

Light interacts with matter and this interactions is expressed by the refractive index:

$$n = \frac{c_o}{c}$$

considering a transparent medium where c is the light speed in the medium considered and c_o is the speed of light in a vacuum equals to 3×10^2 m/s. For gases, there is a simple and linear relations between the refractive index and the gas density:

$$n - 1 = k\rho$$

where k is the Gladstone-Dale coefficient and it is about 0.23 cm^3/g for air at standard conditions. For other gases it may vary roughly from 0.1 to 1.5. Easily it can be notice how the refractive index depends upon ρ while the refractivity *n-1* of a gas, depends upon gas composition, temperature, density and wavelength of illumination. All the factors that lead to gas disturbance generate refract light that may be visualized by virtue of this refraction. A similar relation between n and rho exists also for liquid and solid but it is more complex and much less optical sensitivity of the schlieren apparatus is needed to see refractions in liquid or solids than air.

The physics of refractivity is characterized by special features that are occasionally useful: k increases slightly with increasing light wavelength λ; refractivity increases for a ionized gas and then a plasma refracts light even when the plasma density is quite low; some gases may absorb significant light leading the refractivity higher than normal. Another and important features which is the base for the schlieren techniques is the possibility of the light rays to bend and refract. The presence of the inhomogeneities in the area of interest, refract or bend the light rays in proportion to their gradients of refractive index . The rays are bended according to these relations:

$$\frac{\partial^2 x}{\partial z^2} = \frac{1}{n}\frac{\partial n}{\partial x} \quad \frac{\partial^2 y}{\partial z^2} = \frac{1}{n}\frac{\partial n}{\partial y}$$

and integrating it is possible to evaluate the angular ray deflection in the x and y directions:

$$\varepsilon_x = \frac{1}{n}\int \frac{\partial n}{\partial x} dz \quad \varepsilon_y = \frac{1}{n}\int \frac{\partial n}{\partial y} dz$$

and considering two-dimensional schlieren of extent L along the optical axis this become:

$$\varepsilon_x = \frac{L}{n_0}\frac{\partial n}{\partial x} \quad \varepsilon_y = \frac{1}{n_0}\frac{\partial n}{\partial y}$$

where n_0 is the refractive index of the surrounding medium and the gradients are responsible of the refraction. A region without such gradients is homogeneous and then not interesting in terms of reflecting light. These mathematical expressions are the basis for the schlieren technique and show that light rays are bended toward the region of higher *n*, that means toward regions with of higher density.

The schlieren method is closely and related to the shadowgraphy but several are the differences between these two methods. The shadowgraph does not produce an optical image but simply reproduce shadow. The schlieren image instead is an optical image formed by lens and requires a knife-edge of some other cutoff of the reflected light, while no cutoff or knife-edge are needed for the shadowgraphy. The peculiarity of the schlieren visualizations is that it displays the deflection angle ε while shadowgraphy displays the ray displacements resulting from the deflection. Another distinction between the two techniques lies in the set-up requested and the effort required. The shadowgraph is very simple but the schlieren visualization got the advantages of much higher sensitivity.

16.2.   Simple lens type schlieren system

The easiest possibility to observe the interested phenomena with the schlieren technique is to use a point light source, two lens and a knife-edge. The beam from the point source is collimated by a lens and then, a second lens refocuses the beam to an image of the point source. From there the beam proceeds to a viewing screen where a real inverted image of the test area is formed. At this point the optical system is just a projector and transparent schlieren objects are not imaged until a knife-edge, typically an ordinary razor blade, is added at the focus of the second lens.

Adding the schlieren object to the test area, it bends light rays away from their original paths and the second lens focuses the ray from each point of the object to a corresponding point in the screen image. The Fig.61 shows two such rays, one bent upward and the other downward. The upward deflected ray generates a luminous point on the screen while the downward deflected ray hits the knife-edge and the corresponding point is dark, being the ray blocked by the knife-

edge. For this particular point, the phase difference is converted to an amplitude difference due to a vertical gradient $\partial n/\partial x$.
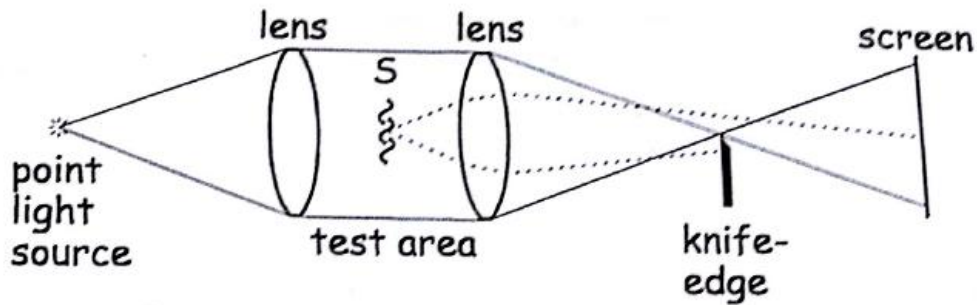
Figure 61: Simple schlieren system with point light source [11]

Generalizing, a finite schlieren object refracts many rays in many directions. All downward components of these ray deflections are blocked by the knife-edge coloring dark partial area of the image. The scheme presented in Fig.61 is very simple schlieren system which could be improved based on the same basic principles.

A clarification about the knife-edge is necessary. Its position in the system affects so much the results of the visualizations on the screen. When horizontal, it detects only vertical component $\partial n/\partial y$ of the deflected ray and only those ray refractions with components perpendicular to it. Refractions parallel to the edge, due to $\partial n/\partial x$, are not interested in the cutoff and then the screen illumination does not change. To have a complete portray of the schlieren object two images are needed with two different orientation of the knife-edge: one horizontal and one vertical. But in this case, the difficulty and the efforts request from the schlieren technique becomes too high: in practice, a single knife-edge correctly oriented is often good enough.

To describe the schlieren basic and system, a point light source is considered. This choice is not so practical and an extended light source is generally required. An additional focusing lens is needed after the knife-edge. This configurations could be seen in the Fig.62. Collimated by the first lens, the lights beam traverses the test area and is refocused by a second lens to form an inverted image of the source at the knife-edge.
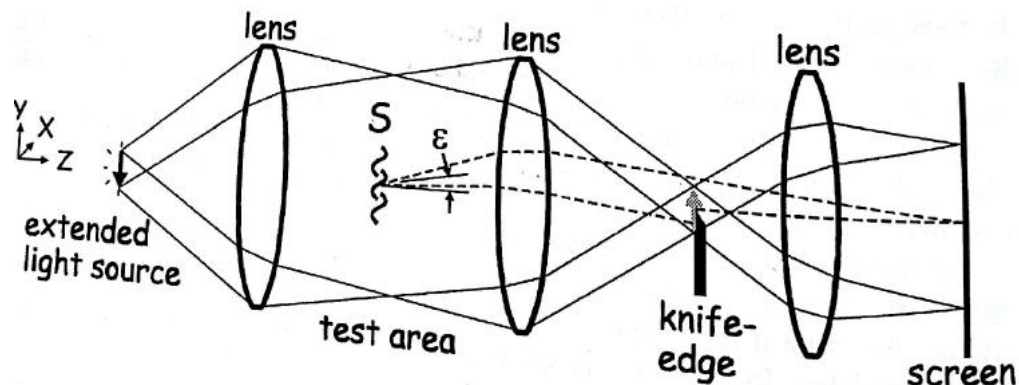
Figure 62: Simple schlieren system with extended light source [11]

Because the light source is no longer a point, collimation does not produce exactly parallel rays, generating an array of point sources distributed along the vertical height of the extended source. Each point produces a schlieren beam that focuses to a corresponding point in the light source image at the knife-edge. The knife-edge blocks a portion of the image of the extended source. Beyond the knife-edge, a third lens is used to focus an inverted image of the schlieren test area on the viewing screen.

Because the light source now has finite size, every point in the test area is illuminated by countless rays within a cone limited by the extremities of the source and each point in the light source illuminates every test area point. It is possible to consider a ray bundle from all light source points which suffer of a refraction angle ε. This ray bundle originated at the test area is returned by the second lens to the same relative position in the conjugate image plane on the screen. It gives the possibility to separate the light rays refracted by schlieren object in the test area from the ordinary rays that provide the background illuminance.

Once separated, the refracted light is marked by a different amount of cutoff at the knife-edge, then recombined in the schlieren image to yield illuminance variations with respect to the background. The final schlieren image is built up of many points of varying illuminance corresponding to the shape and strength of the refractive schlieren object. The use of the extended light source allows a continuous gray scale image rather than a simple black and white image.

The third focusing lens is used to adjust the scale of images for various uses. Although frequently used for convenient image sizing, it is not absolutely essential while the second lens can produce a useful schlieren image by itself if the distance from the test area to the objective is appropriate.

16.3.   Schlieren system set-up and results

According to the basics of the schlieren technique described in the Chap.16.1 and 16.2, an appropriate set-up is prepared to study the exhaust gases of the micro hybrid thruster. Three lens with different focal lengths, each one with a different aim: the first collimates the light in a defined beam, the second lens refocuses the beam to an image of the point source and the third one adjusts the scale of images. A knife-edge to cut off part of the reflected light providing an image with high contrast, a slit with the purpose of restricting the light beam and a simple light source or lamp are used to completely assemble the visualization system. All the signals passing through these lenses system are recorded by a high speed camera (PHOTRON SA5 FASTCAM) which transfers all the information to the software able to visualize in the monitor the density distribution as differences in the colors.

The components and its features are presented below together with pictures of the complete set-up used for the test rig, including the distances between them.
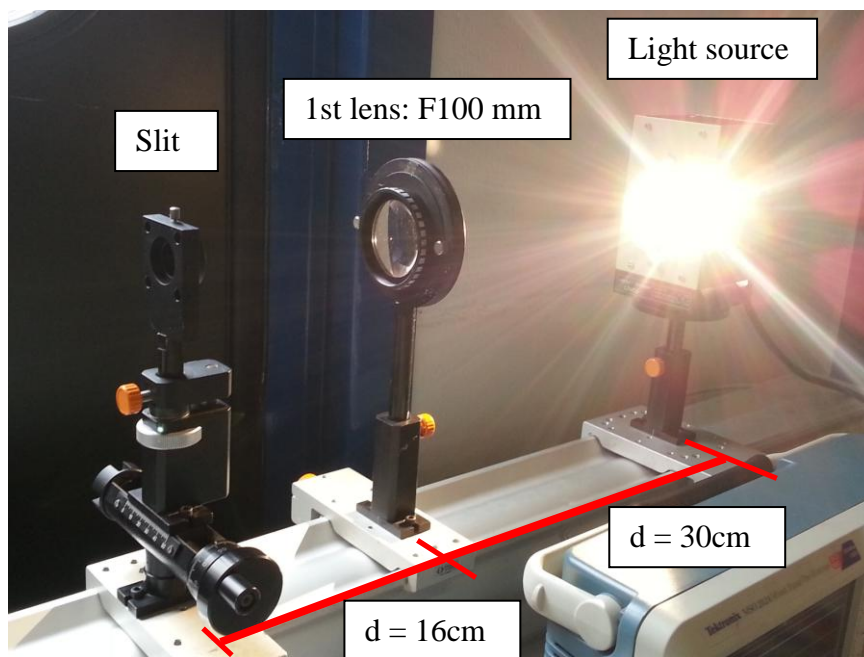
Figure 63: Schlieren set- up - Lamp, lens and slit
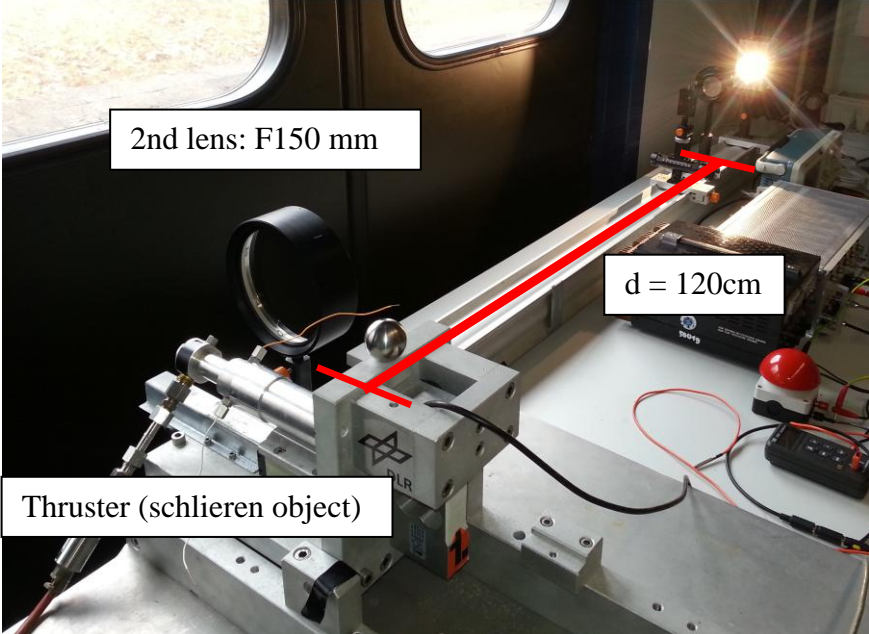
Figure 64: Schlieren setup - Lamp, lenses, slit and mht
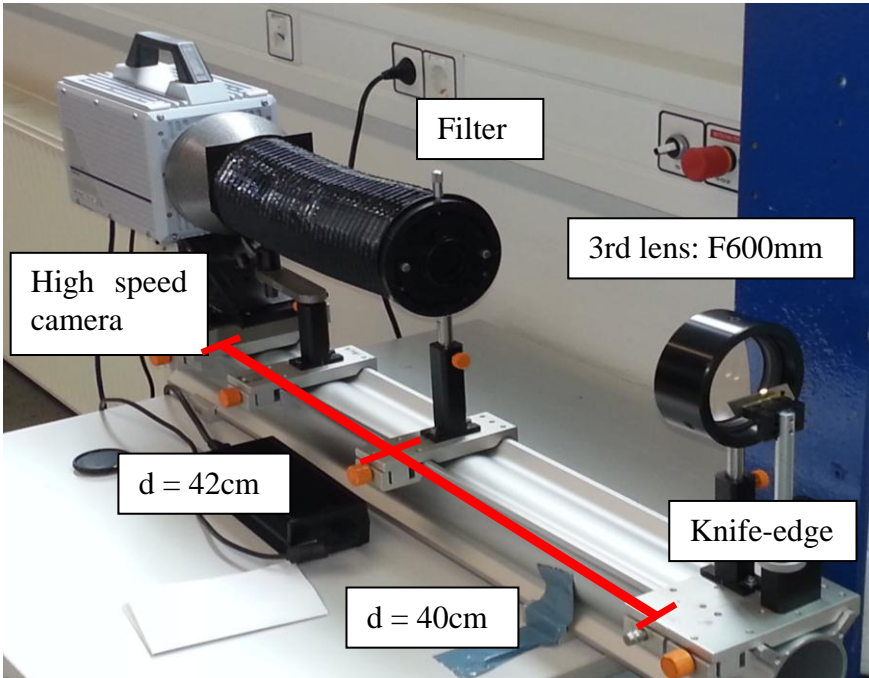
Figure 65: Schlieren setup - Camera, lens and knife-edge
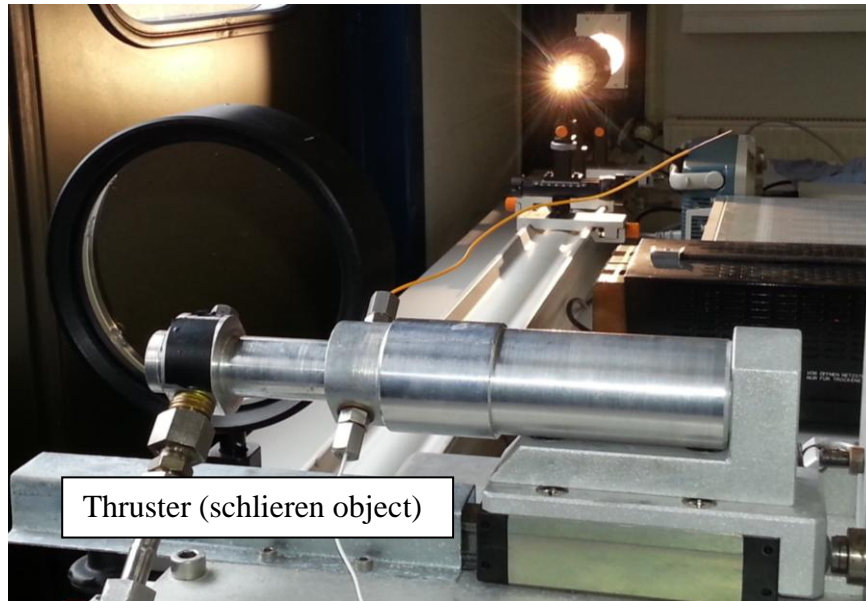
Figure 66: Schlieren setup partial view

The main purpose of using the schlieren imagery for the study of the MHT is to visualize the exhaust gases and observe the flow field and its structures, especially the Mach pattern.

The attention is focused on the initial moments of the start-up of the combustion and in particular after 0.5 s from the ignition when the flow is supposed to be fully developed and a plateau is registered by the measurement chain sensors (see Chap.9).

The images provided from the schlieren method are the following, related to different tests:
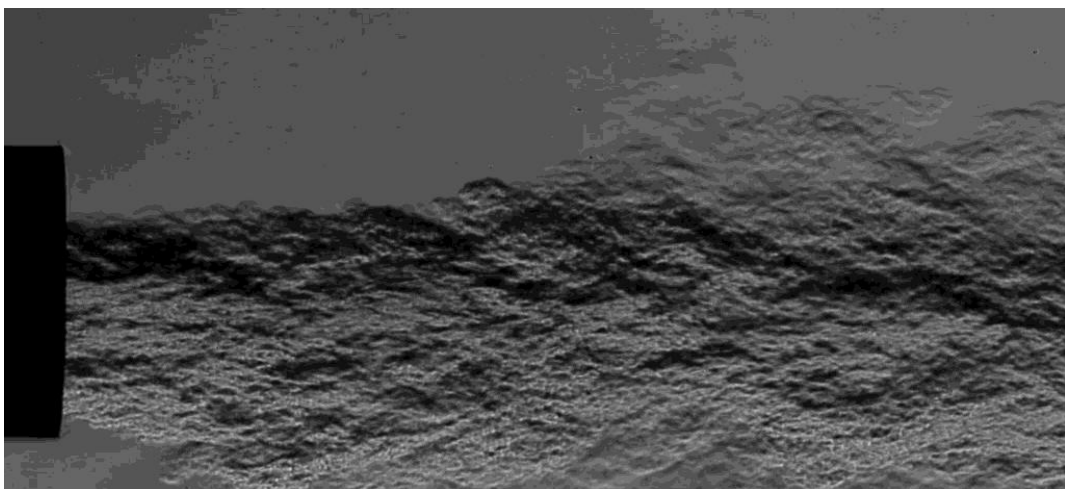
Figure 67: Schlieren image after 0.58s – Test 0014
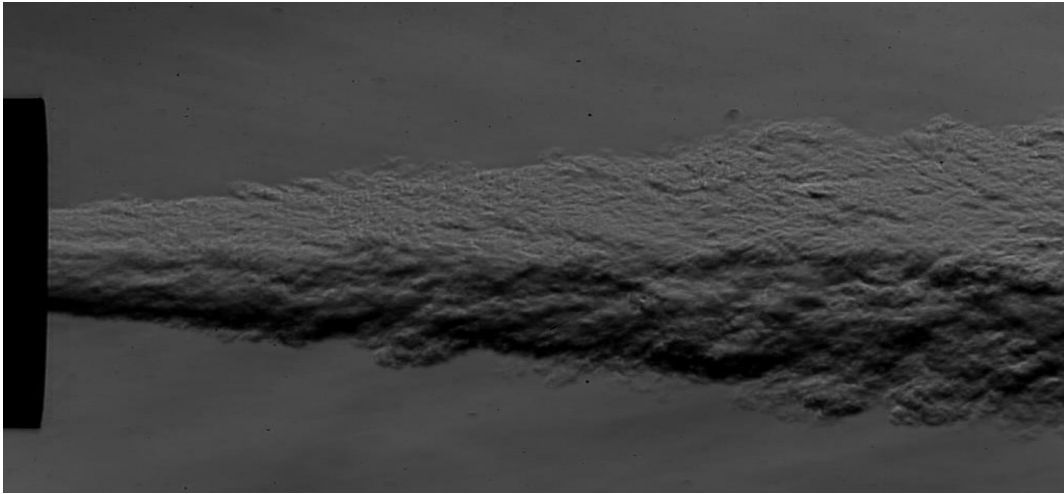
Figure 68: Schlieren image after 0.53s – Test 0015
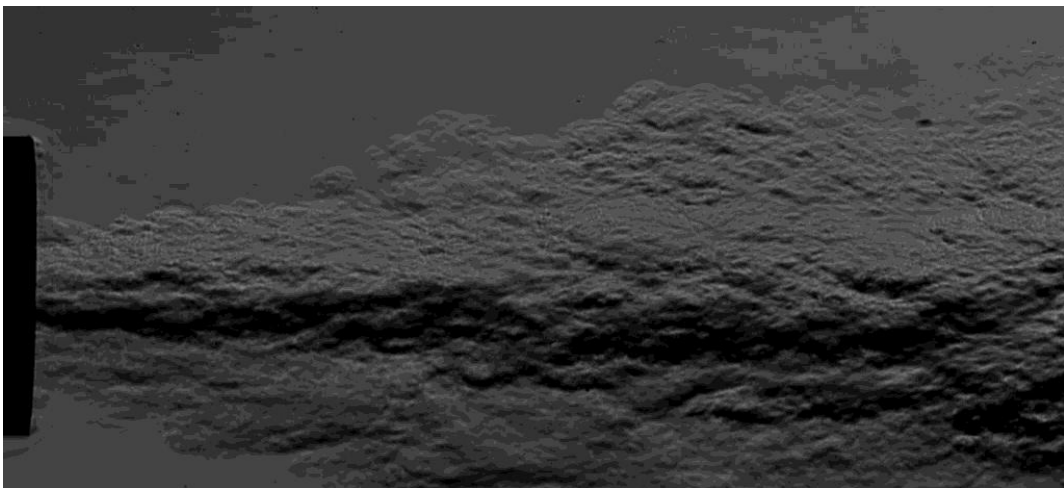
Figure 69: Schlieren image after 0.84s – Test 0016

Looking at these pictures taking from three different tests, it is possible to observe the exhaust flow and its turbulent behavior in the mixing area with the atmosphere. It´s clear the difference between the hot flow coming out from the nozzle and the environment. But the main idea to analyze the Mach distribution in the flow field is here not possible: any Mach disks or other discontinuities inside the flame are not visualized due to the plume surrounding it. A reasonable explanation for this is that the density distribution is not uniform especially near the exhaust flow. This means there is a high density gradient in that area.

According to the schlieren method, a high value of density corresponds to a dark colored region in the images captured by the camera, while the clearest areas are characterized by low density. And this led to the following reasoning: the plume

has higher density in comparison with the inner flow and that means it appears darker in the recorded images, covering all the other colors related to the lower density of the real exhaust flow. Somewhere there are some spots through which the light rays from the lamp could overcome the plume but it is not possible to distinguished correctly between the plume and the jet (a simple sketch of this is represented in Fig.70).

Another possibility to observe the Mach region is to take picture with schlieren camera away from the exit nozzle where the plume is not predominant anymore but in that region there is no interesting information about Mach distribution of the flow (too far from the nozzle exit) and then this solution is useless for the purpose.
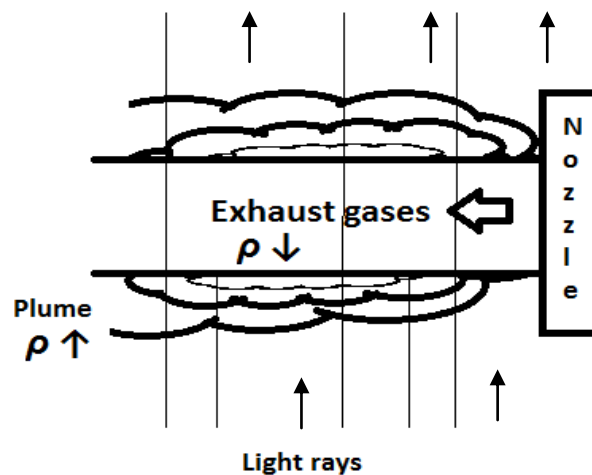
Figure 70: Sketch of the nozzle exit gases

With the infrared imaging this problem is not experienced because the flame is very hot, then very bright, especially when there are Mach disks with a consequent increasing of the temperature. In this situation is easy to detect and visualized the Mach pattern as it is possible to see in Fig.58 and 59.

A confirmation of the problem discussed above is given also by the Tau code results and the Fig.71, in which is possible to see the density distribution which is higher in the border of the jet than inside it. The simulation used as reference is that analyzed in Chap.11 concerned with gas constant R=271.245 J/kgK, γ=1.2397 and a combustion chamber temperature equals to 2528.58 K.
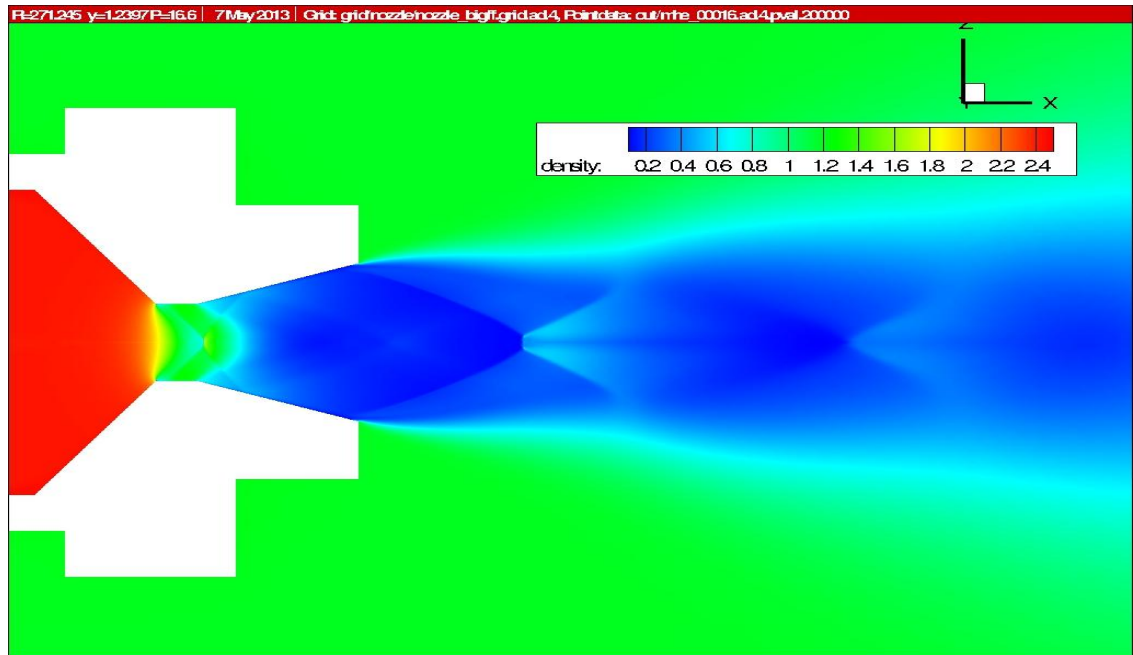
Figure 71: CFD simulation - Density distribution - R= 271.245 J/kgK γ=1.2397

It is possible to see clearly what has been said above watching at the density trend along Z axis at X=60 mm (Fig.72): moving inside the exhaust flow the density decreases rapidly confirming that the plume doesn't permit to study inside the flame.
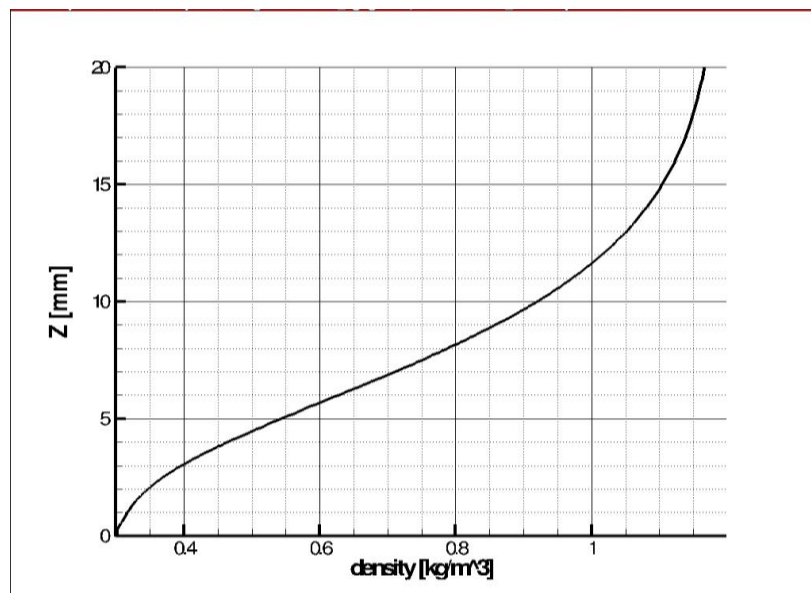
Figure 72: Density distribution plot. R=271.245 J/kgK γ=1.2397

The Fig.73 is only to have an accurate sight of the behavior of the density close to the symmetry axis Z=0.
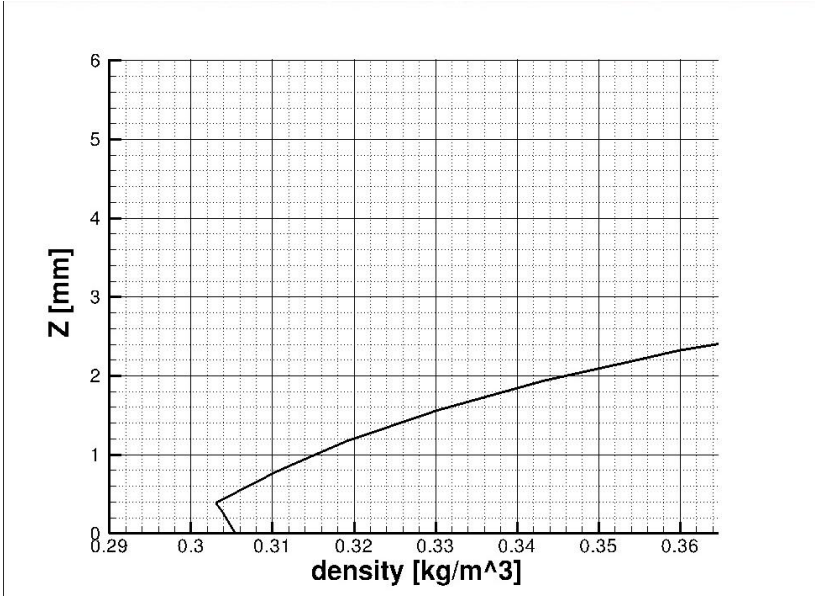
Figure 73: Density distribution plot – Zoom. R=271.245 J/kgK γ=1.2397

17. Co-flow

During its operational life, a nozzle passes through different phases: from the start-up of the engine at ground level, the flight phase during which the spacecraft leaving the atmosphere, until arriving at the desired orbit. In the first moments of the lift-off, the ambient condition is stationary and it is possible to assume there is no velocity in the environmental flow surrounding the nozzle. This situation is well represented by the whole simulations and discussions presented till now, where no co-flow is present and the environment is considered in steady state.

After the lift-off, the spacecraft is in flight mode and now the velocity of the air co-flow is not equal to *0 m/s* anymore. This is the configuration that is discussed in this chapter where all the parameters are unvaried and the only one changed is the air velocity of the ambient.

A velocity of *200 m/s* is established for the co-flow which corresponds to a Mach number around 0.5 and this causes a naturally increasing of the total pressure due to the fact that the static reference pressure is not changed from the previous analysis and is equals to 101325 Pa while now the dynamic pressure is higher and different from zero.

With this introduction, new simulations are performed using Tau code to figure out the behavior of the nozzle in this new condition.

First of all it is necessary to remember which parameters are used:

Chamber Temperature	2528.58 K
Chamber pressure	$16.6*10^5$ Pa
Reference Temperature	300 K
Reference Pressure	101325 Pa
Chamber density	2.4203 kg/m^3
Gas constant R	271.245 J/kgK
Isentropic factor γ	1.2397
Co-flow velocity	200 m/s

Table 24: Thermodynamic values for co-flow simulation

The values used and presented above in the Tab.24 are referred to a previous analysis with NASA Cea presented in Chap.10, using the PET as fuel, actually used during the test campaign.

However what this simulation wants to highlight are the differences in the behavior of the nozzle in case of flight mode and start-up, which means respectively with and without the presence of co-flow.

Then, the simulation produces the following results:
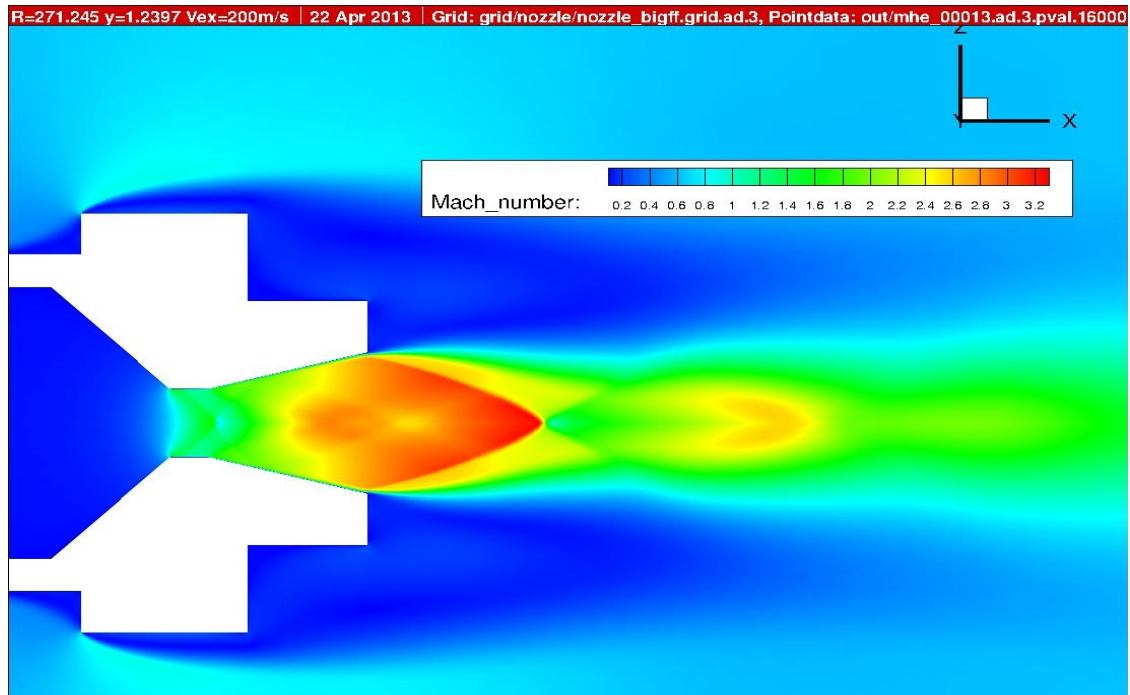
Figure 74: Tau Code simulation - Mach distribution - R=271.245 J/kgK γ=1.2397 v=200 m/s

It is possible to notice in the Fig.74 how the Mach number changes respect to the previous cases in the area outside the nozzle, mostly near its edges due to the variation of the velocity. Now the Mach number in the far-field does not tend to zero but it settles to the asymptotic value of about 0.5, like shown in Fig.80.

The presence of the co-flow generates also a modification in the Mach distribution and the shape of the Mach disks in the jet compared to the Fig.44 related at the simulation with any co-flow. However, a more significant comparison is presented hereafter in the Fig.75 where it is possible to see the difference in the Mach distribution between these two configurations. The same structure of the simulation is used, which implies the usual five CFL loops and four adaptations.
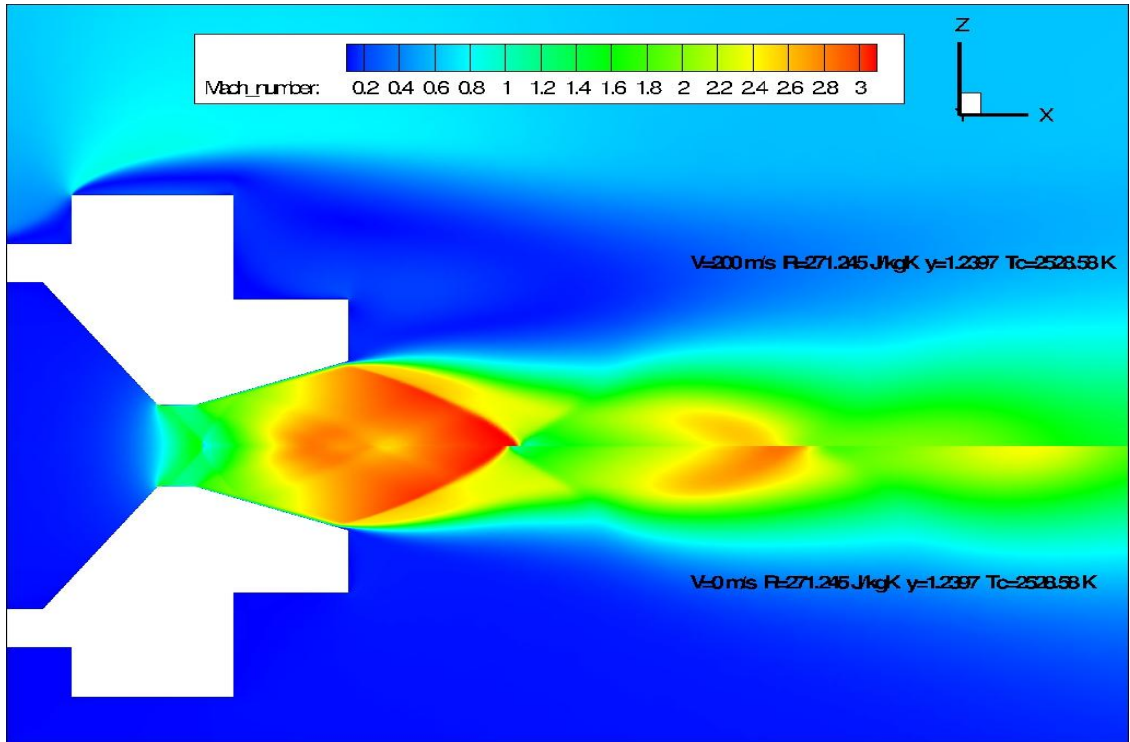
Figure 75: Tau Code simulation - Mach comparison with V=0 m/s and V=200 m/s
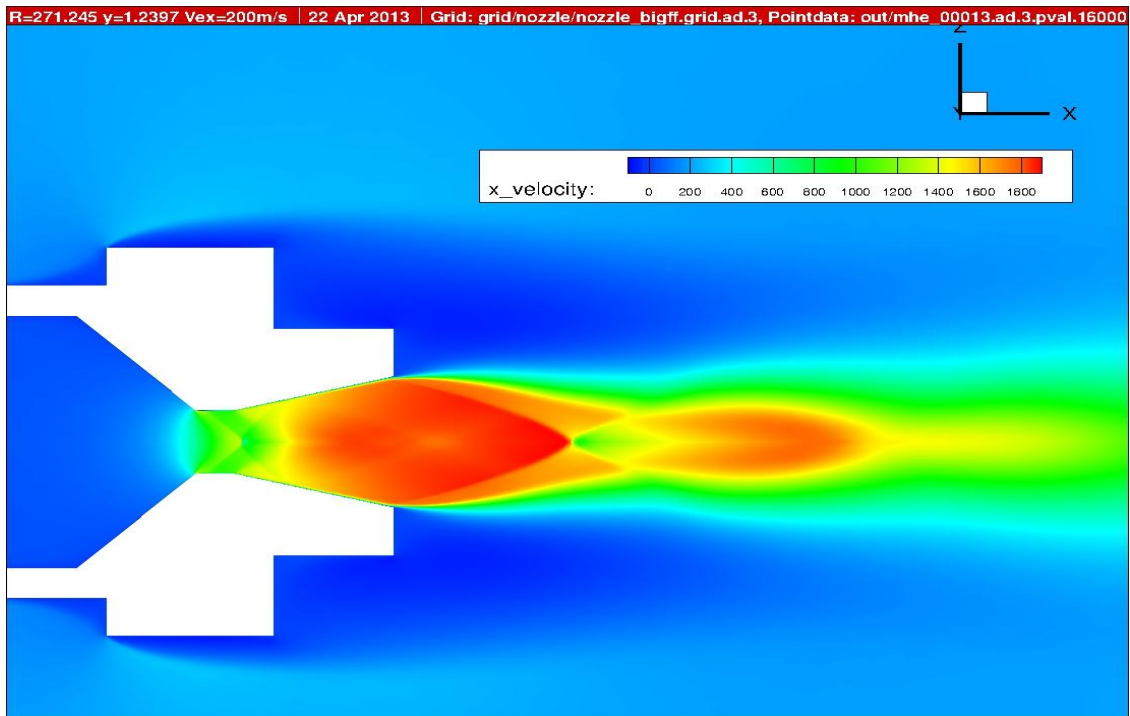
Figure 76: Tau Code simulation - Velocity distribution - R=271.245 J/kgK γ=1.2397 V=200 m/s

As usual the pressure and temperature distribution are shown:
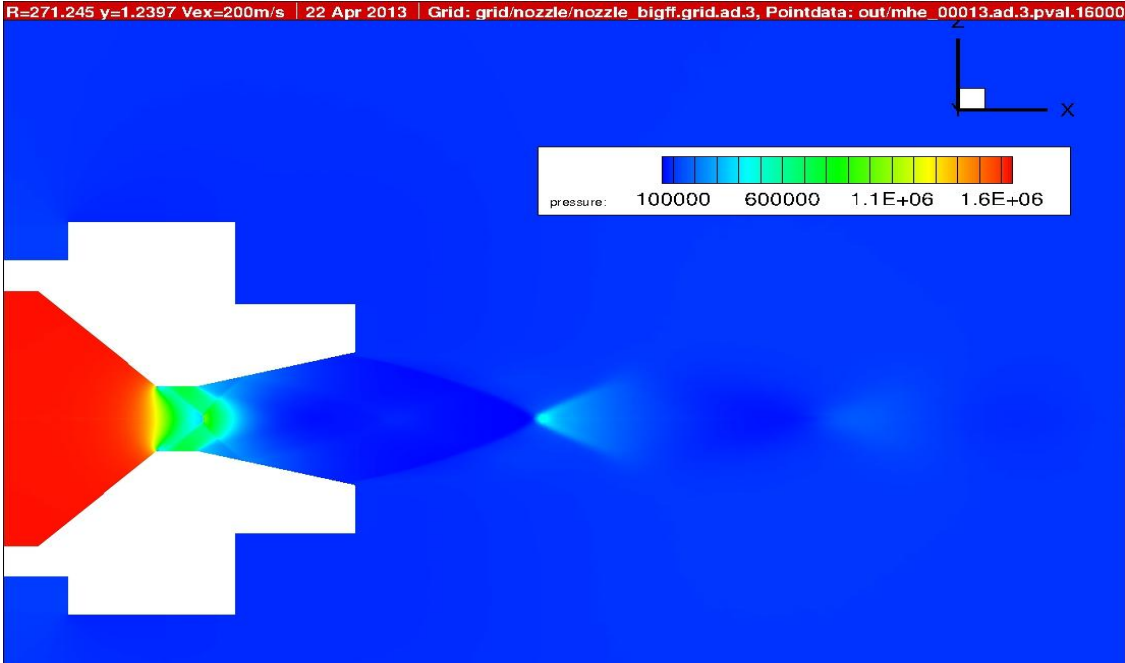
Figure 77: Tau Code simulation - Pressure distribution - R=271.245 J/kgK γ=1.2397 V=200 m/s
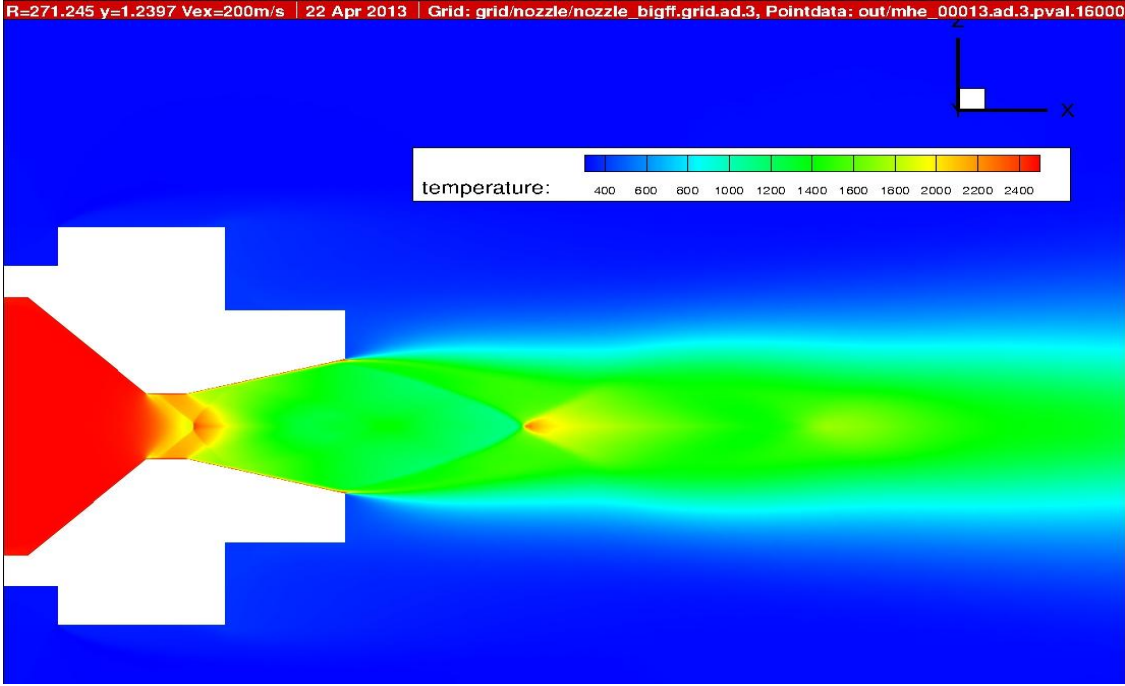
Figure 78: Tau Code simulation - Temperature distribution - R=271.245 J/kgK γ=1.2397 V=200 m/s

The modification in the input parameters does not affect the convergence of the simulation and the accuracy of the mesh:
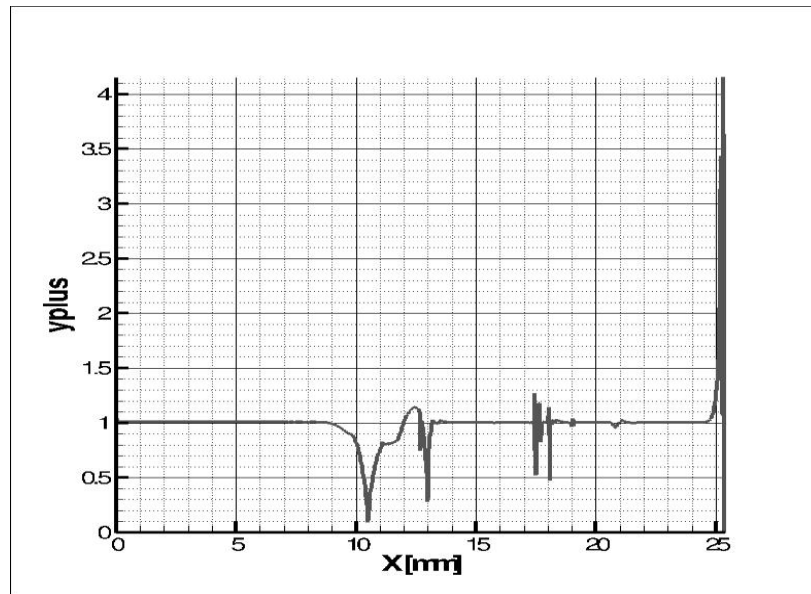
Figure 79: y^+ trend in the nozzle - R=271.245 J/kgK γ=1.2397 V=200 m/s

At this point it necessary to make a further comparison between this case and the one which does not consider the presence of the co-flow. Only in this way is possible to understand the real differences and similarities in these two situations.

Regarding the Mach number distribution along the symmetry axis of the nozzle (coordinate Z=0 mm), the Mach number inside the nozzle in the case without co-flow (blue line in Fig.80) is of course the same of that with the presence of co-flow (red line in the Fig.80); in the closest area of the nozzle exit until a distance of about 50/55 mm, the absence of a co-flow lead to a higher Mach number until the flow is extinguished after 3/4 diameters behind the nozzle. For that reason far away from the nozzle exit, the Mach number is higher in case of co-flow because of the contribution of the air velocity in the surrounding environment: the value is stabilized around 0.5 for the co-flow while in the other case the Mach number tends to zero.

Remember that the length of the modeled nozzle is equals to 25.4 mm and the reference system has the X-axis along the symmetry one and the zero is at the beginning of the combustion chamber, the Z-axis upwards from the symmetry axis and the third Y-axis is binormal to both according to the right–hand rule.
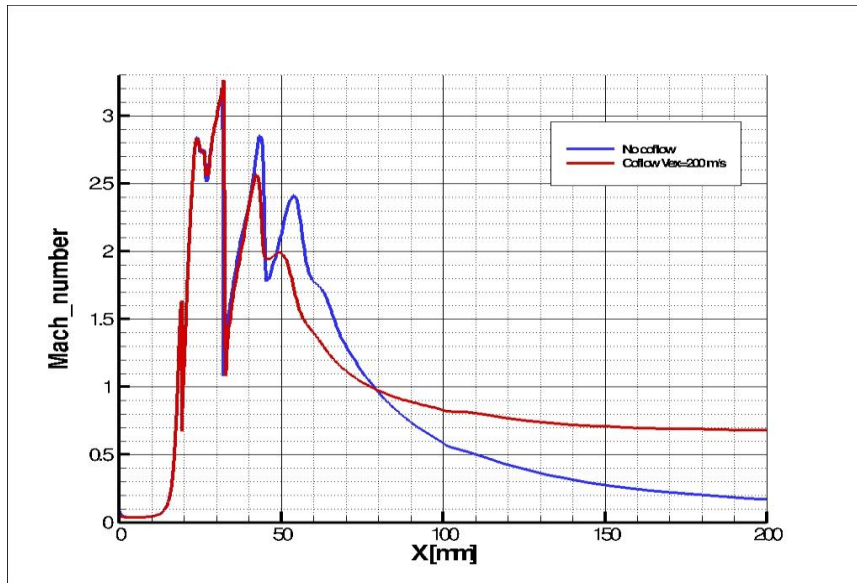
Figure 80: Mach comparison: co-flow (red) and no co-flow (blue)

It is interesting also to observe the Mach number trend along the Z-axis at a distance of 34.6 mm from the nozzle exit (60 mm of the total length). In this case, outside the jet, the Mach number related to the co-flow (red line in Fig.81) is higher than the value without its presence (blue line in Fig.81) but the situation is reversed getting closer inside of the jet. This can be explained by recalling the mass flow rate conservation principle in the entire domain.
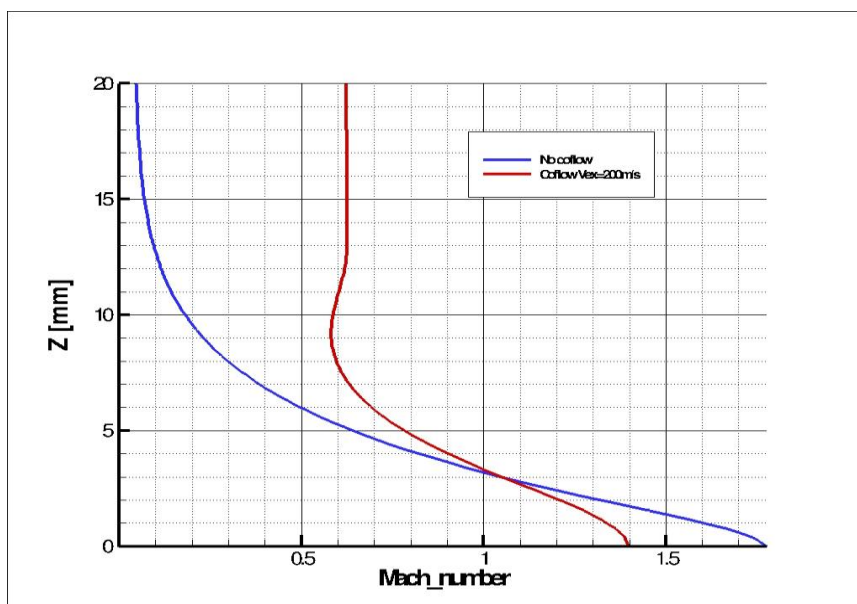
Figure 81: Mach comparison in Z direction: co-flow (red) and no co-flow (blue)

18. Advanced configuration and future generation

Several configuration of the MHT are tested during the experimental campaign with different results and sometimes also failures. The first configuration implies the electric pill coming inside the combustion chamber from the nozzle. The head of the electric pill is then surrounding with black powder able to burn and both break the diaphragm and start the combustion with the spark from the igniter pill. This configuration is not used anymore and in particular it is avoided during the recording of the process with IR and schlieren camera, due to the fact that the wires, coming out from the nozzle, obstruct the visualization. Another problem is that in this first configuration the wires are inside the combustion chamber modifying the dynamic of the combustion.

The current and definitive configuration is the one in which the wires of the igniter pill come out from the lateral holes of the case of the thrust. The electric pill should be exactly below the diaphragm and surrounded by a sufficient amount of black powder to guarantee the ignition. With this configuration there is not interference with the exhaust flow and also with the combustion in the chamber. But the amount of black powder and the correct position of the igniter pill are very important for the hot test: just few millimeters away from the correct position under the diaphragm and/or a not enough quantity of powder could be the reasons for a failure in the test. Using the black powder, also another problem occurs: during the ignition, the strong explosion generates a lot of particles that affect the exhaust gases and its measurement. To avoid this, it could be better to use something else instead of the black powder for the ignition.

Several tests and experiments are performed with various inflammable materials. The best results are obtained using a solid mixture containing kerosene and magnesium powder pasted on its surface. This solution gives a good and durable flame but it is not so easy to ignite it with the electric pill due to the fact that there is not so much air in the case of the MHT and this inhibits the combustion of the igniter. The failures in the ignition with this configuration occur frequently.

A new and more reliable configuration is then needed to reduce as much as possible the failures providing good results. This is the aim of the new generation of MHT, at the moment of this report under construction, which consists in a thruster of bigger dimensions, external lines of feed for the oxidizer and a nitrogen dedicated line for pipe cleaning and evacuation. Several tests will be conduct on this new version of hybrid thruster to confirm the possibility, now only theoretical, to provide up to 100 N of thrust.

19. Problems & Failures

In this first part of test campaign, different tests are performed. Of course many failures occurred and it is a good thing taking trace of them for a better further investigation. Then hereafter, a brief list of the failures experienced is presented:

- *Ignition failures*: in some cases the combustion in the MHT doesn´t occur and it happened also in the previous test campaigns by Padoan L. It is probably due to the ignition system not correctly positioned: the electric pill probably is too far from the diaphragm and the spark generated is not able to burn it and start the combustion. Another reason could be due to the black powder: a good amount of black powder is necessary to break the diaphragm;
- *Arming failure*: a not perfect isolation of the injection system and, therefore, a loss of N_2O from the bottom of the thruster occur. The reason could be found in the not correct position of the diaphragm, the injector or the two small O-rings in the injector body or in the use of worn O-rings. To avoid this, it is recommended to incline the thruster case at 45° and slowly pushing the bottle in its housing;
- *Calibration*: in addition to the already discussed problems of calibration (Chap.8.1), it is necessary to specify that the measurement regarding the thrust sensor calibration has been carried out with provisional MHT case. Otherwise the test T006 & T007 have been carried out with the definitive case which is bigger and heavier;
- *Configuration*: considering the configuration with the electric pill inserted from the side holes in the case and not from the nozzle, there is the possibility that the pills break due to the continued movements and solicitations. In this case of course the ignition is not possible. With this configuration there is also problem related to the black powder: if the amount of it is not enough, the diaphragm does not burn and no combustion occurs;
- *Advanced configuration*: referring to the Chap.18, frequent failures occur when a solid compound with kerosene and magnesium powder is used as igniter instead of black powder. The electric igniter pill is not always able to burn this mixture and probably the lack of oxygen in the case inhibits the start of combustion;
- *Saving procedure*: with the schlieren imaging set up, a high speed camera is used to record the firing test. This camera has got an internal hard disk to store the data temporarily until they are stored in other support. This means that is not possible to switch off the camera before saving otherwise all the files and information will be lost.

20. Conclusion

The whole work here presented meets the initial objectives proposed.

Having at disposal the combustion process simulation by NASA CEA and the CFD calculation of the flow field, a first check and comparison of the results shows how close these two models are in terms of thrust, mass flow rate, specific impulse and Mach number. The relative results are presented in the Table 25 and the deviation between these two models is anyway small, around 15%, thus giving a positive feedback about the goodness of the models.

	NASA Cea	Tau Code	Error
Thrust	17.94 N	15.15 N	15.3%
Mass flow rate	10.589 g/s	9.198 g/s	13.1%
Mach	2.742	2.716	1%
Specific impulse	186.54 s	185.97	< 0.5%

Table 25: Comparison of numerical results - NASA CEA vs Tau Code

The deviation between NASA Cea and Tau code results has to be also investigated deeper but in first analysis it is possible to say that this is due to a very important approximation made in the Gordon-McBride software: all the transformation during the simulation is considered to be isentropic, hypothesis not present in Tau code. It has to be considered also that NASA Cea involves a one dimensional flow while Tau code computes two dimensional flows.

For experimental investigation the hybrid thruster is tested on the test rig at the DLR test center in Lampoldshausen and optical diagnostics are applied to investigate the flow field of the exhaust.

The study of temperature field which characterizes the whole system under analysis is carried out using an infrared camera. In this way it is possible to record and take pictures of the experiment and in particular of the exhaust gases and of all the area surrounding the nozzle. In particular the aim of this investigation is to evaluate the position of the Mach disks from the exit of the nozzle looking both the same in the CFD results and in the experimental infrared pictures. This analysis confirms that the temperature fields present the same distribution: the numerical model and the experimental phenomena fit very well together with a very small deviation.

The schlieren imagery is used for the study of the micro hybrid thruster to visualize the exhaust gases and observe the flow field and its structures, especially the Mach patterns. But the main idea to analyze the Mach distribution in the flow field is not possible: any Mach disks or other discontinuities inside the flame are not visualized due to the hot plume surrounding it. A reasonable explanation for this is that the density distribution is not uniform especially near

the exhaust flow with high density gradient in that area: the plume has higher density in comparison with the inner flow and that means it covers all the phenomena related to the lower density of the real exhaust flow. A confirmation of this problem is given also by the CFD results where the density distribution is higher in the border region of the jet than inside of it.

The final comparison between the experimental results and CFD calculation is carried out at the end of the test campaign. The sensors used for the experiment produce values useful as input for the CFD simulation: it is a kind of continuous swap between the numerical and test results, using the latter ones as input for the first in a circle on-going update.

Among the basic parameters measured during the tests, the comparison is led in terms of the thrust generated by this engine.

Considering the Tau Code calculated thrust of 15.15 N and the one provided by the sensor, equal to 23.7 N, an error of about 35% is experienced.

The experimental thrust, defined by the reference point chosen from the experimental test, is not so in accordance with the theoretical one: reason for this discrepancy could be the hypothesis of frozen combustion in CFD simulation, while the combustion in the real phenomena is in equilibrium generating different values of thrust.

Anyway it has to be kept in mind that the environmental conditions (reference temperature and pressure) during the experimental tests are variable and different from numerical hypothesis considered stable.

Considering these, it is probably also necessary to find a better reference point on the thrust curve, chosen in correspondence of a temperature stable along the process.

At the end of this study several considerations about the results are possible which stress the good results of this research.

The slight difference of the numerical results bares a good accordance between NASA Cea and CFD simulations in terms of basic thruster performances. A further and better confirmation of the goodness of the numerical model is provided by the infrared imagery which confirms the presence of the same Mach field in the exhaust flow during the experiment and what has been investigated numerically.

From the other hand, the results in terms of thrust are not so close together and the schlieren visualization does not provide useful information about.

There are a lot of possibilities to improve and get better the system here studied: from a better calibration of the temperature sensors to reduce the noise and accelerate its response to the choice of a new reference point in the curve registered. Currently the most critical aspect of the micro hybrid thruster is the ignition system: this is the main reason of the failures during the test campaign which boast about 85% of success, and a more reliable and satisfactory ignition system could improve this percentage.

The CFD model at the moment provides good and acceptable results in accordance with the rocket theory but new solution to accelerate the convergence and produce better results is always possible.

A bigger and new generation of thruster is at the moment under study with the aim to generate higher thrust (up to 100N) and this development could be a link to further studies of the exhaust having more information and data to compare with the numerical results. These could be the monitoring of the exhaust flow velocity with PIV technique and a new schlieren visualization with different configurations of components to obtain information of the exhaust.

All the tests are performed according applicable standard (DIN, EN, EC-rules, ECSS) and the test team applies standard testing procedures (test preparation, execution, documentation, risk and failure management i.e.).

References

[1] W. Kitsche, S. Alger, G. Costa. *Test Plan for Hybrid Test Rig campaign, Update HTR 004*. Release 2013, DLR , 2011.

[2] Pruefprotokoll – *Druckmesswertaufnehmer* . DLR database , 2004.

[3] Nandan A. Patel. *Assessment of Plasma Assisted Gasification for Effective Polyethylene Terephthalate (PET) Plastic Waste Treatment*. Polytechnic Institute Hartford, Connecticut October, 2012.pg. 13

[4] De Wilde, J.P. *Enthalpy and Entropy of Organic Compounds From Group Contributions*. Delft University of Technology; Faculty of Aerospace Engineering Delft: Memorandum LR M-635 (1990): Delft University of Technology. Web. 20 Nov. 2012.

[5] Walters, Richard, Stacey Hackett, and Richard Lyon. *Heats of Combustion of High Temperature Polymers*. Federal Aviation Administration I (2000): Fire Safety Branch - Federal Aviation Administration. Web. 22 Sept. 2012.

[6] Van Krevelen D.W. *Properties of Polymers. Fourth edition.Chapter 20 "Thermochemical properties"*. Amsterdam. Elsevier, 1990.

[7] Tau-Code user guide,*Release* 2010.2.0-p1,DLR , 2010.

[8] Dr. S.C. Liew. *Electromagnetic waves*. Centre for Remote Imaging, Sensing and Processing. Retrieved 2006-10-27.

[9] Maldague X. P. V., Jones T. S., Kaplan H., Marinetti S. and Prystay M. *Fundamentals of Infrared and Thermal Testing: Part 1. Principles of Infrared and Thermal Testing. Nondestructive Handbook, Infrared and Thermal Testing*, Volume 3, X. Maldague technical ed., P. O. Moore ed., 3rd edition, Ohio , ASNT Press, 2001.

[10] Gordon and McBride. *Computer program for calculation of complex chemical equilibrium compositions and applications. Part 1:Analysis* . NASA Reference Publication 1311,Ohio, June 1996.

[11] Settles G. S. *Schlieren and shadowgraph techniques: visualizing phenomena in transparent media*. Springer, Germany, 2001.

[12] Brooks S.P. and Gelman A. *Alternative methods for monitoring convergence of iterative simulations*. Journal of Computational and Graphical Statistics, 1998.

[13] Pope S.B. *Turbulent flow.* Cambridge University Press, 2000.

[14] Spalart P.R. and Allmaras S.R. *A one-equation turbulence model for aerodynamic flows*. AIAA Paper 92-0439.

[15] Salim M. and Cheah S.C. *Wall y^+ strategy for dealing with wall-bounded turbulent flows.* International Multi Conference of Engineers and Computer Scientists Vol. II, Hong Kong, 2009.

[16] Altman D. *Hybrid rocket development history*. AIAA paper 91-2515.

[17] De Luca L.T. *Problemi energetici in propulsione aerospaziale. Appunti per studenti*. Cap. 12. SpLab, Politecnico di Milano, Italia.

[18] L.Green Jr. *Introductory Considerations on Hybrid Rocket Combustion*. Vol. 15. Academic Press, New York, NY, USA, 1964.

[19] *Quadrant technical data sheet of Polyethylene Terephthalate (Ertalyte).*

[20] Nandan A. Patel. Assessment of Plasma Assisted Gasification for Effective Polyethylene Terephthalate (PET) Plastic Waste Treatment. Polytechnic Institute Hartford, Connecticut October, 2012.pg. 13

[21] Flory P. Principles of polymer chemistry. Cornwell University Press. 1995. Pg 249.

[22] A. Gerasimov. *Modeling Turbulent Flows with FLUENT*. Europe, ANSYS, lnc. 2006.

[23] Courant R., K. O. Fredrichs and H. Lewy (1928). *Uber die Differenzengleichungen der Mathematischen Physik*. Math. Ann, vol.100, p.32, 1928.

Appendix A

In this appendix the technical draw of the micro hybrid thruster are presented in its completeness with referring to each part. This version corresponds to the second generation of the MHT studied in this report, of course more complex to the previous one but simpler than the future bigger generation of the thruster which include a feed system separated by the main unit and able to generate more power.

The following pictures show the overall thruster system n which is possible to recognize the oxidizer bottle, the fuel package, the ignition system and the nozzle (Fig. 82). In the Fig.83 and 84 the detailed descriptions of the aluminum tube, which has the purpose to contain all the components, and the nozzle are represented with all the relevant dimensions.

Pos.	Menge	Einheit	Benennung	Sachnummer / Norm-Kurzbezeichnung
11	2	St	O-Ring 1,6x5	
10	2	St	O-Ring 2,3x16	
9	2	St	Sicherungsring	Bohrung DIN 472 NW20
8	1	St	Zylinderschraube M5x20	ISO 4762-M5x20
7	1	St	N20 Tank	
6	1	St	Fuel Grain	809.09-06/4A
5	1	St	Top-Cap	809.09-05/4A
4	1	St	Piercer	809.09-04/4A
3	1	St	Injector Body	809.09-03/4A
2	1	St	Nozzle	809.09-02/4A
1	1	St	Alu-Rohr	809.09-01/4A
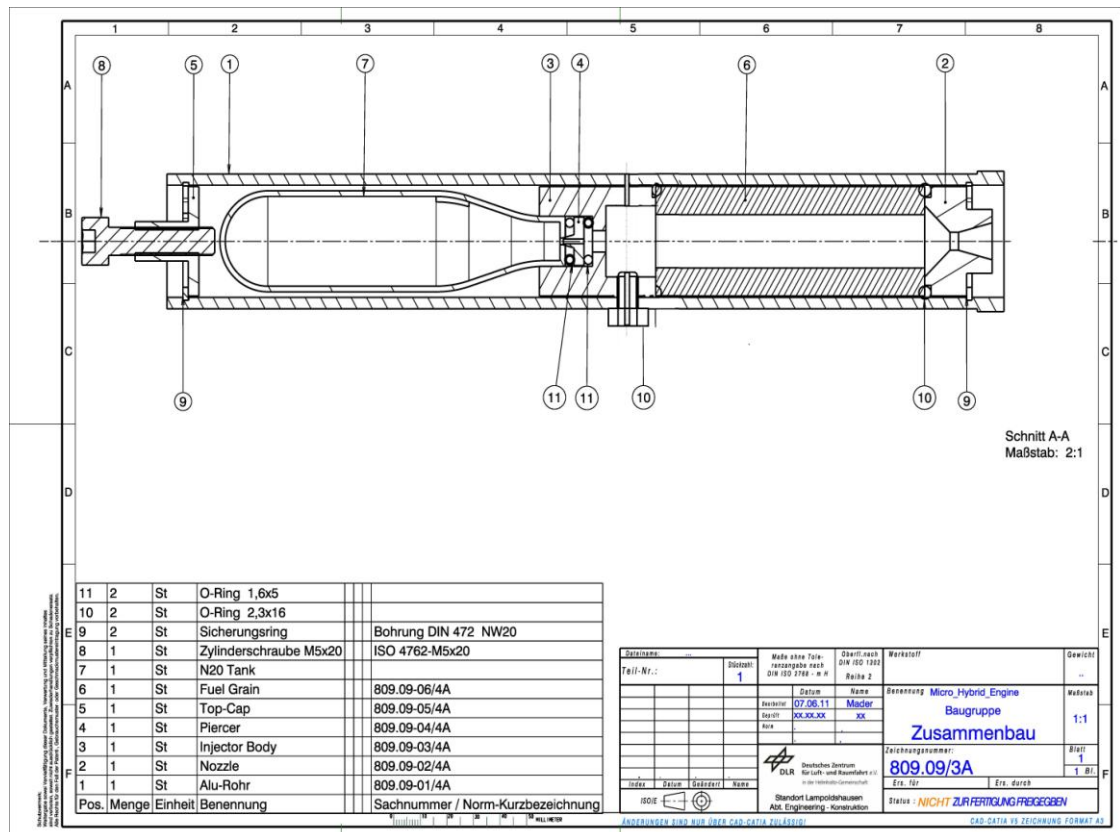
Figure 82: Technical draw MHT
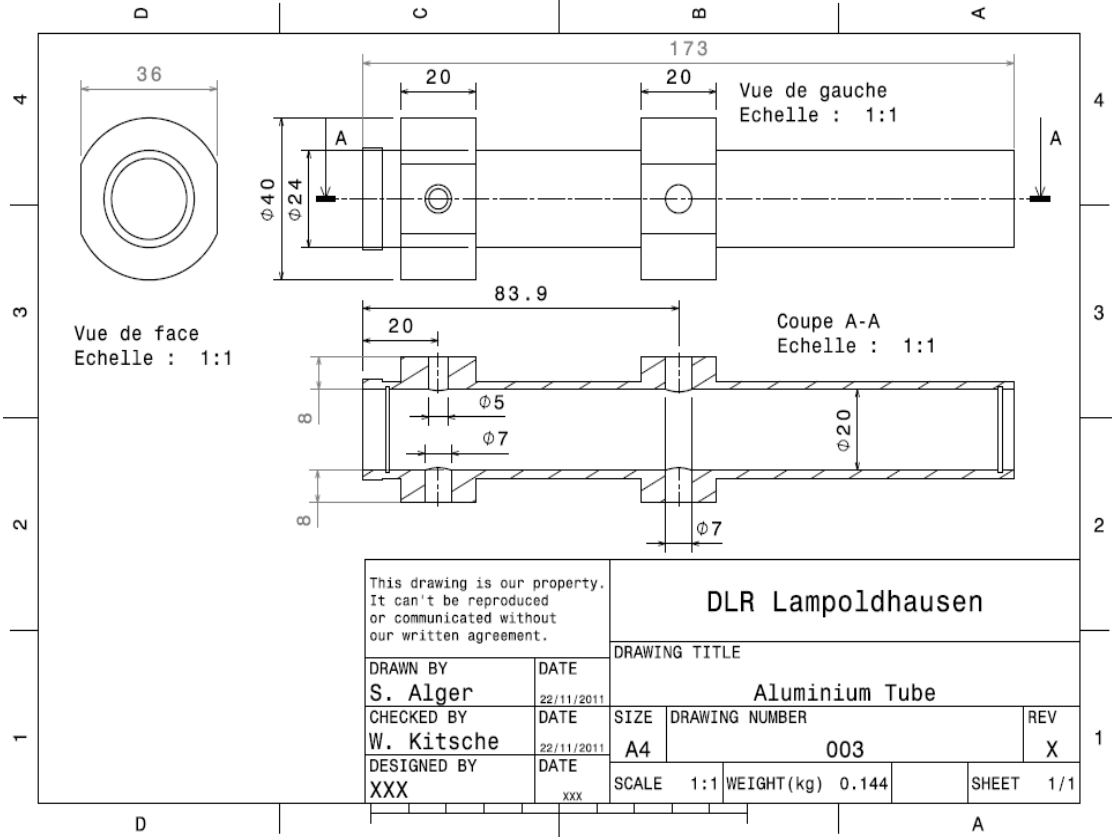
Figure 83: Technical draw of aluminum tube
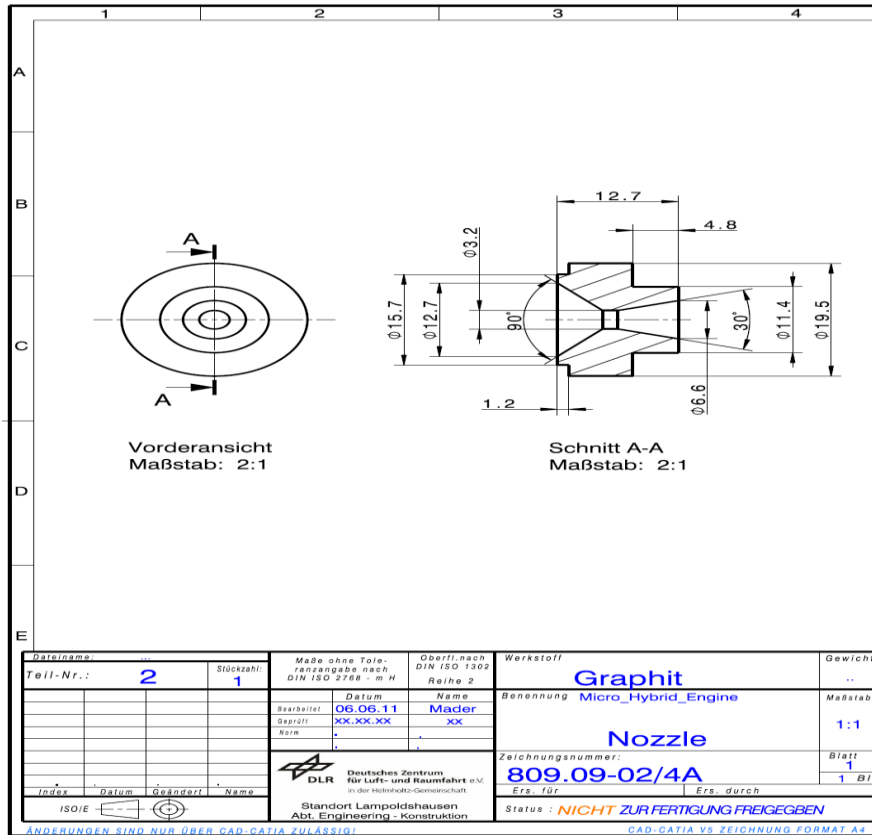
Figure 84: Technical draw nozzle

Appendix B

Here after is presented the parameter file used for the simulation with the Tau code software. As explained in the Chap.3, Tau code is an internal software developed by DLR to solve and evaluate turbulent problems and, in general, to study the fluid dynamics of several problems (i.e. combustion instability, study of properties of nozzle and propulsor…).
For the complete solving Tau code needs as input a large quantity of parameters to define the problem and its boundary conditions. For further details and explanations of each item, refers to Tau code user guide [7].

```
--------------------------------------------------------: -
 PREPROCESSING
 --------------------------------------------------------: -
                   Number of domains: 3
              Number of primary grid domains: 3


    Runtime optimisation ----------------------------: -
         #   Cache-coloring (0/max_faces in color): 0    /* required for vector
architecture */
            Cache-coloring (0/max_faces in color): 50000 /* cache - architecture
*/
              Bandwidth optimisation (0/1): 0
            2D offset vector (0 / x=1,y=2,z=3): 2

Solver parameters:
    Files/IO -------------------------------------: -


######################################################################
######################################

              Restart-data prefix: (none)
            Boundary mapping filename: bmaps/p30_bigff.bmap
              Primary grid filename: grid/nozzle/nozzle_bigff.grid
                Grid prefix: grid/nozzle/nozzle_bigff
              Output files prefix: out/mhe_0006
          Profile output description file: (none)
          Plane output description file: (none)
        Surface output description file: para_sao_final
        Field output description file: para_sao_final
```

Automatic parameter update (0/1): 1
Automatic parameter update mode (0/1): 0
Accumulate queue time (0/1): 1
Output level: 5
Timestepping Start/Stop ------------------------: -
Output period: 10000
Maximal time step number: 10000
Minimum residual: 1e-06
Memory management ------------------------------: -
Increase memory (0/1): 1
Geometry ----------------------------------: -
Grid scale: 0.001
Reference relation area: 0
Reference length (pitching momentum): 1
Reference length (rolling/yawing momentum): 1
Origin coordinate x: 0
Origin coordinate y: 0
Origin coordinate z: 0
Perfect gas thermodynamic ----------------------: -
Gas constant R: 439.045791
Gas constant gamma: 1.2924
References --------------------------------: -
Reference temperature: 300
Reference pressure: 101325
Reference velocity: 0.5
Reference outer pressure: 101325
Variables ---------------------------------: -
Fix negative values (0/1): 1
Minimal density: 1e-12
Minimal pressure: 1e-12
Minimal energy: 1e-12
Flowfield initialization -----------------------: -
Init total conditions (0/1): 0

Solver IO parameters:
IO ---------------------------------------: -
Write pointdata dimensionless (0/1): 0
Reference system of forces and moments (tau/ln9300): tau
Universal ---------------------------------: -
Solver type: Flow
Monitoring --------------------------------: -
Monitor history (0/1): 1
Residual monitoring type (0/1): 1

Monitoring values: Residual_Max-res_dnue/dt_Max-y+_Max-eddyv
Monitoring significant figures: 4_4_4_4_4
Extended coefficient monitoring (0/1): 0
Flux main ---------------------------------------: -
Inviscid flux discretization type: Upwind
Viscous flux type TSL/Full (0/1): 1
Mixed inviscid fluxes (0/1): 0
Upwind flux ------------------------------------: -
Upwind flux: AUSMDV
Order of upwind flux (1-2): 2
Order of additional equations (1-2): 2
Mach number limit for limiter: 0
Lowest pressure for 2nd order: 0
AUSMDV shock fix (0/1): 1
Limiter --------------------------------------: -
Limiter freezing convergence: 0
Venkatakrishnan limiter constant: -1
SRR limiter active (0/1): 0
SRR limiter radius relaxation constant: 0.03
Coarse grid upwind flux: Van_Leer
Gradients ------------------------------------: -
Reconstruction of gradients: Least_square
Relaxation -------------------------------------: -
Relaxation solver: Backward_Euler
Hold static velocity field (0/1): 0
Backward Euler ---------------------------------: -
Linear solver: Lusgs
Compute lusgs mapping (0/1): 1
Implicit overrelaxation omega: 1
Implicit overrelaxation beta: 1
Turbulence model equations eigenvalue correction: 1
LUSGS --------------------------------------: -
Sgs stages maximum: 3
Lusgs increased parallel communication (0/1): 1
Lusgs treat whirl implicitly (0/1): 1
Multigrid -------------------------------------: -
MG description filename: sg
Multigrid indicator (0/1): 1
SG start up steps (fine grid): 0
Turbulence equations use multigrid (0/1): 0
Coarse grid viscous flux type TSL/Full (0/1): 0
Use new multigrid (0/1): 0
Full multigrid ---------------------------------: -

Multigrid start level: 5
Maximal time step number (coarse grids): 5000
Minimum residual (coarse grids): 1e-10
Full multigrid central scheme first-order (0/1): 1
Timestepsize ------------------------------------: -
CFL number: 2
CFL number (coarse grids): 0.05
CFL number (large grad p): 0.4
Time step smoothing factor: 0
Smoother --: -
Residual smoother: Point_explicit
Correction smoother: Point_explicit
Correction smooth epsilon: 0.2
Residual smooth epsilon: 0.2002
Correction smoothing steps: 2
Residual smoothing steps: 2
Preconditioning ---------------------------------: -
Preconditioning: (none)
Cut-off value: 1
Turbulence --------------------------------------: -
Turbulence mode: RANS
Ratio Prandtl lam/turb: 0.8
General ratio mue-t/mue-l: 0.1
Maximum limit mue-t/mue-l: 20000
General turbulent intensity: 0.001
Reference bl-thickness: 1e+22
Turbulence model version: SAO
Positivity scheme: 0
EARSM expansion order: 1
Vortical flow correction (0/1): 0
Turbulence diffusion flux type TSL/Full (0/1): 1
Vortex generator modeling (0/1): 0
SA models ---------------------------------------: -
SA boundary condition type: smooth
SA attractor for zero value (0/1): 0
Cauchy convergence control ----------------------: -
Use Cauchy convergence control: off
Error for Cauchy convergence clift: -1
Error for Cauchy convergence cdrag: -1
Error for Cauchy convergence cmy: -1
Error for Cauchy convergence cost function: 1e-06
Number of samples for Cauchy convergence: 20
Factor for dynamic Cauchy convergence: 0.05

Chimera search --------------------------------: -
Suppress error on orphaned points (0/1): 0
Chimera wall projection ------------------------: -
Apply Chimera wall projection (0/1): 0
Mismatch of overlapping walls: 0

Solver IO parameters:
IO ---: -
Write pointdata dimensionless (0/1): 0
Reference system of forces and moments (tau/ln9300): tau

Parameters section refinement:
Refinement Parameter ----------------------------: -
Refinement mode: both
!Change wall normal distribution (0/1): 1
Maximum point number: 800000
Maximum point number per partition: -1
Maximum refinement level: -1
Percentage of new points: 30
Adaptation sensitivity: 0.9
Minimum edge length: 1e-9
Part of low quality elements: 0
Global Indicator settings -----------------------: -
Indicator type: diff
h-scaling power: 0.5
h-scaling reference length: 0

Indicator type diff scalings ------------------: -
Indicator0 V-scaling: 1
Indicator0 rho-scaling: 1
Indicator0 Ht-scaling: 1
Indicator0 Pt-scaling: 1
Indicator user settings -----------------------: -
Indicator user-scaling: 1
Indicator user-values: p

Refinement regime -----------------------------: -
Number of cut-out volumes: -1
Minima x-direction: 0
Minima y-direction: -1000
Minima z-direction: 0
Maxima x-direction: 100

Maxima y-direction: 1000
Maxima z-direction: 20
Frustum min radius: 0
Frustum max radius: 0

Surface Reconstruction Parameter ----------------: -
Maximum surface angle (degree): 30
Maximal point movement factor: 0.2
---: -

Appendix C

The complete output of the combustion simulation performed by NASA Cea is presented here. In the first part the input data and options set from the user are reported. Then the properties of the defined problem are presented together with the performance parameters and all the species involved in the combustion product. For more details and explanations, refers to [10].


```
*****************************************************************

      NASA-GLENN CHEMICAL EQUILIBRIUM PROGRAM CEA2, MAY
21, 2004
            BY  BONNIE MCBRIDE AND SANFORD GORDON
   REFS: NASA RP-1311, PART I, 1994 AND NASA RP-1311, PART II,
1996

*****************************************************************
```

```
 problem    o/f=7.0778,
   rocket  frozen  nfz=1  tcest,k=6000
  p,bar=16.6,
  sup,ae/at=4.2539,
 react
  oxid=N2O wt=1
  fuel=pet  wt=1
    h,kj/mol=-268.008  C 10 H 8 O 4
 end
```

```
 OPTIONS: TP=F  HP=F  SP=F  TV=F  UV=F  SV=F  DETN=F  SHOCK=F
REFL=F  INCD=F
 RKT=T  FROZ=T  EQL=F  IONS=F  SIUNIT=T  DEBUGF=F  SHKDBG=F
DETDBG=F  TRNSPT=F
```

```
 TRACE= 0.00E+00    S/R= 0.000000E+00    H/R= 0.000000E+00    U/R=
0.000000E+00
```

```
 Pc,BAR =    16.600000
```

```
  SUPERSONIC AREA RATIOS =     4.2539
```

```
 NFZ= 1  Mdot/Ac= 0.000000E+00  Ac/At= 0.000000E+00
```

REACTANT   WT.FRAC (ENERGY/R),K TEMP,K DENSITY
    EXPLODED FORMULA
O: N2O   1.000000 0.000000E+00   0.00 0.0000
    N 2.00000 O 1.00000
F: pet   1.000000 -0.322338E+05   0.00 0.0000
    C 10.00000 H 8.00000 O 4.00000

SPECIES BEING CONSIDERED IN THIS SYSTEM

g 7/97 *C   tpis79 *CH   g 4/02 CH2
g 4/02 CH3   g11/00 CH2OH   g 7/00 CH3O
g 8/99 CH4   g 7/00 CH3OH   srd 01 CH3OOH
g 8/99 *CN   g12/99 CNN   tpis79 *CO
g 9/99 *CO2   tpis91 COOH   tpis91 *C2
g 6/01 C2H   g 1/91 C2H2,acetylene g 5/01 C2H2,vinylidene
g 4/02 CH2CO,ketene   g 3/02 O(CH)2O   srd 01 HO(CO)2OH
g 7/01 C2H3,vinyl   g 9/00 CH3CN   g 6/96 CH3CO,acetyl
g 1/00 C2H4   g 8/88 C2H4O,ethylen-o g 8/88 CH3CHO,ethanal
g 6/00 CH3COOH   srd 01 OHCH2COOH   g 7/00 C2H5
g 7/00 C2H6   g 8/88 CH3N2CH3   g 8/88 C2H5OH
g 7/00 CH3OCH3   srd 01 CH3O2CH3   g 7/00 CCN
tpis91 CNC   srd 01 OCCN   tpis79 C2N2
g 8/00 C2O   tpis79 *C3   n 4/98 C3H3,1-propynl
n 4/98 C3H3,2-propynl g 2/00 C3H4,allene   g 1/00 C3H4,propyne
g 5/90 C3H4,cyclo-   g 3/01 C3H5,allyl   g 2/00 C3H6,propylene
g 1/00 C3H6,cyclo-   g 6/01 C3H6O,propylox g 6/97 C3H6O,acetone
g 1/02 C3H6O,propanal g 7/01 C3H7,n-propyl   g 9/85 C3H7,i-propyl
g 2/00 C3H8   g 2/00 C3H8O,1propanol g 2/00 C3H8O,2propanol
srd 01 CNCOCN   g 7/88 C3O2   g tpis *C4
g 7/01 C4H2,butadiyne g 8/00 C4H4,1,3-cyclo- n10/92 C4H6,butadiene
n10/93 C4H6,1butyne   n10/93 C4H6,2butyne   g 8/00 C4H6,cyclo-
n 4/88 C4H8,1-butene n 4/88 C4H8,cis2-buten n 4/88 C4H8,tr2-butene
n 4/88 C4H8,isobutene g 8/00 C4H8,cyclo-   g10/00 (CH3COOH)2
n10/84 C4H9,n-butyl   n10/84 C4H9,i-butyl   g 1/93 C4H9,s-butyl
g 1/93 C4H9,t-butyl   g12/00 C4H10,n-butane g 8/00 C4H10,isobutane
g 6/01 C4N2   g 8/00 *C5   g 5/90 C5H6,1,3cyclo-
g 1/93 C5H8,cyclo-   n 4/87 C5H10,1-pentene g 2/01 C5H10,cyclo-
n10/84 C5H11,pentyl   g 1/93 C5H11,t-pentyl n10/85 C5H12,n-pentane
n10/85 C5H12,i-pentane n10/85 CH3C(CH3)2CH3 g 2/93 C6H2
g11/00 C6H5,phenyl   g 8/00 C6H5O,phenoxy   g 8/00 C6H6
g 8/00 C6H5OH,phenol g 1/93 C6H10,cyclo-   n 4/87 C6H12,1-hexene
g 6/90 C6H12,cyclo-   n10/83 C6H13,n-hexyl   g 6/01 C6H14,n-hexane

g 7/01 C7H7,benzyl   g 1/93 C7H8   g12/00 C7H8O,cresol-mx
n 4/87 C7H14,1-heptene n10/83 C7H15,n-heptyl   n10/85 C7H16,n-heptane
n10/85 C7H16,2-methylh n 4/89 C8H8,styrene   n10/86 C8H10,ethylbenz
n 4/87 C8H16,1-octene   n10/83 C8H17,n-octyl   n 4/85 C8H18,n-octane
n 4/85 C8H18,isooctane n10/83 C9H19,n-nonyl   g 3/01 C10H8,naphthale
n10/83 C10H21,n-decyl   g 8/00 C12H9,o-bipheny g 8/00 C12H10,biphenyl
g 6/97 *H   g 6/01 HCN   g 1/01 HCO
tpis89 HCCN   g 6/01 HCCO   g 6/01 HNC
g 7/00 HNCO   g10/01 HNO   tpis89 HNO2
g 5/99 HNO3   g 4/02 HO2   tpis78 *H2
g 5/01 HCHO,formaldehy g 6/01 HCOOH   g 8/89 H2O
g 6/99 H2O2   g 6/01 (HCOOH)2   g 5/97 *N
g 6/01 NCO   g 4/99 *NH   g 3/01 NH2
tpis89 NH3   tpis89 NH2OH   tpis89 *NO
g 4/99 NO2   j12/64 NO3   tpis78 *N2
g 6/01 NCN   g 5/99 N2H2   tpis89 NH2NO2
g 4/99 N2H4   g 4/99 N2O   g 4/99 N2O3
tpis89 N2O4   g 4/99 N2O5   tpis89 N3
g 4/99 N3H   g 5/97 *O   g 4/02 *OH
tpis89 *O2   g 8/01 O3   n 4/83 C(gr)
n 4/83 C(gr)   n 4/83 C(gr)   g11/99 H2O(cr)
g 8/01 H2O(L)   g 8/01 H2O(L)

O/F = 7.077800

          EFFECTIVE FUEL   EFFECTIVE OXIDANT   MIXTURE
ENTHALPY   h(2)/R   h(1)/R   h0/R
(KG-MOL)(K)/KG   -0.16773734E+03   0.00000000E+00   -
0.20765226E+02

KG-FORM.WT./KG   bi(2)   bi(1)   b0i
 *N   0.00000000E+00   0.45441326E-01   0.39815868E-01
 *O   0.20815107E-01   0.22720663E-01   0.22484763E-01
 *C   0.52037768E-01   0.00000000E+00   0.64420718E-02
 *H   0.41630214E-01   0.00000000E+00   0.51536575E-02

POINT ITN   T   N   O   C   H

 1 26   2528.580   -12.727   -14.553   -21.492   -12.638

     THEORETICAL ROCKET PERFORMANCE ASSUMING FROZEN
COMPOSITION

Pin = 240.8 PSIA
CASE =

REACTANT		WT FRACTION (SEE NOTE)	ENERGY KJ/KG-MOL	TEMP K
OXIDANT	N2O	1.0000000	0.000	0.000
FUEL	pet	1.0000000	-268008.000	0.000

O/F=   7.07780   %FUEL= 12.379608   R,EQ.RATIO= 0.687620
PHI,EQ.RATIO= 0.647186

	CHAMBER	THROAT	EXIT
Pinf/P	1.0000	1.7980	27.930
P, BAR	16.600	9.2325	0.59434
T, K	2528.58	2256.01	1295.79
RHO, KG/CU M	2.4203 0	1.5088 0	1.6910-1
H, KJ/KG	-172.65	-552.96	-1845.75
U, KJ/KG	-858.51	-1164.89	-2197.22
G, KJ/KG	-21813.5	-19861.0	-12935.7
S, KJ/(KG)(K)	8.5585	8.5585	8.5585

M, (1/n)	30.654	30.654	30.654
Cp, KJ/(KG)(K)	1.4026	1.3874	1.2892
GAMMAs	1.2397	1.2430	1.2665
SON VEL,M/SEC	922.1	872.1	667.2
MACH NUMBER	0.000	1.000	2.742

PERFORMANCE PARAMETERS

Ae/At	1.0000	4.2539
CSTAR, M/SEC	1261.5	1261.5
CF	0.6913	1.4500
Ivac, M/SEC	1573.8	2021.4
Isp, M/SEC	872.1	1829.3

MOLE FRACTIONS

*CO	0.00629	*CO2	0.19118	*H	0.00014
HO2	0.00002	*H2	0.00040	H2O	0.07539
*NO	0.01469	NO2	0.00004	*N2	0.60288
*O	0.00130	*OH	0.00625	*O2	0.10142

 * THERMODYNAMIC PROPERTIES FITTED TO 20000.K